Statistical modeling, level-set and ensemble learning for automatic segmentation of 3D high-frequency ultrasound data : towards expedited quantitative ultrasound in lymph nodes from cancer patients

Thanh Bui Minh

THÈSE DE DOCTORAT DE L'UNIVERSITÉ PIERRE ET MARIE CURIE

Spécialité

Informatique Biomédical - Imagerie Biomédicale

École doctorale Pierre Louis de santé publique à Paris : Épidémiologie et Science de l'Information Biomédicale

Présentée par

Thanh Minh BUI

Pour obtenir le grade de

DOCTEUR de l'UNIVERSITÉ PIERRE ET MARIE CURIE

Sujet de la thèse:

Statistical modeling, level-set and ensemble learning for automatic segmentation of 3D high-frequency ultrasound data: Towards expedited quantitative ultrasound in lymph nodes from cancer patients

Soutenue le 02 Juin 2016 devant le jury composé de :

M. Denis FRIBOULET	Rapporteur
Mme. Yao WANG	Rapporteur
M. Djamal BOUKERROUI	Examinateur
M. Jonathan MAMOU	Examinateur
M. Frédéric OSSANT	Examinateur
Mme. Magali SVRCEK	Examinateur
Mme. Lori BRIDAL	Directrice de thèse
M. Alain CORON	Codirecteur de thèse

Laboratoire d'imagerie biomédicale
15 rue de l'école de médecine
75006 Paris

UPMC
École doctorale Pierre Louis de santé publique à Paris: Epidémiologie et Science de l'Information Biomédicale
15 rue de l'école de médecine
75006 Paris

Contents

Acknowledgements

First of all, I would like to express my sincere gratitude to my thesis supervisors Dr. Alain Coron and Dr. S. Lori Bridal for your guidance, patience and continuous supports during my graduate study. Alain has provided me with guidance throughout most of my time as a graduate student. I learned a lot from you, not only your technical knowledge but also your carefulness. Lori has been very supportive during my PhD studies. I greatly appreciate your help in the writing of publications and this thesis. Thank you for encouraging my research and for allowing me to grow as a research scientist.

During my study, I have had the opportunity to collaborate with researchers from Riverside Research, New York, USA. I am grateful to Dr. Jonathan Mamou and Dr. Ernest J. Feleppa for your advice and encouragement. It is no exaggeration to say that Jonathan is my third supervisor who usually provides me with helpful comments, timely advice and guidance. Dr. Feleppa is always available to provide feedback and corrections to help me finalize publications.

I would like to thank Prof. Denis Friboulet and Prof. Yao Wang for your acceptance to be reviewers of my thesis and for your insightful comments and encouragement. I would also like to thank Prof. Djamal Boukerroui, Dr. Frédéric Ossant and Dr. Magali Svrcek for serving on my thesis committee.

I am thankful to Dr. Emi Saegusa-Beecroft, Dr. Eugene Yanagihara and Dr. Junji Machi who have contributed to my thesis in different ways.

I would like to thank Dr. Pascal Laugier for receiving and integrating me into the laboratory. I am also thankful to Dr. Jean Charlet for being my tutor during my graduate study.

Many friends and colleagues have helped me stay sane through these difficult years. Their support and care helped me overcome setbacks and stay focused on my graduate study. I greatly value their friendship and appreciate their belief in me.

Most importantly, I am grateful to my wife, my father and my sister for always supporting me in what I was doing.

Finally, I appreciate the financial support from NIH (grant CA100183) that funded parts of the research presented in this thesis.

Abstract

This work investigates approaches to obtain automatic segmentation of three media (i.e., lymph node parenchyma, perinodal fat and normal saline) in lymph node (LN) envelope data to expedite quantitative ultrasound (QUS) in dissected LNs from cancer patients. A statistical modeling study identified a two-parameter gamma distribution as the best model for data from the three media based on its high fitting accuracy, its analytically less-complex probability density function (PDF), and closed-form expressions for its parameter estimation. Two novel level-set segmentation methods that made use of localized statistics of envelope data to handle data inhomogeneities caused by attenuation and focusing effects were developed. The first, local region-based gamma distribution fitting (LRGDF), employed the gamma PDFs to model speckle statistics of envelope data in local regions at a controllable scale using a smooth function with a compact support. The second, statistical transverse-slice-based level-set (STS-LS), used gamma PDFs to locally model speckle statistics in consecutive transverse slices. A novel method was then designed and evaluated to automatically initialize the LRGDF and STS-LS methods using random forest classification with new proposed features. Methods developed in this research provided accurate, automatic and efficient segmentation results on simulated envelope data and data acquired for LNs from colorectal- and breast-cancer patients as compared with manual expert segmentation. Results also demonstrated that accurate QUS estimates are maintained when automatic segmentation is applied to evaluate excised LN data.

Résumé de la thèse

Afin d'accélérer et automatiser l'analyse par ultrasons quantitatifs de ganglions lymphatiques de patients atteints d'un cancer, plusieurs segmentations automatiques des trois milieux rencontrés (le parenchyme du ganglion, la graisse périnodale et le sérum physiologique) sont étudiées. Une analyse statistique du signal d'enveloppe a permis d'identifier la distribution gamma comme le meilleur compromis en termes de qualité de la modélisation, simplicité du modèle et rapidité de l'estimation des paramètres. Deux nouvelles méthodes de segmentation basées sur l'approche par ensemble de niveaux et la distribution gamma sont décrites. Des statistiques locales du signal d'enveloppe permettent de tenir compte des inhomogénéités du signal dues à l'atténuation et la focalisation des ultrasons. La méthode appelée LRGDF modélise les statistiques du speckle dans des régions dont la taille est contrôlable par une fonction lisse à support compact. La seconde, appelée STS-LS, considère des coupes transverses, perpendiculaires au faisceau, pour gagner en efficacité. Une troisième méthode basée sur la classification par forêt aléatoire a été conçue pour initialiser et accélérer les deux précédentes. Ces méthodes automatiques sont comparées à une segmentation manuelle effectuée par un expert. Elles fournissent des résultats satisfaisants aussi bien sur des données simulées que sur des données acquises sur des ganglions lymphatiques de patients atteints d'un cancer colorectal ou du sein. Les paramètres ultrasonores quantitatifs estimés après segmentation automatique ou après segmentation manuelle par un expert sont comparables.

List of Publications

International Journal Publications

- **Thanh Minh Bui**, Alain Coron, Jonathan Mamou, Emi Saegusa-Beecroft, Tadashi Yamaguchi, Eugene Yanagihara, Junji Machi, S. Lori Bridal, and Ernest J. Feleppa, "Modeling the Envelope Statistics of Three-dimensional High-frequency Ultrasonic Backscatter from Dissected Human Lymph Nodes", Japanese Journal of Applied Physics, vol. 53, pp. 07KF22-1 – 11, 2014.

- **Thanh Minh Bui**, Alain Coron, Jonathan Mamou, Emi Saegusa-Beecroft, Tadashi Yamaguchi, Eugene Yanagihara, Junji Machi, S. Lori Bridal, and Ernest J. Feleppa, "Local Transverse-slice-based Level-set Method for Segmentation of 3D, High-frequency Ultrasonic Backscatter from Dissected Human Lymph Nodes", IEEE Transactions on Biomedical Engineering (Resubmitted after getting review with decision "Minor Revisions").

International Conference Proceedings

- **Thanh M. Bui**, Alain Coron, Jonathan Mamou, Emi Saegusa-Beecroft, Eugene Yanagihara, Junji Machi, Alexandre Dizeux, S. Lori Bridal, and Ernest J. Feleppa, "Level-set segmentation of 2D and 3D ultrasound data using local gamma distribution fitting energy", IEEE International Symposium on Biomedical Imaging: From nano to macro (ISBI), New York, USA, 2015, pp. 1110-1113.

- **Thanh M. Bui**, Alain Coron, Jonathan Mamou, Emi Saegusa-Beecroft, Eugene Yanagihara, Junji Machi, S. Lori Bridal, and Ernest J. Feleppa, "Random Forest Classification and Local Region-Based, Level-Set Segmentation for Quantitative Ultrasound of Human Lymph Nodes", IEEE International Ultrasonics Symposium (IUS), Taipei, Taiwan, 2015, pp. 1-4.

- **Thanh M. Bui**, Alain Coron, Jonathan Mamou, Emi Saegusa-Beecroft, Tadashi Yamaguchi,

Eugene Yanagihara, Junji Machi, S. Lori Bridal, and Ernest J. Feleppa, "Statistical Analysis of the Envelope of Three-dimensional High-frequency Ultrasonic Backscatter from Dissected Human Lymph Nodes", Symposium on UltraSonic Electronics (USE 2013), Japan.

Presentations at International Conferences

- **Thanh M. Bui**, Alain Coron, Jonathan Mamou, Emi Saegusa-Beecroft, Eugene Yanagihara, Junji Machi, S. Lori Bridal, and Ernest J. Feleppa, "A 3D, 3-Phase, Level-Set Segmentation Method for Quantitative Ultrasound Processing of Human Lymph Node Data", International Congress on Ultrasonics (ICU), Metz, France, 2015.

- Emi Saegusa-Beecroft, Jonathan Mamou, Daniel Rohrbach, **Thanh Minh Bui**, Alain Coron, Tadashi Yamaguchi, Michael Oelze, Gregory Kobayashi, Clifford Wong, Conway Fung, Masaki Hata, S Lori Bridal, Eugene Yanagihara, Junji Machi, Ernest J Feleppa, "Advances in Three-Dimensional (3D) High-Frequency (HF) Quantitative Ultrasound (QUS) for the Detection of Metastases in Lymph Nodes of Breast, Colorectal and Gastric Cancers", The United States & Canadian Academy of Pathology Conference (USCAP), Boston, USA, 2015.

- Jonathan Mamou, Daniel Rohrbach, Alain Coron, Emi Saegusa-Beecroft, **Thanh Minh Bui**, Michael L Oelze, Eugene Yanagihara, Lori Bridal, Tadashi Yamaguchi, Junji Machi, Ernest J Feleppa, "Quantitative-ultrasound detection of cancer in human lymph nodes based on support vector machines", the 168th Meeting of the Acoustical Society of America, Indiana, USA, 2014.

- Alain Coron, **Thanh Minh Bui**, "Segmentation of ultrasound images and sequences: an overview", Ultrasonic Imaging and Tissue Characterization Symposium (UITC), USA, 2013.

Abbreviations

2D Two-dimensional

3D Three-dimensional

CDF Cumulative distribution function

HF High frequency

HFU High-frequency ultrasound

KS Kolmogorov Smirnov

LN Lymph node

LNP Lymph node parenchyma

LRGDF Local region-based gamma distribution fitting

MAP Maximum a posteriori

NS Normal saline

PDF Probability density function

PNF Perinodal fat

QUS Quantitative ultrasound

RF Random forest

RFC Random forest classification

ROI Region of interest

STS-LS Statistical transverse-slice-based level-set

Long résumé de la thèse en français

Les ganglions lymphatiques et leur rôle dans la prise en charge du cancer

Les ganglions lymphatiques appartiennent au système lymphatique et sont de petits organes ayant une forme ovoïde ou réniforme connectés à des vaisseaux sanguins et des vaisseaux lymphatiques. Ils jouent un rôle important dans le système immunitaire et sont responsables de la filtration de la lymphe avant que celle-ci ne retourne dans la circulation générale. Lors du développement d'un cancer, la présence ou l'absence de métastases dans les ganglions lymphatiques qui drainent la tumeur, est pris en compte pour déterminer le stade de la maladie et donc le traitement à suivre.

Les ultrasons quantitatifs

On désigne par ultrasons quantitatifs un ensemble de techniques qui estiment des paramètres liés à la microstructure d'un milieu, comme un tissu, à partir des signaux ultrasonores rétrodiffusés par ce milieu. Un signal ultrasonore radio-fréquence (RF) est composé d'échos obtenus par réflexions d'un faisceau ultrasonore sur une surface séparant deux milieux ayant des propriétés acoustiques différentes, ainsi que de composantes de diffusion du faisceau par des structures dont la taille est inférieure à la longueur d'onde. Ce sont notamment les composantes fréquentielles de ces derniers signaux qui renferment des informations sur la micro-structure des tissus.

En imagerie ultrasonore conventionnelle, l'information ultrasonore est représentée par des images dites en mode-B construites à partir du logarithme de l'enveloppe du signal radio-fréquence. Cette représentation des données est moins riche que le signal RF. Aussi d'une part le mode-B permet d'observer des structures dont les dimensions sont supérieures à la longueur d'onde. Et d'autre part pour évaluer la micro-structure tissulaire, les analyses s'appuient bien souvent sur le signal RF.

Par exemple, après transformée de Fourier du signal RF, les variations du contenu spectral du signal

RF sont extraites et reliées à des propriétés décrivant la microstructure des tissus biologiques à l'aide d'un modèle de diffusion comme le modèle de diffuseur Gaussien.

Les ultrasons quantitatifs pour détecter les métastases dans les ganglions lymphatiques

Notre laboratoire collabore depuis 2007 avec d'autres équipes à un projet visant à détecter à l'aide d'ultrasons quantitatifs les métastases dans les ganglions lymphatiques. Le projet mené par Ernest Feleppa de Riverside Research à New York est en partie financé par le NIH (contrat CA100183). Les résultats de cette collaboration [1–4] ont permis de montrer le potentiel des ultrasons quantitatifs à haute-fréquence (> 15 MHz) pour analyser en 3D l'ensemble du ganglion et détecter les métastases. Une fois les signaux RF acquis, l'analyse comprend 3 étapes importantes : la segmentation des données 3D, l'estimation des paramètres ultrasonores quantitatifs et la classification (ganglions sains/ganglions métastatiques).

L'acquisition des données est décrite dans le 2^{e} chapitre. En résumé, les ganglions extraits de la pièce opératoire sont immergés dans du liquide physiologique (NS) et les signaux RF sont enregistrés avec un transducteur monoélément focalisé de fréquence centrale 25.6 MHz. Cependant il reste toujours une pellicule de graisse (PNF) résiduelle autour du parenchyme du ganglion (LNP). Segmenter les trois milieux (LNP, PNF et NS) est nécessaire pour restreindre l'estimation des paramètres ultrasonores au parenchyme et tenir compte de l'atténuation des trois milieux lors de l'estimation des paramètres ultrasonores quantitatifs. Enfin à partir de la segmentation, il est aisé d'extraire la taille, la forme, et le volume des ganglions qui pourraient être utilisés comme biomarqueurs.

Une fois segmenté, 13 paramètres ont été considérés dont les quatre principaux sont la taille et la concentration efficaces des diffuseurs, l'ordonnée à l'origine et la pente du spectre. Deux modèles de diffusion différents permettent d'estimer ces quatre valeurs à partir d'un spectre normalisé tenant compte de l'atténuation, appelé également coefficient de rétrodiffusion [5]. La figure (1.6) illustre la façon d'obtenir le coefficient de rétrodiffusion. Les neuf autres paramètres sont des paramètres statistiques dérivés de l'enveloppe du signal radio-fréquence.

Dans une précédente étude, et sur une base de données comprenant 172 ganglions de patients at-

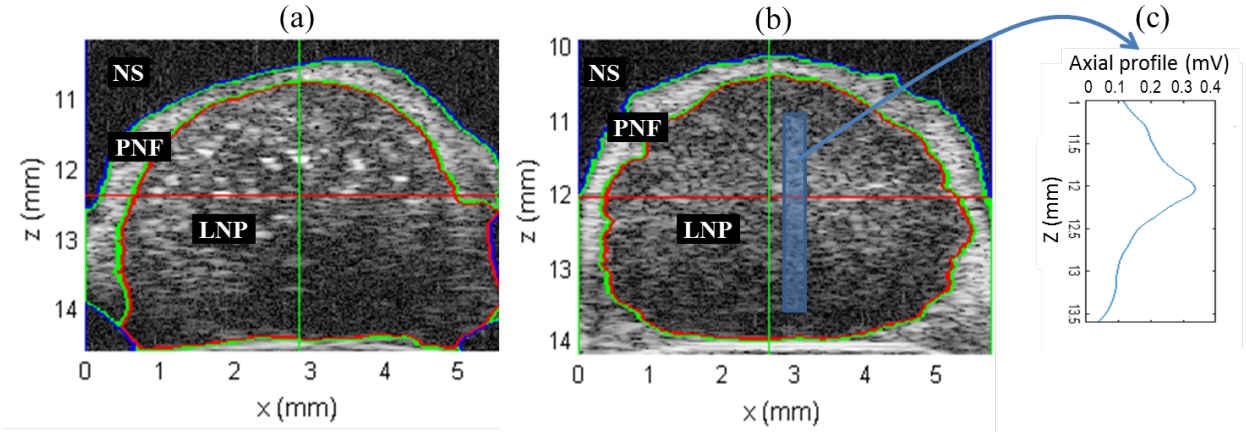

Figure 1: Deux images en B-mode montrant 2 coupes 2D (plan x-z) d'acquisitions ultrasonores haute-fréquence 3D effectuées sur un ganglion métastatique (a) et un ganglion sain (b). La méthode STS-LS décrite au Chapitre 5 a été utilisée pour segmenter le parenchyme ganglionnaire (LNP) délimitée par un trait rouge, la graisse (PNF) délimitée par un trait vert, et le liquide physiologique (NS) délimité par un trait bleu. (c) Le profil représente une version lissée de l'enveloppe du signal radio-fréquence et il a été calculé le long du rectangle bleu visible dans (b). Il illustre l'inhomogénéité de l'enveloppe avec la profondeur.

teints d'un cancer colorectal ou gastrique, l'aire sous la courbe de la Caractéristique Opérationnelle du Récepteur (COR) a été estimée pour évaluer la performance de la classification en deux classes (ganglion sain, ganglion métastatique) d'un classificateur linéaire. Des aires sous la courbes supérieures à 0.95 ont été obtenues pour les ganglions colorectaux et gastriques. En dépit de ces résultats prometteurs, l'adoption de cette méthode en pratique clinique est limitée par le temps nécessaire pour segmenter les données qui étaient initialement segmentées à l'aide d'une méthode semi-automatique nécessitant beaucoup d'attention [6]. Développer une segmentation 3D automatique et plus robuste est indispensable pour envisager une utilisation en routine clinique.

Les défis de la segmentation des données ultrasonores haute-fréquence

Segmenter une image est un problème mal posé consistant à partitionner l'image en régions cohérentes afin par exemple d'isoler un ou plusieurs objets dans l'image. Les techniques à mettre en oeuvre peuvent être simples comme un seuillage ou s'appuyer sur des techniques très raffinées pour, par exemple, intégrer des connaissances a priori sur l'intensité, la texture ou la forme des objets recherchés. Les images ultrasonores restent souvent difficiles à interpréter et donc à seg-

menter à cause de la présence du speckle, d'un contraste parfois limité, de frontières très ténues ou absentes entre deux régions, et de l'atténuation.

En plus des difficultés évoquées, les acquisitions ultrasonores haute-fréquence des ganglions ont été acquises à l'aide d'un transducteur monoélément focalisé. Aussi les effets de la focalisation et de l'attenuation sont particulièrement visibles. Ainsi le rapport signal à bruit est faible dans les régions les plus éloignées du transducteur comme on peut l'observer sur la figure 1(a). Avec un transducteur focalisé, le faisceau converge à la focale puis diverge, ce qui contribue à ce que l'intensité du signal rétrodiffusé varie rapidement avec la profondeur comme on peut le voir sur la figure 1(b,c).

Objectif de la thèse

Le principal objectif de ce travail est la segmentation automatique en 3 milieux (parenchyme du ganglion, graisse environnante, et liquide physiologique) des acquisitions ultrasonores. Cette étape est un verrou à l'analyse automatique par ultrasons quantitatifs des ganglions lymphatiques excisés et par conséquent la détection des métastases par ultrasons quantitatifs.

Contributions

Les principales contributions de cette thèse sont les suivantes:

- Une méthode de prétraitement basée sur les splines cubiques afin de restaurer les échantillons saturés et qui se trouvent principalement dans la graisse ;
- Une analyse statistique de l'enveloppe du signal RF qui identifie la distribution gamma comme la meilleure distribution paramétrique à prendre en compte lors du développement de méthodes de segmentation des ganglions lymphatiques ;
- Deux méthodes de segmentation basées sur une approche par ensemble de niveaux et modélisant l'intensité des voxels par des statistiques gamma locales ;
- Une méthode basée sur les forêts aléatoires qui a été développée pour améliorer l'initialisation des 2 précédentes méthodes.

Organisations de la thèse

La thèse est divisée en 7 chapitres :

1er chapitre : Ce chapitre présente le contexte clinique du projet : L'anatomie du ganglion lymphatique est décrite puis le rôle des ganglions lymphatiques dans l'évaluation du stade du cancer, préalable indispensable au choix du traitement le plus adapté. La méthode de référence s'appuyant sur l'histologie ainsi que les méthodes émergentes invasives et non-invasives sont examinées dont les ultrasons quantitatifs. Enfin dans le contexte des ultrasons quantitatifs, l'importance et les difficultés de la segmentation des données haute-fréquence acquises sur des ganglions lymphatiques humains sont discutées.

2^{e} chapitre : Ce chapitre décrit le protocole expérimental utilisé pour recruter les patients, acquérir les données ultrasonores et les données histologiques qui servent de référence. Le contenu de la base de données est résumé. Les données simulées utilisées dans la suite de l'étude sont également présentées.

3^{e} chapitre : Une méthode de prétraitement basée sur les splines cubiques est décrite afin de restaurer les échantillons saturés du signal RF. Ce prétraitement permet de retrouver dans la graisse une distribution empirique unimodale alors qu'initialement la distribution exhibait bien souvent 2 modes. Une étude statistique de l'enveloppe du signal RF est menée pour déterminer parmi 9 distributions (Rayleigh, Gaussienne, lognormale, Nakagami, Weibull, log-logistique, gamma, loi d'extremum généralisée, gamma généralisée) celles qui modélisent le mieux les distributions empiriques des différents milieux. La distribution gamma généralisée à trois paramètres modélise le mieux les trois milieux. La distribution gamma avec ses deux paramètres a cependant été retenue dans le reste de l'étude car elle présente un bon compromis entre la qualité de la modélisation, la simplicité du modèle et la rapidité de l'estimation des paramètres.

4^{e} chapitre : Ce chapitre s'ouvre par une revue de la littérature concernant la segmentation des données ultrasonores et le problème de la segmentation de données inhomogènes. Puis une nouvelle méthode variationnelle de segmentation appelée LRGDF basée sur une approche par ensemble de niveaux dans laquelle les statistiques gamma locales de l'enveloppe dans les trois milieux sont déterminées à l'aide d'une fonction lisse à support compact. En comparant cette méthode avec une segmentation manuelle réalisée par un expert, on obtient un critère de similarité de Dice élevé. Cette méthode est également plus performante que la même méthode utilisant une statistique

Gaussienne.

5^e chapitre : Afin d'améliorer la prise en compte des inhomogénéités du signal d'enveloppe des ganglions lymphatiques, une seconde méthode appelée STS-LS est décrite. Elle utilise une densité gamma pour modéliser le speckle supposé homogène dans le même milieu et à l'intérieur de coupes transverses qui sont donc perpendiculaires au faisceau ultrasonore. L'intensité des voxels d'un même milieu et à la même profondeur sont modélisés par la même distribution ce qui a pour effet que cette méthode est plus rapide que la méthode LRGDF tout en conservant des segmentations de bonne qualité mesurée à travers le critère de similarité de Dice.

6^e chapitre : Les méthodes LRGDF et STS-LS fournissent de bonnes segmentations mais sont des méthodes qui nécessitent une initialisation. Plus l'initialisation est proche du résultat attendu et plus la segmentation convergera rapidement vers la solution désirée. Ici l'enjeu consiste à améliorer l'initialisation des 2 méthodes STS-LS et LRGDF à l'aide d'une classification par forêt aléatoire afin de conserver des segmentations de bonne qualité tout en diminuant les temps de calcul. Les méthodes hybrides ont été évaluées sur des ganglions colorectaux et la méthode combinant forêt aléatoire et LRGDF est la plus performante. Nous montrons également que les paramètres ultrasonores quantitatifs estimés après segmentation automatique sont comparables aux paramètres ultrasonores quantitatifs estimés après segmentation manuelle par un expert.

7^e chapitre : Après un résumé des résultats obtenus, ce chapitre final décrit les limites de ce travail en particulier l'application de la méthode sur certains ganglions du sein et s'achève sur des pistes à explorer.

Chapter 1

Introduction

1.1 Diagnostic Context

1.1.1 Lymph Node Anatomy (Structure) and Pathology

The lymphatic system, also named second vascular system, is one of the two components of the circulatory system and is an integral part of the immune system. Comprised of lymph vessels (i.e., lymphatics) and lymph organs (i.e., lymph nodes, tonsils, thymus, spleen and bone marrow) as illustrated in Fig. 1.1, the lymphatic system transports lymph fluid throughout the body. Specifically, lymph fluid that contains lymphocytes and other white blood cells is transported through lymphatic vessels to lymph nodes and is then emptied into the bloodstream through the thoracic duct (i.e., the largest lymphatic vessel) [7, 8]. In addition, the lymph organs generate immune cells, monitor the presence of pathogens and facilitate the immune response. Finally, the lymphatic system is in charge of transporting dietary fat from the intestine to the liver [9].

Lymph nodes (LNs) or lymph glands are small, bean-shaped, encapsulated lymphatic organs. They are responsible for filtration of lymph on its way to the blood vascular system and processing of antigens [11, 12]. Their longest dimension is from 1 mm to 20 mm [8]. Approximately 600-800 LNs [13, 14] are distributed throughout the body but they are concentrated in certain areas such as the axilla, mesenteries and groins [8]. Details about the structure inside a LN are shown in Fig. 1.2 [8]. The LN is surrounded by a fibrous capsule where the afferent lymphatic vessels penetrate and drain into the subcapsular and medullary sinus system. Efferent lymphatic vessels emerge from the hilum of the LN in order to transport lymph towards larger lymphatic vessels. A network of blood vessels entering the hilum helps circulating lymphocytes into the LN. The lymphoid parenchyma is composed of a cortex and medulla. The cortex contains collections of lymphocytes comprised predominantly of B cells and some T cells. The B cells mature completely

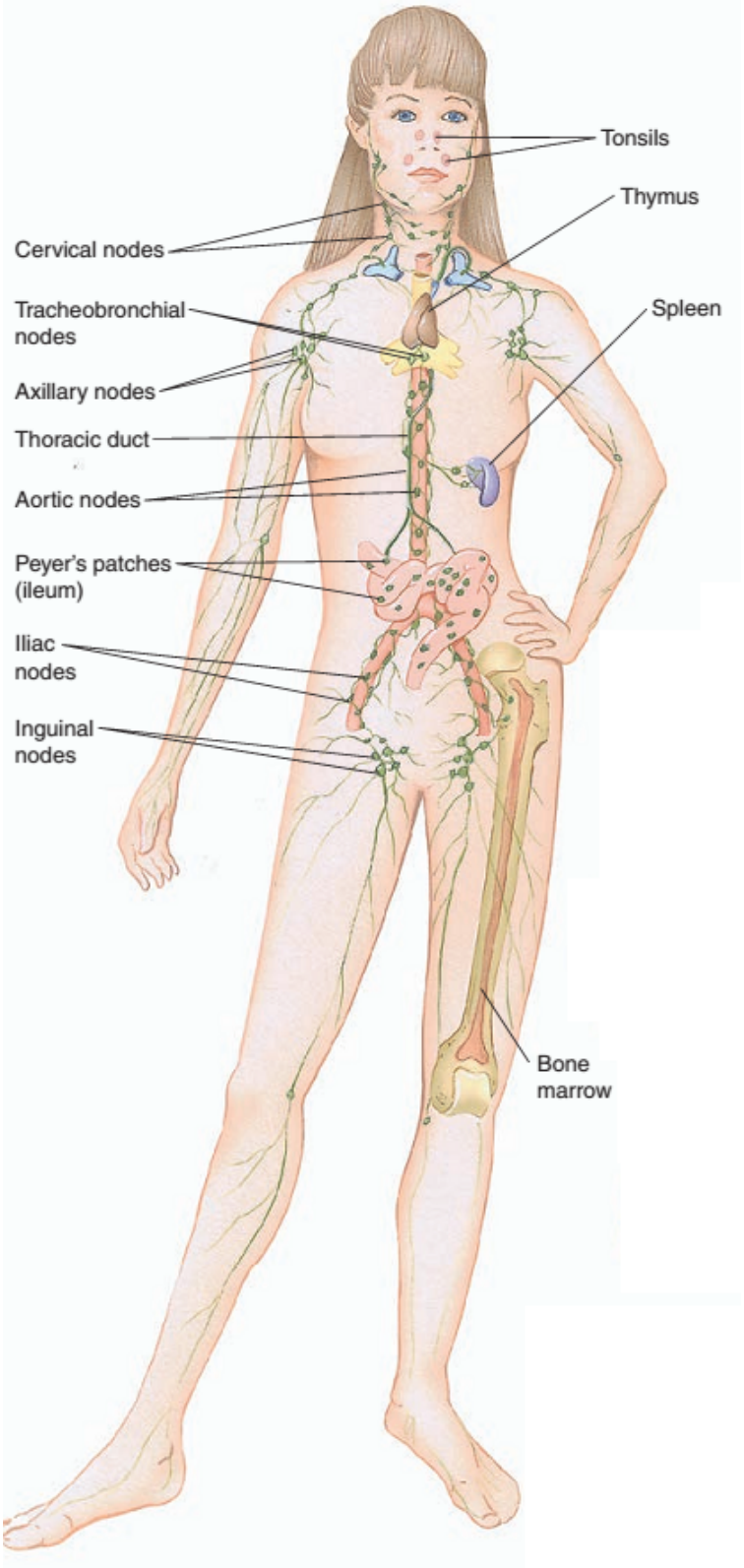

Figure 1.1: Anatomy of the lymphatic system consisting of lymph vessels and lymph organs. The lymph organs include lymph nodes, tonsils, thymus, spleen and bone marrow. From [10]

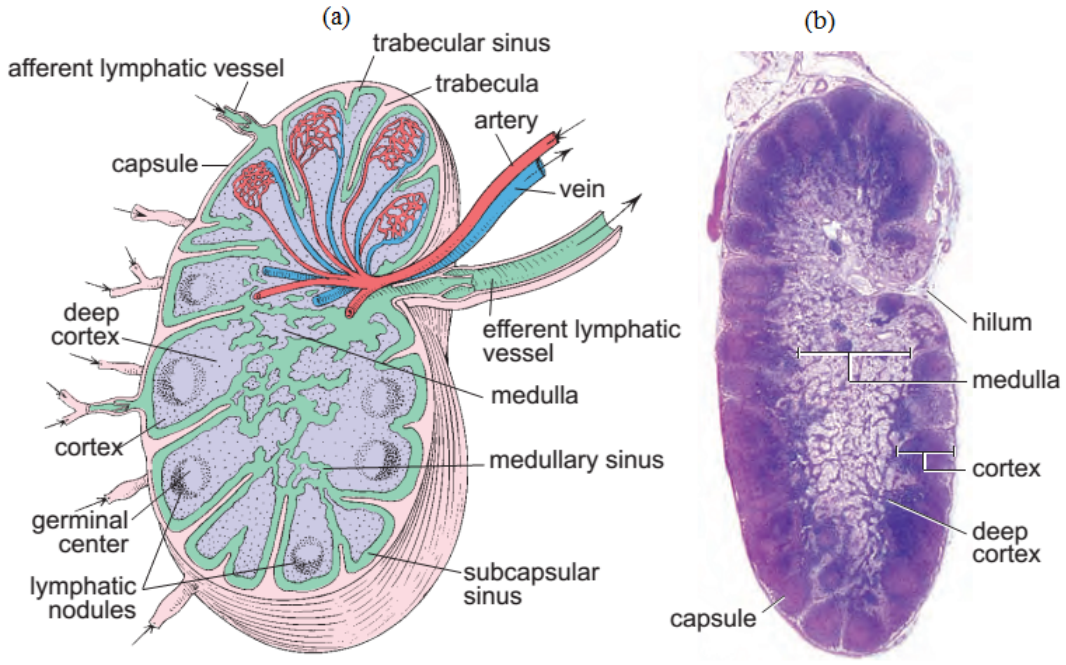

Figure 1.2: Detailed structures of a lymph node (a), and a photomicrograph of a lymph node in a routine hematoxylin and eosin preparation (b). From [8]

within the bone marrow while the T cells exit the bone marrow immature and attain maturity within the thymus.

In addition to their functions in normal physiology, LNs and lymphatic vessels play critical roles in pathological conditions including inflammation and cancer [15]. LNs become greatly enlarged when functional demands are increased. This can occur, for example during intense immune reactions or due to tumor metastasis. In cancer patients, the lymphatic vessels provide conduits for tumor cells to leave the primary tumor and to establish secondary tumors in regional LNs or distant organs [9]. In fact, stromal or immune cells in the LN microenvironment secrete chemokine signals that will attract tumor cells to the LN [15]. In many cancer types, including breast cancer, gastric cancer and colorectal cancer, cancer cells pass through lymphatic vessels at the tumor site and then spread via the lymphatic system: initially to the draining regional LNs (also called the sentinel LNs) and then further to the blood stream and other organs. Therefore, the existence of metastases in sentinel LNs is commonly considered to be the first step in metastatic cancer cell dissemination [9]. Note that a sentinel LN is defined as the first LN in the lymphatic system that receives drainage from an anatomic region and is immunologically responsible for that region [16]; the sentinel LN is thus regarded as the first LN to which cancer cells are most likely to spread from a primary tumor. To detect the sentinel LN, blue dye (e.g., methylene blue) or a radio-tracer is

injected within the region close to the tumor. The surgeon then identifies the node by visual inspection or by using a gamma probe or Geiger counter. The procedure of identifying, dissecting and examining the sentinel LN to determine its status (i.e., containing metastases or not) is referred as the sentinel LN biopsy (SLNB). This regular clinical routine procedure is part of regular clinical routine and is essential for staging disease progression, determining patient prognosis and selecting appropriate treatment strategies [9].

1.1.2 Importance of Accurate Detection of Metastases in Human Lymph Nodes

Accurate detection of LN metastases plays a key role in proper staging and treatment of cancer. For many cancers, the tumor-node-metastasis (TNM) system developed and maintained by the American Joint Committee on Cancer and the International Union for Cancer Control [17] is the established tool for cancer staging. Depending on the stages of cancer, proper treatments, ranging from surgery or local radiation of the primary tumor to systematic treatments involving chemotherapy and radiation, are performed. The TNM staging system is basically based on 3 key information: (1) the extent of primary tumor (T), (2) the status of nearby (regional) LNs (N), and (3) distant metastases (M) [17, 18]. In women with early-stage breast cancer, the status of axillary LNs is one of the strongest prognostic factors, and the current standard of care in the assessment of metastatic spread to LNs is the SLNB [19]. For colorectal cancer patients, the presence of regional LN metastasis plays the main role in guiding the indication of adjuvant therapy [20, 21]. Fig. 1.3 illustrates how the metastases found in LNs relates to the stage determined for patients with colorectal cancer. In relation to the primary colorectal tumor, when metastases are found in the nearby LNs alone or in more distant LNs, then the cancer is in Stages III or IV, respectively. Presence of distant metastases (LNs or organs) automatically categorizes the cancer as Stage IV, even if the primary cancer has not yet infiltrated the wall of the colon or rectum, and it may or may not have spread to nearby lymph nodes. It is worth noting that the SLNB could also be applied to other malignancies such as colorectal cancer [21].

Currently, micrometastases (metastases between 0.2 mm and 2 mm in diameter) and isolated tumor cells (< 0.2 mm or < 1000 tumor cells) are categorized separately from macrometastases (> 2 mm). Furthermore, micrometastases are regarded as a clinically significant and positive detection

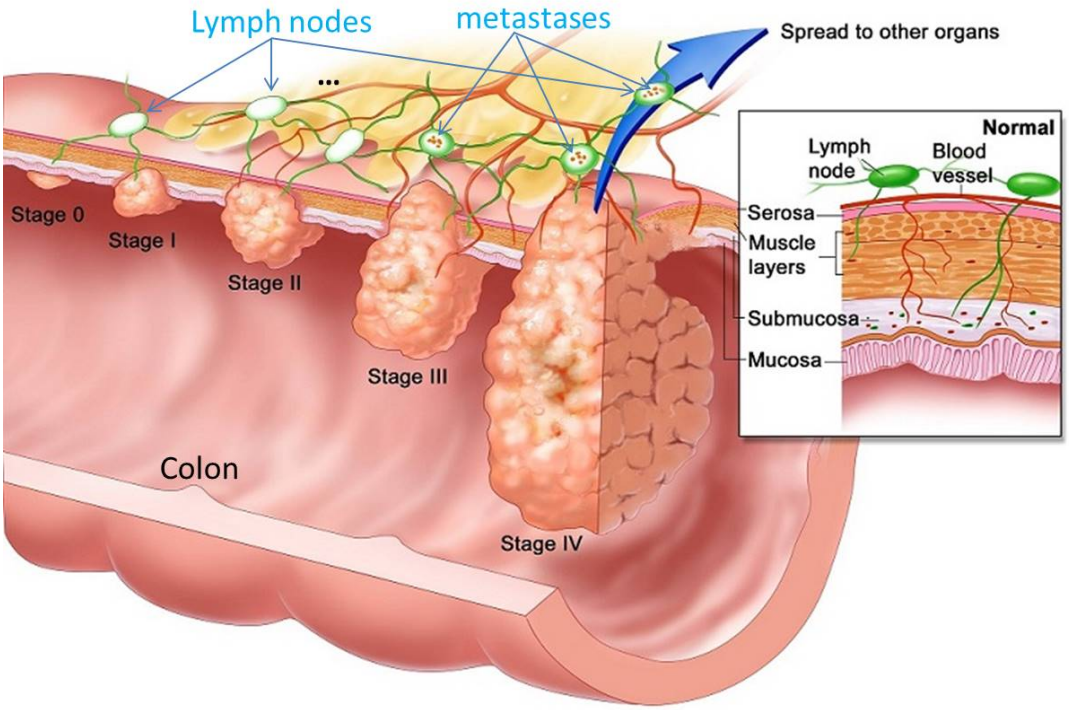

Figure 1.3: Stages of colorectal cancer. A part of the lymphatic system with the lymph nodes is depicted in green color. *(Source: http://www.nih.gov/research-training/advances-colorectal-cancer-research)*

of metastases [4, 15, 17]. Sensitive detection of micrometastases poses a challenge for clinical evaluation and orientation of patient care.

1.1.3 The Current Histological Method for Examining Human Lymph Nodes

In the current standard-of-care, the approach for examining LNs in cancer specimens relies on manual dissection followed by histological assessment. After dissection from cancer patients, LNs are sent to a pathology laboratory in which the LNs undergo either (1) an intraoperative "touch-prep" procedure or (2) a postoperative complete histological preparation and evaluation [22].

In the complete histological procedure, small LNs (< 5 mm) are bisected, and the larger ones are cut into 3 mm pieces. The major steps of the procedure are presented in Fig. 1.4(a) [22]. The procedure can reliably detect metastases in the stained slides extracted from the surfaces of the LN pieces. However, because the complete volume of the LN is not evaluated, clinically significant micrometastases (i.e., 0.2 mm - 2 mm) can go undetected. Furthermore, the complete procedure is a time-consuming process that typically requires 2 - 3 days [22].

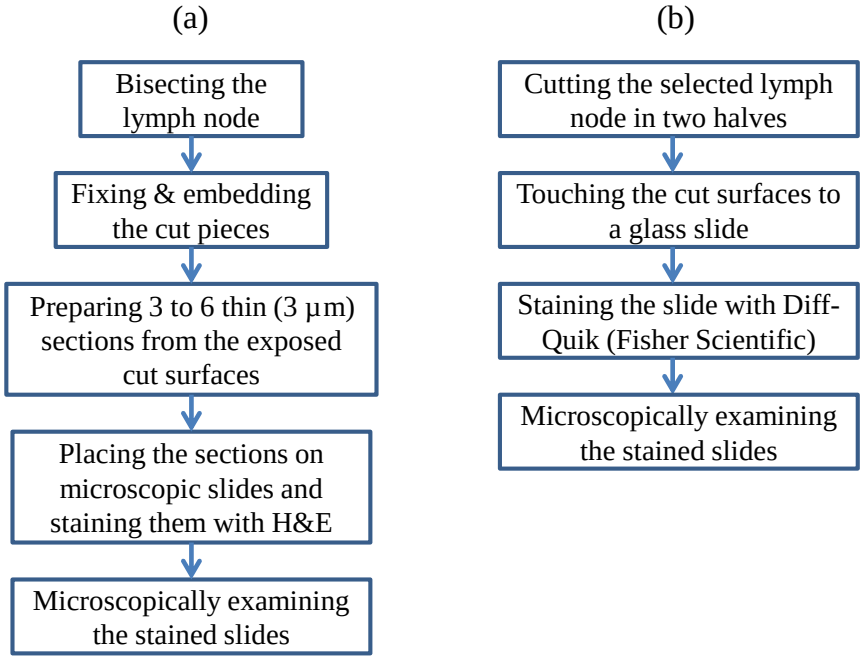

Figure 1.4: Flowcharts showing the main steps of (a) postoperative complete histological preparation and examination, and (b) intraoperative touch prep procedures to determine LN status.

The touch prep procedure illustrated in Fig. 1.4(b) [22–24] is primarily used to evaluate sentinel LNs in breast cancer. The aim of the procedure is to quickly determine (within 10 - 15 minutes [23]) the status of sentinel LNs while the patient is under the effects of anesthesia in an operating room [22]. Note that the LNs experiencing the intraoperative touch prep procedure also undergo the postoperative complete histological procedure. For breast cancer, if the patient has given consent for axillary dissection, and the sentinel LN is categorized as a positive during the touch prep procedure, a complete axillary node dissection will be performed for the anesthetized patient. Otherwise, the patient is rescheduled (typically 1 week after the surgery [24]) in clinic to discuss the results of the postoperative procedure evaluating the sentinel LNs. Clearly, because only the two cut surfaces of the LN are examined, the touch prep procedure can miss micrometastases and/or peripheral metastases in the LNs [21].

Therefore, both standard histological procedures suffer from sampling constraints, i.e. only a small portion of the LN is examined, leaving most of the LNs uninspected. They are not able to detect all metastases in LNs, particularly micrometastases [25], leading to a high probability of false-negative determinations [22]. For colorectal cancer, about 30% of the patients with histopathology-negative LNs (i.e., TNM stages I and II) develop recurrent and/or progressive disease which is likely to be associated with undetected metastatic deposits [20, 21, 26]. Many pa-

tients who were initially diagnosed LN negative following the standard-of-care procedure experience disease recurrence, and after advanced evaluation, they are found to contain isolated tumor cells and/or micrometastases [21, 27].

1.1.4 Emerging Techniques for Metastases Detection in Human Lymph Nodes

1.1.4.1 Noninvasive Methods

Current standard histopathological methods for metastases detection require the dissection of LNs which entails a painful and costly surgical procedure, and is often associated with side effects (e.g., restricted shoulder motion and lymphedema). Thanks to recent advances in medical imaging, several noninvasive methods are emerging to detect and characterize human LNs.

Choi et al. [28] conducted a study on the use of computed tomography and magnetic resonance imaging (MRI) for the evaluation of LN metastasis in early colorectal cancer. Their results showed that a size criterion of metastatic LNs was ≥ 4.1 mm . This criterion was optimal to diagnose LN metastases with a sensitivity of 78.6% and specificity of 75%. The accuracy of differentiation of benign and malignant LNs using LN size alone is low because malignant LN infiltration occurs in up to 30% of cases within LNs of less than 5 mm for rectal, gastric, lung, esophageal and pancreatic carcinoma [29]. To detect axillary LN metastasis in breast cancer, Hwang et al. [30] compared three noninvasive modalities including axillary ultrasonography (AUS), contrast-enhanced MRI (cMRI) and F-fluorodeoxyglucose (F-FDG) position emission tomography/computed tomography (PET/CT). Additional criteria including cortical thickening, irregular or round shape, loss of fatty hilum and high level of F-FDG uptake were considered to differentiate metastatic LNs from normal ones. They concluded, however, that although PET/CT was more accurate than AUS and cMRI, it was inadequate for decision-makings, and therefore none of these modalities could replace SLNB.

Color Doppler ultrasound can help to discriminate metastatic LNs from normal ones by revealing macrovessel architectures [29, 31]. Normal LNs generally present hilar predominant normal vascularity. Contrarily, metastatic LNs exhibit peripheral or mixed vascularity and loss of hilar type of vascularization. In addition, contrast-enhanced color Doppler ultrasound improves the visualization of macrovessels but it does not provide information for evaluating microvessels [29, 32].

Contrast-enhanced ultrasound (CEUS) techniques could improve the visualization of vessels in

LNs to better evaluate the vascular distribution [29]. Recently, Matsuzawa et al. [33] described the use of CEUS with Sonazoid contrast agent to detect sentinel LNs and determine their status. Their results indicated that CEUS with Sonazoid which provided a sensitivity of 81.8% and a specificity of 95.5% was more accurate than contrast enhanced computed tomography and color Doppler ultrasound.

It should be noted that the ability of the detection of LNs using noninvasive imaging methods highly depends the size and position of LNs. Reliable determination of metastatic LNs is difficult because approximately one third of metastases occur in LNs that are not even visible to all imaging methods [29]. Therefore, current noninvasive imaging methods mainly concentrate on the early determination of metastases in detectable LNs to guide neoadjuvant treatment strategies.

1.1.4.2 Invasive Methods to Assess the Entire Lymph Nodes.

The use of more closely-spaced step sections [25] and immunohistochemistry staining [34] may improve the detection of metastasis in LNs [4, 21] as compared to the current standard histopathological methods. In addition, methods including molecular analysis or high-frequency (HF), three-dimensional (3D) quantitative ultrasound (QUS) have been developed to better assess the entire volume of LNs.

Molecular biology-based techniques such as the real-time polymerase chain reaction analysis (RT-PCR) and, more recently, one step nucleic acid amplification (OSNA) have been developed to assess the entire volume of LNs for metastases. In colorectal cancer, techniques based on quantitative RT-PCR for the detection of Keratin 20 mRNA in regional LNs have been investigated by several groups [26, 35, 36]. Their results generally indicate a higher sensitivity of molecular analysis compared to conventional histopathological methods. To detect metastases in axillary LNs in primary breast cancer patients, methods based on molecular detection of cytokeratin 19 mRNA using OSNA have been demonstrated to outperform histopathology of a single tissue section [37–39]. Although very promising, the lack of standardization of molecular analyses makes comparison of different studies difficult. Therefore, techniques based on molecular analyses require further prospective studies before being adopted in clinical routine [4, 21].

HF, 3D QUS methods [1, 2, 4, 22] have been developed to examine the entire-volume of LNs with finer spatial sampling in order to better detect LN metastases throughout the LN. Using HF

ultrasound (i.e., > 15 MHz), QUS methods can provide an evaluation of tissue microstructures. By performing a 3D ultrasound scan, data can be acquired from the full LN volume. Therefore, the methods can evaluate the whole LN to detect micrometastases as well as macrometastases. Results [4] have demonstrated that QUS methods can provide high sensitivity and specificity for detecting metastases in colorectal and axillary LNs. The QUS methods will be described in more detail in Section 1.2.2.

1.2 Emerging Quantitative Ultrasound Techniques for Lymph Node Characterization

1.2.1 Fundamentals of Ultrasound

Ultrasound is a widespread medical imaging modality with many advantages compared to other imaging modalities. Major strengths of ultrasound are its abilities to reveal anatomy, the dynamic movement of organs, and details of blood flow in real-time. It is the only non-invasive medical imaging modality that can provides true real-time images. Furthermore, ultrasound is low cost, safe (because it does not use ionizing radiation), easy to transport (portable) and to use (adaptable).

Ultrasound is the term corresponding to mechanical waves propagating at frequencies above the range of audible sound frequencies (i.e., > 20 kHz). When an ultrasound pulse propagates within a biological medium, the wave is modified as it travels through the tissues. The ultrasound wave is absorbed by media and reflected at interfaces encountered along its path. Absorption refers to the phenomenon when some energy of the ultrasonic wave propagating through tissue is absorbed by the tissue and converted to heat. Additional energy is lost from the propagating wave as energy is scattered away from the wave propagation path. The attenuation coefficient of a medium describes the amount of lost wave intensity per distance traveled due to the different attenuation phenomena. The attenuation coefficient in soft biological tissues increases as a function of the ultrasonic wave's frequency.

Biological tissue is not acoustically homogeneous, i.e., the acoustic impedance, which is defined as the product of the density and the propagation speed of sound, varies within the medium. Therefore, when an ultrasonic beam propagates in the tissue, part of it is reflected or scattered due to

discontinuities in the acoustical properties of the medium [40]. Note that scatterers are microscopic inhomogeneities (i.e., cell nuclei, fiber, etc) that are acoustically different from their surrounding medium. Echoes are produced, that can be due to specular reflections and diffuse scattering [40].

- Specular reflections enable the visualization of boundaries between two acoustically different regions. They occur when an ultrasound pulse reaches boundaries where the size of the inhomogeneities in acoustical impedance is larger than the wavelength of the acoustical signal.
- Diffuse scattering occurs as the ultrasound pulse encounters scattering structures with sizes smaller than the acoustic wavelength. Diffuse scattering gives rise to speckle phenomenon.

In reflection mode, ultrasound images are generated by transmitting acoustic pulses into the imaged object using an ultrasound probe (transducer), and then recording the echoes backscattered from structures within the object as the pulses propagate through them. Contrast between tissues in ultrasound images can result from differences in their populations of scatterers. Specifically, a medium with few or weak scatterers will appear dark in an ultrasound image. Contrarily, a dense scatterering medium or a medium containing strong scattering structures will appear bright.

Speckle

Speckle gives ultrasonic images their characteristics granular appearance [41]. The speckle phenomenon depends on the resolution cell of the ultrasonic imaging system. The resolution cell, which is defined by the beam cross-sectional area and the transducer pulse duration [40, 42], corresponds to an elementary volume from which the ultrasound system cannot resolve the contribution of individuals scatterers. The dimensions of the resolution cell vary with its position in space because the emitted ultrasound beam is usually focused at one particular point.

Speckle is formed by backscattered echoes of randomly or coherently distributed scatterers within a resolution cell within the insonified media [43]. It also depends on the nature of the involved scatterers, such as their mass density, their spatial distribution and their echogeneity. Speckle can be fully developed [43] or partly developed [44]. Fully developed speckle refers to the situation when each resolution cell contains a large (or infinite) number of randomly located scatterers. When the number of scatterers within a resolution cell is low (i.e., effective number of scatterers is smaller than 10) , the speckle is defined as partially developed.

Quantitative Ultrasound

Quantitative ultrasound (QUS) is the term referring to techniques that provide parameter estimates relating to small scale tissue structures based on ultrasonic backscattered radio frequency (RF) signals. Echo signals are produced by reflections from interfaces between acoustically different regions (macrostructures, with dimensions > wavelength) and by coherent and incoherent scattering from small scale tissue structures (microstructures, with dimensions < wavelength) and recorded by the ultrasound imaging system as the RF signals. Therefore, these echo signals contain frequency-dependent information about the microstructures of tissues as well as the nature of underlying scatterers.

Conventional ultrasonic images (B-mode images) are constructed from the log-compressed RF signal envelope. This processing removes the frequency-dependent content available in the RF echo signals. B-mode images display tissue structures with dimensions greater than wavelength; however, in order to evaluate the microstructures of tissue using the ultrasonic signals, the frequency-dependent information available only in the original RF signals must be used.

Thus, QUS analysis relies on access to the RF signals prior to processing for the production of B-mode images. By transforming the RF echoes in the frequency domain using the Fourier transform, the frequency dependence of the echo signals can be evaluated and, using appropriate scattering models, can be related to the microstructural properties of the biological media.

Several parameter estimates have been obtained using QUS techniques [45, 46]. Using spectral analysis of the raw backscattered RF signals, spectral slope and intercept [47, 48], effective scatterer size and acoustic concentration [49, 50] have been successfully used to characterize different aspects of tissue microstructures. Note that acoustic concentration is the product of the scatterer number density and square of the relative acoustic impedance. The relative acoustic impedance is the ratio of the acoustic impedance difference between the background and the scatterers to the acoustic impedance of the background. By modeling the echo envelope with proper statistical distributions, effective number of scatterers per resolution cell [44], and the ratio of coherent to diffuse signal [51] can be derived and thus applied to tissue characterization.

1.2.2 Quantitative Ultrasound for Detecting Metastases in Human Lymph Nodes

Our laboratory has been part of a collaborative project since 2007 working to develop techniques using HF QUS to detect LN metastases. This research consortium is directed by Ernest Feleppa of Riverside Research, New York, USA. Previous work from this collaboration [1–4] has demonstrated the potential of a high-frequency (HF), three-dimensional (3D), QUS method (Fig. 1.5) for reliably evaluating the entire LN volume to detect metastases. In these previous studies, radio-frequency (RF) echo signals were acquired from entire LNs using HF ultrasound (HFU) (i.e., > 15 MHz) so that tissue microstructural properties could be assessed to detect LN micrometastases. The QUS method consists of two major steps: 3D segmentation and 3D QUS-parameter estimation.

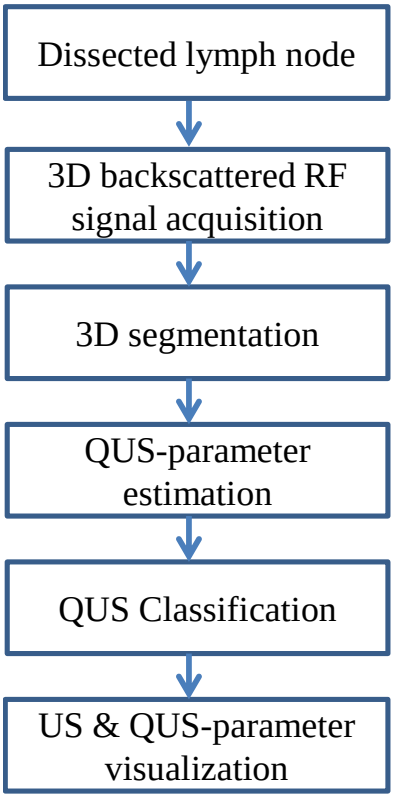

Figure 1.5: Steps used in QUS methods for detecting metastases in dissected human LNs.

Details describing the acquisition of these data are presented in Chapter 2. In brief, the gross surgical specimen was dissected and immersed in normal saline (NS) for RF signal acquisition. After dissection, the bean-shaped LN parenchyma (LNP) remains surrounded by a thin layer of perinodal fat (PNF). Accurate segmentation of the three media (LNP, PNF and NS) is necessary to

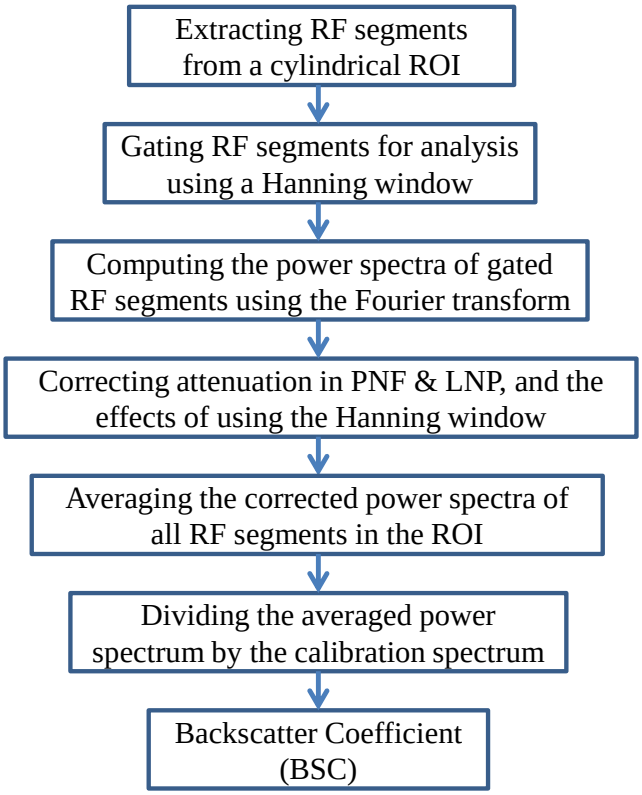

Figure 1.6: The major steps for estimating the backscatter coefficient (normalized and attenuation-corrected local power spectrum) of the backscattered RF signals within a cylindrical ROI.

correct for attenuation in each medium and to restrict QUS processing to the LNP. Furthermore, successful segmentation provides LN dimensions, shape and volume data, which may also be useful as bio-markers of cancer.

The second step of the QUS method computed a feature set from the LNP data after compensation for attenuation effects. This feature set consisted of thirteen QUS parameters associated with tissue microstructures in the LNP. The four most effective parameters (spectral intercept, spectral slope, effective scatterer sizes and acoustic concentration) were estimated by fitting two different scattering models to attenuation-compensated and normalized local power spectra (which can be related to backscattered coefficients [5]). Fig. 1.6 illustrates the process of computing the backscattered coefficient. Four other parameters were estimated from the backscattered echo envelope by considering its probability density functions (PDF) to be Nakagami and Homodyned-K. Another five parameters were estimating using the modified quantile-quantile plot [52] by quantifying the difference between the echo envelope PDFs and the Rayleigh PDFs.

In a database of 172 LNs of colorectal- and gastric-cancer patients [4], the area under the receiver-

operator characteristic curve (AUC) was computed to assess the classification performance. A high AUC value (i.e., > 0.95) was obtained. Despite these promising results, application of the QUS method for metastasis detection is currently limited by time-consuming visual inspection and manual correction required by the existing semi-automatic 3D segmentation method [6]. Developing a more-robust, 3D, automatic segmentation approach is necessary to make the QUS method practical in the clinical setting.

1.3 Segmentation

1.3.1 Overview

Segmentation is a well-established problem involving partitioning an image into different meaningful regions which are application-dependent. The objective of segmentation is well-defined; however, depending on the quality and characteristics of images (data), segmentation techniques range from simple (e.g., thresholding) to complicated ones, requiring complex mathematical formulation to integrate prior information (intensity distribution, shape, texture, etc.) derived from the segmented image and/or image datasets (i.e., segmentation based on machine learning techniques). Because of the inherent poor visual quality, automatic segmentation of US data is difficult. Additional challenges including speckle, low contrast between tissue regions of concern, lack of explicit boundaries, occlusion caused by surrounding tissues and attenuation make the automatic US segmentation one of the most active areas of researches in medical imaging with a wide range of segmentation methods being developed. We will further discuss state-of-the-art segmentation techniques in Section 4.1.1.

1.3.2 Specific Challenges for Segmentation of High-frequency Ultrasound Data from Human Lymph Nodes

In addition to the challenges outlined above, high-frequency ultrasound (HFU) data from human LNs suffer from important focusing and acoustic-attenuation effects because the data were acquired using a single-element, spherically-focused HF transducer. To obtain the fine-resolution backscattered signals for the evaluation of LN microstructures to detect micrometastases, a HF

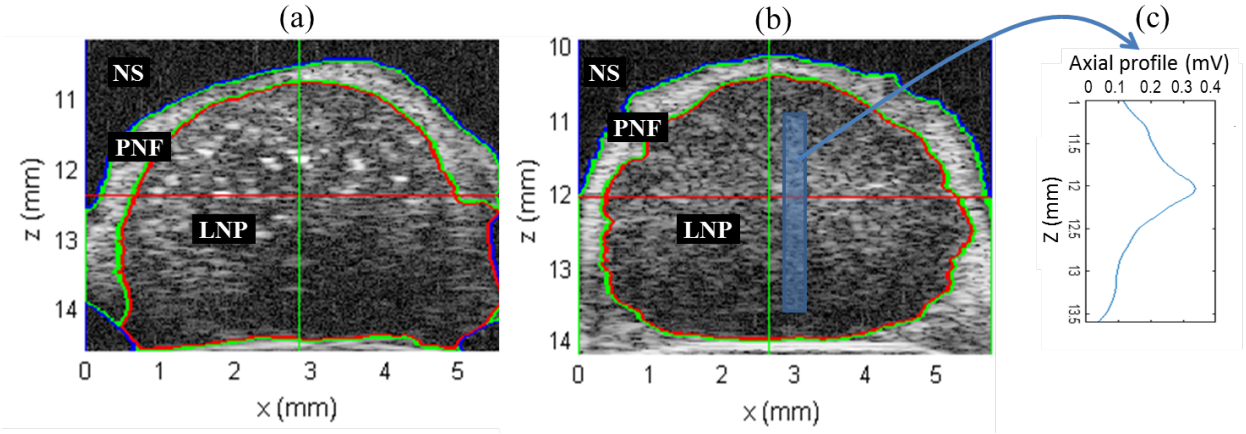

Figure 1.7: HFU B-mode data presenting a 2D section (in the x-z plane) of volumetric data acquired from excised metastatic (a) and nonmetastatic (b) LNs. Regions that were segmented using the proposed STS-LS method (presented in Chapter 5) are delineated and identified with labels as LNP, PNF and NS. (c) The smoothed axial profile of radio-frequency signal envelopes (i.e., radio-frequency signal envelopes vs. depth) within the rectangle shown in (b) illustrates the inhomogeneities of the intensity with depth.

transducer was used, leading to the high signal attenuation. This causes low signal-to-noise levels with depth, especially at the deepest regions explored for large LNs as depicted in Fig. 1.7(a). Furthermore, to increase transducer sensitivity and performance at analysis regions, the spherically-focused transducer was used. With a focused transducer, the beam profile converges to a focal point and then diverges at an equal angle beyond the focal point as shown in Fig. 1.8. As a result, the backscattered signals and thus the echo envelope evolved significantly with imaged depth as illustrated in Fig. 1.7(b,c).

In addition, as presented in Section 1.1.1, LNs have a complicated structure with different acoustic

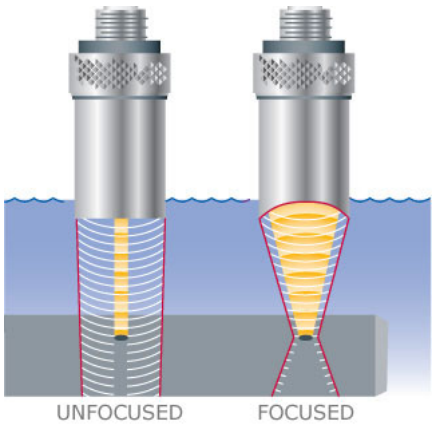

Figure 1.8: Single-element, spherically-unfocused and -focused transducers. *Source: http://www.olympus-ims.com/en/ultrasonic-transducers*

properties. Therefore, backscattered echo signals from LNs, especially the metastatic LNs, tend to be highly inhomogeneous. Furthermore, the great variation in the shape of between different LNs, particularly in axillary LNs, makes it difficult to incorporate shape priors into segmentation.

1.4 Objectives of the Thesis

The main objective of the thesis is to investigate if local and parametric modeling of speckle statistics can contribute to better and faster segmentation of high frequency ultrasound data for the detection of micro metastases in human LNs using QUS.

First, the probability density functions (PDF) best modeling the echo signal envelope (or speckle statistics) from the three media (i.e., LNP, PNF and NS) in the LN HFU data is identified (Chapter 3). Developing an US image segmentation method depends strongly on how the speckle is interpreted, i.e., speckle can be suppressed but it can be used as a source of information [41]. In this thesis, we adopt the latter strategy and exploit speckle information for segmentation.

Subsequently, two novel level-set segmentation methods (Chapter 4 and 5) that employ gamma PDFs to locally model the speckle statistics in two different manners are developed to segment the three media. Although the two level-set segmentation methods provide satisfactory segmentation results on our dataset, we would like to enhance them. Furthermore, the level-set methods require an initialization, the closer the initialization is to the sought boundaries, the faster the segmentation will converge, thus reducing the execution time. We thus consider to integrate into the segmentation methods the information that we have acquired a large LN dataset, and many LNs have been manually segmented by experts. Therefore, Chapter 6 presents hybrid segmentation methods in which we implement random forest classification (RFC) with new features to obtain a preliminary segmentation which is considered as initialization for the level-set segmentation methods. Following this approach, the level-set segmentation methods are applied to refine the segmentation provided by the RFC so that automatic segmentation is ultimately obtained. The agreement between QUS parameters estimated from manually segmented LNs and from automatically segmented LNs is also assessed to investigate if the QUS estimates are maintained when automatic segmentation is applied to evaluate excised LN data. Finally, limitations remaining to overcome and other applications that may benefit from the work presented in this thesis in the future are discussed.

Chapter 2

High-resolution Databases Characterizing Human Lymph Nodes

This chapter describes the experimentally-acquired and simulated databases that were used throughout this thesis. Within the NIH project CA100183 (PI, Pr Ernest Feleppa, Riverside Research, New York NY), human lymph nodes (LNs) were removed from patients at the Kuakini Medical Center (KMC) in Honolulu, HI. The patient population, techniques used for LN dissection, histological preparation and high-frequency ultrasound (HFU) data acquisition are briefly summarized in Section 2.1. More detailed descriptions on the preparation of high-frequency ultrasound and histology databases can be found in previously published works [1, 2]. Note that the Institutional Review Boards (IRBs) of the University of Hawaii and KMC approved the participation of human subjects in the study. All participants were recruited at KMC and gave written informed consent as required by the IRBs.

For developing segmentation methods, it was necessary to have additional data with well-known characteristics. Therefore, techniques were put into place to simulate data sets that well mimic the experimentally-acquired LN data (with realistic speckle, attenuation and focusing effects). The methods used to obtain these simulated data are described in Section 2.2.

2.1 Data Acquired from Human Lymph Nodes

2.1.1 High-frequency Ultrasound Data

LNs were dissected from patients with histologically-proven primary cancers (e.g., breast, colorectal or gastric cancer) at KMC. Table 2.1 summarizes the number of patients, LNs and LN status

Organ	Patients	Total LN	Cancerous LN	Non-cancerous LN
Breast	199	418	71	347
Gastric	33	127	32	95
Colorectal	169	445	74	371
Other	25	58	20	38
Total	426	1048	197	851

Table 2.1: Clinical LN database of human lymph nodes

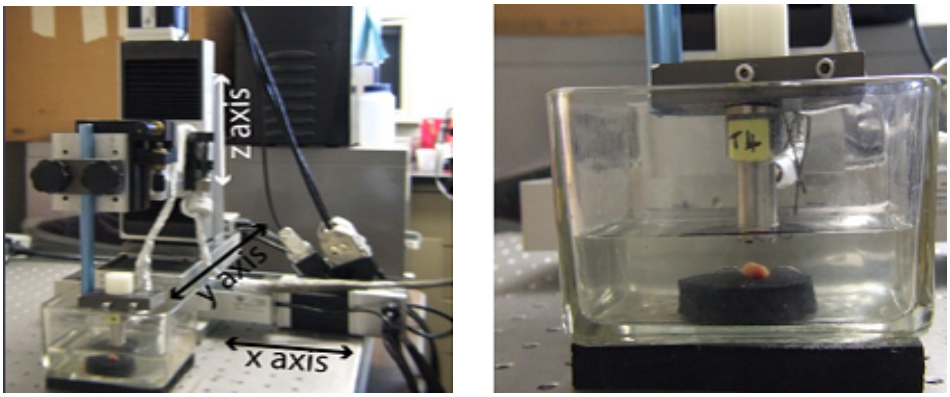

Figure 2.1: Data acquisition set-up showing scanning axes (left) and the excised LN in normal saline solution (right). (Taken from [53])

that we have acquired for each type of cancer. The surrounding perinodal fat (PNF) was then manually removed from the LNs. Isolated, freshly dissected LNs were individually placed in a normal saline (NS) solution at room temperature and scanned. Sizes predominantly ranged from 2 to 12 mm and LNs were surrounded by a remaining thin layer of PNF. The scanning system along with a LN being scanned is presented in Fig. 2.1. Radio-frequency (RF) signals were acquired using a single-element transducer (PI30-2-R0.50IN, Olympus NDT, Waltham, MA) with a 12.2 mm focal length, an F-number of 2 and a center frequency of 25.6 MHz. The theoretically predicted axial and lateral resolutions of the imaging system were 85 μm and 116 μm, respectively. Thus, the volume of the 3D resolution cell can be estimated to be $\pi \times 85 \times (116/2)^2 \times 10^{-9} \approx 8.98 \times 10^{-4}$ mm^3. The RF echo signals were digitized at 400 MS/s using an 8-bit Acqiris DB-105 A/D board (Acqiris, Monroe, NY). Volumetric data were acquired from each LN by scanning adjacent planes with a uniform plane and A-line spacing of 25 μm in both lateral directions. Envelope data were derived from the digitized RF data by applying a Hilbert transform.

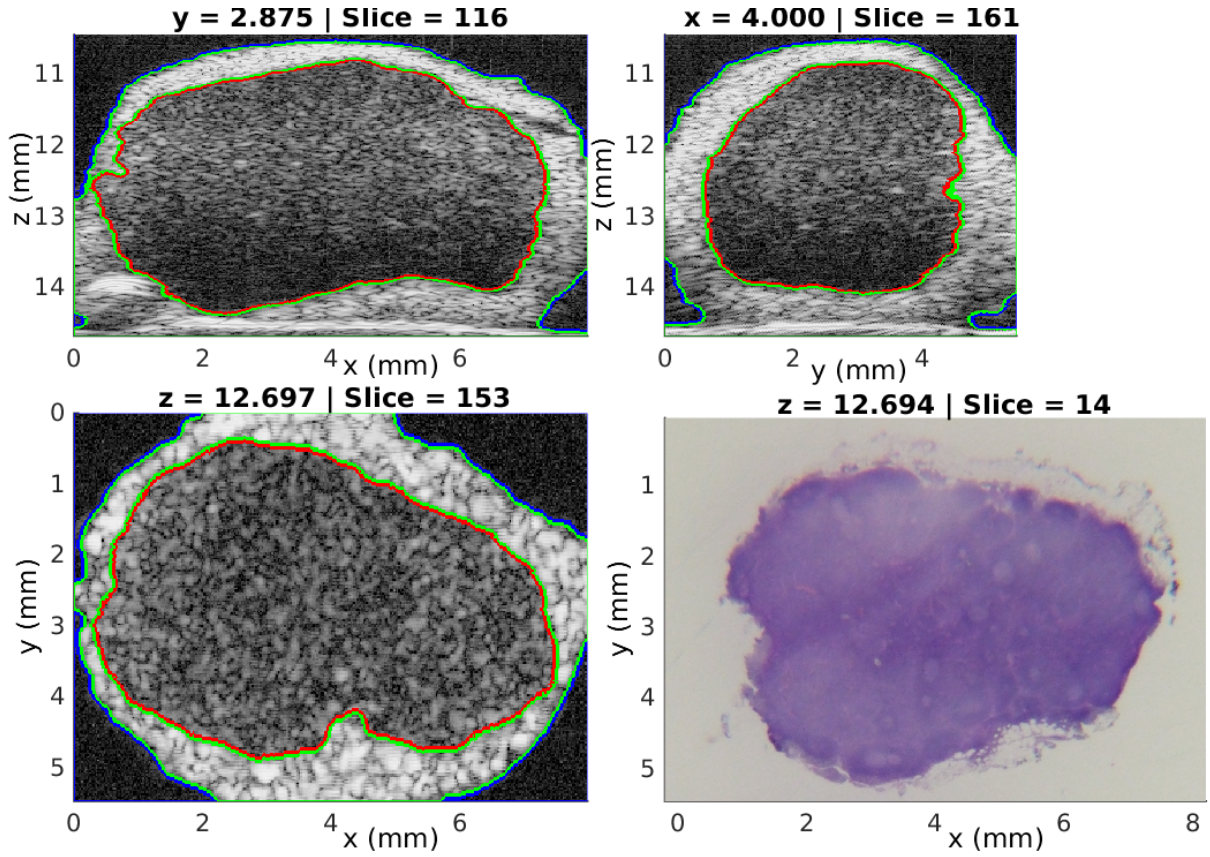

Figure 2.2: Three orthogonal cross-sectional views showing the segmentation of three regions overlaid on B-mode data (40-dB dynamic range) acquired from a non metastatic LN of a colorectal cancer patient. The RFC_STS-LS method presented in Chapter 6 was used to segment the LN. The LNP and PNF regions are demarcated by the red curve and green curve, respectively; while the NS region is limited by the blue curve. The bottom right panel displays the histology image co-registered with the bottom left B-mode image.

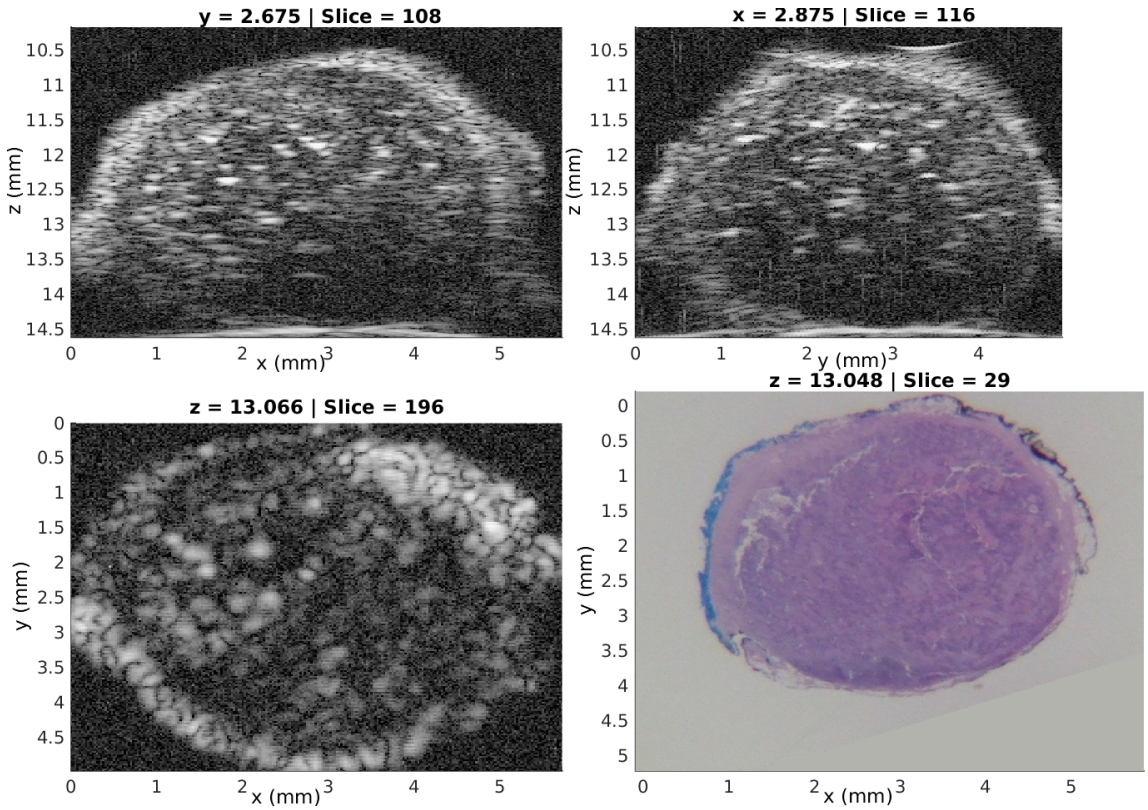

Figure 2.3: Three orthogonal cross-sectional views of B-mode data (40-dB dynamic range) acquired from a metastatic LN of a colorectal cancer patient. The co-registered histology images is also shown.

2.1.2 Histology Data

To overcome the problems of sampling constraints associated with the current standard of care, a non-standard histology procedure was employed to acquire fine spatial sampling, which is important to avoid missing clinically significant metastases. Furthermore, fine spatial sampling enables co-registration of 3D ultrasound volume with 3D histology volume, necessary to evaluate the reliability of the QUS methods for detecting metastatic regions within the LNs.

Briefly, after US data acquisition, the scanned LN was inked to provide visual reference for recovering orientation with respect to the 3D ultrasound scan. To estimate the size of LN, the entire LN was photographed using a digital camera (FujiFilm FinePix S9100, Fuji Photo Film, Tokyo, Japan) equipped with Hoya +2 and +4 close-up lenses (Hoya Corp., Tokyo, Japan). The next steps involved cutting the LN approximately in half, fixing the two half-nodes in 10 % neutral-buffered formalin and embedding them in paraffin. The two half-nodes were then microtomed into paired 3 μm thin sections at every 50 μm for nodes smaller than 5 mm or 100 μm for larger nodes. In other words, a step size (distance between two consecutive set of pairs) for nodes smaller than 5 mm and for larger nodes was 50 μm and 100 μm, respectively. At each step, sets of 3 to 5 pairs of 3 μm sections were obtained depending on LN size. For light-microscopic examination, each 3 μm thin section was placed on a microscope slide and stained with Hematoxylin and Eosin (H&E). To obtain histological images of the two lymph-node halves, each H&E stained slide was photographed using the same digital camera used for estimating LN size (i.e., FujiFilm FinePix S9100) and a high-quality, high-throughput slide scanner (NanoZoomer, Hamamatsu, Japan) with a pixel resolution of 0.46 μm.

Fig. 2.2 displays three orthogonal B-mode images of a metastatic LN together with a co-registered histology image using LymphExplorer [54]. Three regions (LNP, PNF and NS) were automatically segmented using the RFC_STS-LS segmentation method described in Chapter 6 of the thesis. Furthermore, Fig. 2.3 shows three cross-sectional views of B-mode data acquired from a metastatic LN as well as a corresponding histology image. In general, data acquired from metastatic LNs are more inhomogeneous than those acquired from nonmetastatic LNs, and thus automatic segmentation of such data is more challenging.

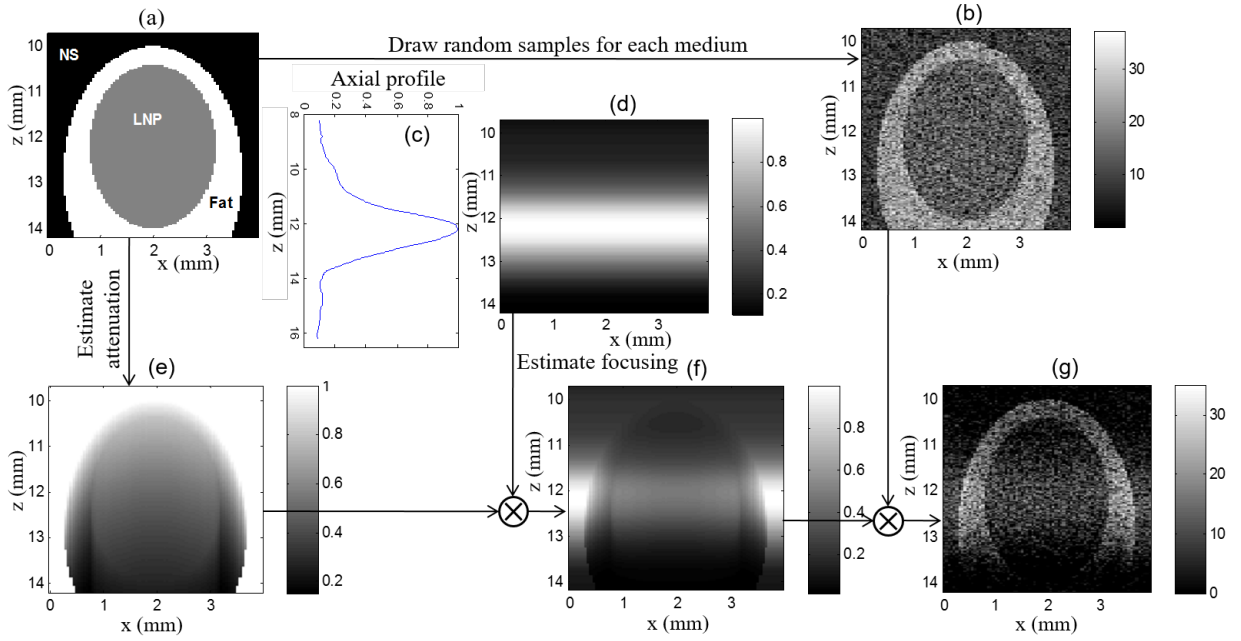

Figure 2.4: Illustration the generation of simulated data affected by focusing and attenuation. (a) Ground truth data with three media: LNP, PNF and NS. (b) B-mode display of original envelope data distributed according to gamma distributions for the 3 media. (c) Axial profile of the focused transducer. (d) A slice generated from the axial profile. (e) The attenuation estimated for 3 media. (f) The combination of focusing and attenuation. (g) B-mode display of simulated data affected by focusing and attenuation.

2.2 Simulated Ultrasound Data based on Speckle Statistics

Simulated data were generated to present the same topology as the LN data, i.e., simulated data sets were comprised of three regions (LNP, PNF and NS) as shown in Fig. 2.4(a). As will be presented in Chapter 3, the gamma (GA) distribution well describes envelope statistics for data from LNP, PNF and NS regions. Therefore, data were initially simulated for each type of tissue region as random numbers distributed according to the GA distribution. The GA-distribution parameters for each region were chosen to be approximately those for each corresponding region of the LN envelope data. Specifically, the shape and scale (a, b) parameters for the LNP, PNF and NS regions were $\left(2.25, 1.1\times10^{-4}\right)$, $\left(2.49, 2.9\times10^{-4}\right)$ and $\left(2.90, 0.5\times10^{-4}\right)$, respectively. The size of the data was selected to be the size of a typical LN, i.e., 4.5 mm $\times$ 4 mm $\times$ 5 mm. Fig. 2.4(b) shows a B-mode image (log compression with 40 dB dynamic range) of the simulated data with no simulation of the attenuation and focusing effects $A_0(\mathbf{x})$. Note that $\mathbf{x} = (x_1, x_2, x_3) = (z, x, y)$ is a spatial variable representing a voxel in 3D space.

To simulate the focusing effect, we employed the experimentally measured axial beam-profile

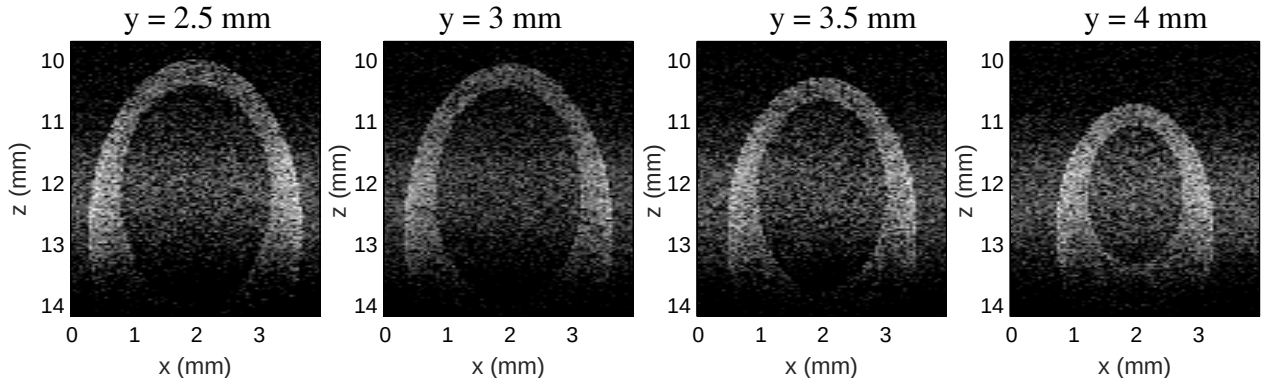

Figure 2.5: B-mode images (40-dB dynamic range) extracted from the simulated data.

curve $\left(F_{\text{profile}}(x_1)\right)$. This profile was estimated based on the amplitude of the specular echo from a planar interface placed at different axial positions with respect to the transducer as described in [1]. The beam profile is presented schematically in Fig. 2.4(c). A slice constructed from the axial profile of the curve is presented in Fig. 2.4(d). The attenuation was negligible for NS. It was assumed to be typical of soft tissue, 0.5 dB/MHz/cm, for LNP and was based on a previous measurement of 0.97 dB/MHz/cm for PNF [1]. Therefore, at the center frequency of 25.6 MHz and after conversion from decibels to nepers, the attenuation coefficients of PNF, α_{PNF}, and LNP, α_{LNP}, were 2.859 Np/cm and 1.474 Np/cm, respectively. By taking into consideration the round-trip propagation, the final simulated signal, A, was obtained using the following equation:

$$A(\mathbf{x}) = A_0(\mathbf{x})\, F_{\text{profile}}(x_1) \exp\left(-2\left(\alpha_{\text{PNF}} d_{\text{PNF}}(\mathbf{x}) + \alpha_{\text{LNP}} d_{\text{LNP}}(\mathbf{x})\right)\right), \tag{2.1}$$

where A_0 is the random numbers distributed according to the GA distribution, and F_{profile} is the axial profile of the focused transducer; d_{PNF} and d_{LNP} are, respectively, the thickness of PNF and LNP layers that the sound propagates through. Fig. 2.4(e) shows the effect of attenuation in the 3 encountered media, and Fig. 2.4(f) presents the combination of the attenuation and focusing effects. Finally, Fig. 2.4(g) shows the B-mode image of the slice simulated in panel Fig.2.4(b) after integration of the attenuation and focusing effects. Fig. 2.5 presents a few B-mode images extracted from a typical 3D simulated LN data set.

The experimentally acquired databases combined with simulated data sets will be used throughout this thesis to evaluate the performance of the novel automatic segmentation techniques. Prior to development of segmentation techniques, it was necessary to well characterize the data distribution in the different types of tissues encountered. This characterization is the subject of the next chapter.

Chapter 3

Statistical Modeling of High-frequency Ultrasound Data from Human Lymph Nodes[1]

3.1 Introduction

Modeling accurately the statistics of ultrasound echo envelope signals is important for applications of tissue segmentation and classification. Statistical distributions can be employed in developing segmentation methods based on maximum likelihood or maximum *a posteriori* (MAP) approaches. Furthermore, the estimated parameters of the statistical distributions of the echo envelope can provide information regarding tissues of interest and could potentially be used for characterizing different tissue types.

Significant work has been performed to investigate the specific statistical properties of ultrasound echo-signal data within the common clinical frequency range (<15 MHz). Zimmer *et al.* [56] used the lognormal distribution to model speckle in liver images. Shankar *et al.* [57] proposed Nakagami and K distributions to model the backscattered echo signals from tissue, and the distribution parameters then were used to classify breast masses. A family of four distributions (gamma, Weibull, normal and lognormal) was evaluated by Tao *et al.* [58] for modeling the speckle in cardiac ultrasound images. The study of Tao indicated that the gamma distribution provided the best fit to the data and had a low misclassification rate in distinguishing between blood and adjacent soft tissue. Nillesen *et al.* [59] investigated the envelope statistics of blood and myocardium in

[1]This chapter is adapted from Thanh Minh Bui, Alain Coron, Jonathan Mamou, Emi Saegusa-Beecroft, Tadashi Yamaguchi, Eugene Yanagihara, Junji Machi, S. Lori Bridal, and Ernest J. Feleppa, "Modeling the Envelope Statistics of Three-dimensional High-frequency Ultrasonic Backscatter from Dissected Human Lymph Nodes", Japanese Journal of Applied Physics, vol. 53, pp. 07KF22-1–11, 2014 [55]

echocardiographic images. Nillensen's study showed that the gamma distribution outperformed other distributions (K, Nakagami, inverse Gaussian and Rayleigh) in describing the speckle statistics of blood and myocardium. To diagnose liver fibrosis, two and three component Rayleigh mixture models were proposed to model statistics of the ultrasonic envelope data acquired on this organ. [60–62]. Recently, Anquez *et al.* [63] proposed the use of the gamma distribution to model the statistics in amniotic fluid and fetal tissues of antenatal 3D ultrasound images. Anquez then formulated a segmentation method by integrating the gamma statistical model of the intensity distribution using the MAP approach to maximize the probability $p(P(\Omega)|I)$ of the partition $P(\Omega)$ given the image I. Only a few studies have evaluated the statistics of HFU data. Raju *et al.* [64] conducted a study on the statistics of the envelope of two-dimensional (2D) HFU backscatter signals from human skin. Raju's results indicated that the Weibull, K and generalized gamma distributions were capable of modeling the envelope statistics well. However, the shape parameters of the three distributions were unable to discriminate between data acquired in healthy skin and skin affected by dermatitis [65].

The aim of this chapter is to identify probability distribution functions (PDFs) that best model the envelope of 3D HFU data acquired in LNP, PNF and NS. Once fully characterized, information regarding PDFs in different regions of the LNP and the surrounding media can be applied to develop a LN segmentation method using the MAP approach [63, 66]. Furthermore, detailed characterization of parameters describing the PDF of non-cancerous vs. metastatic LNP may potentially also contribute to more-accurate QUS-based characterization of LNs. To avoid confusion, it is worthwhile mentioning that in this thesis, statistical modeling and segmentation methods were evaluated using envelope data (i.e., before log compression), but LN images (e.g. Figs. 3.1, 4.3, etc) are shown in B-mode display (log compression with 40 dB dynamic range) for good contrast.

3.2 Theory

3.2.1 Probability Density Functions

The analytic signal associated with the signal backscattered from an ensemble of discrete scatterers in the absence of attenuation can be expressed at each instant as [64] $Re^{j\varphi} = \sum_{i=1}^{N} a_i e^{j\theta_i}$, where a_i and θ_i, respectively, are the amplitude and phase of the backscattered signal from an individual

Table 3.1: Expression of the nine investigated PDFs. Here $\phi(z) = \exp\left(-z^2/2\right)/\sqrt{2\pi}$ is the PDF for the standardized normal distribution, $\Gamma(m) = \int_0^\infty x^{m-1}e^{-x}dx$ is the gamma function, $\phi_{\text{logis}}(z) = e^z(1+e^z)^{-2}$ is the PDF of a standardized logistic distribution.

Family	Probability Density Function ($r \geq 0$ unless specified)	Parameter interpretation
Rayleigh (RA)	$f(r;\sigma) = \frac{r}{\sigma^2}\exp\left(-\frac{r^2}{2\sigma^2}\right)$	$\sigma > 0$: scale
Normal (NM)	$f(r;\mu,\sigma) = \frac{1}{\sigma}\phi\left(\frac{r-\mu}{\sigma}\right)$,	μ: mean; $\sigma > 0$: standard deviation
Lognormal (LM)	$f(r;\mu,\sigma) = \frac{1}{\sigma r}\phi\left(\frac{\ln(r)-\mu}{\sigma}\right)$, $r > 0$	μ: location $\sigma > 0$: scale
Nakagami (NA)	$f(r;m,\Omega) = \frac{2m^m r^{2m-1}}{\Gamma(m)\,\Omega^m}\exp\left(-\frac{m}{\Omega}r^2\right)$	$m \geq 0.5$: shape $\Omega > 0$: scale
Weibull (WE)	$f(r;\alpha,\beta) = \frac{\beta}{\alpha^\beta}r^{\beta-1}\exp\left[-\left(\frac{r}{\alpha}\right)^\beta\right]$	$\alpha > 0$: scale $\beta > 0$: shape
Loglogistic (LL)	$f(r;\mu,\sigma) = \frac{1}{\sigma r}\phi_{\text{logis}}\left(\frac{\ln(r)-\mu}{\sigma}\right)$, $r > 0$	μ: location $\sigma > 0$: scale
Gamma (GA)	$f(r;a,b) = \frac{1}{b^a\Gamma(a)}r^{a-1}\exp\left(-\frac{r}{b}\right)$	$a > 0$: shape $b > 0$: scale
Generalized Extreme Value (GE)	$f(r;k,\mu,\sigma) = \frac{1}{\sigma}\exp\left[-\left(1+k\frac{(r-\mu)}{\sigma}\right)^{-\frac{1}{k}}\right]\left(1+k\frac{(r-\mu)}{\sigma}\right)^{-1-\frac{1}{k}}$ with $1+k\frac{(r-\mu)}{\sigma} > 0$	$k \neq 0$: shape μ: location $\sigma > 0$: scale
Generalized Gamma (GG)	$f(r;a,b,c) = \frac{cr^{ac-1}}{b^{ac}\Gamma(a)}\exp\left[-\left(\frac{r}{b}\right)^c\right]$	$a > 0$, $c > 0$: shape $b > 0$: scale

scatterer i, and N is the number of scatterers;R denotes the envelope of the signals received by the transducer. The amplitude, a_i, depends on the shape, size, and acoustical properties of each scatterer with respect to the surrounding medium. The phase, θ_i, depends on the position of each scatterer. Because a_i, θ_i, and N are unknown beforehand, they can be modeled, in general, as random variables. Therefore, the resultant envelope R of the signal backscattered from an ensemble of discrete scatterers is also a random quantity that can be described using probability density functions (PDFs). Although scattering in real tissue results from a continuous distribution of scattering sites throughout the tissue and not from discrete scatterers, this simplified model provides a convenient starting point for analysis. To determine which PDF best models the envelope of HFU data acquired from human LNs, we investigated nine exponential PDFs described in Table 3.1. Each PDF is described briefly.

Rayleigh (RA) distribution: On the basis of the central-limit theorem, the envelope data, R, can be modeled using a RA distribution for either a large number of randomly distributed scatterers (the phase, θ_i, is uniformly distributed from 0 to 2π) [67], or when the individual amplitudes a_i are themselves RA distributed [64]. The ratio of the mean of the RA distribution to its standard

deviation, i.e., its *SNR*, has a constant value of 1.91.

Normal (NM) distribution: According to the central-limit theorem, the NM distribution approximately models the sum of a large number of independent, identically distributed (i.i.d.) random quantities. The NM distribution was used to describe the intensity distribution of ultrasound images of prostate tissue [68]. It has recently been used to model the saturated 3D ultrasound data acquired from fetal tissue [63].

Lognormal (LM) distribution: The LM distribution is a common model for failures times. According to the central-limit theorem, the LM distribution can be used to model a random variable that arises from the product of a number of identically distributed independent positive random quantities [69]. In the context of ultrasound, the LM distribution has been used to model the speckle in hepatic images [56].

Nakagami (NA) distribution: The NA distribution was first proposed by Nakagami to describe the statistics of returned radar echoes [70]. The parameter m is constrained such that $m \geq 0.5$ [70]. The study by Yacoub [71] indicated that the magnitude of the incoherent sum of powers (as opposed to the instantaneous amplitude summation) of several RA signals can be modeled by the NA distribution. In the context of ultrasound, Shankar [67] proved that pre-Rayleigh ($SNR < 1.91$), Rayleigh ($SNR = 1.91$) and post-Rayleigh ($SNR > 1.91$) conditions could be modeled by the Nakagami distribution. Moreover, Shankar showed that the envelope of backscattered signals obtained from human breast was described well by this distribution and that its parameters could be used to classify breast masses [72]. The NA distribution includes the RA distribution for the special case when $m = 1$, and approximates the Rician distribution when $m > 1$.

Weibull (WE) distribution: The WE distribution has been used to model radar clutter signals [73]. The statistics of the envelope of high-frequency ultrasonic backscatter from human skin have been approximately described by this distribution [64]. Because the *SNR* monotonically increases with the shape parameter β, the WE distribution can be used to model pre-Rayleigh ($0 < \beta < 2$), Rayleigh ($\beta = 2$) and post-Rayleigh ($\beta > 2$) conditions. Note that, the WE distribution includes the exponential ($\beta = 1$) and RA ($\beta = 2$) distributions. Furthermore, if R has a WE distribution with parameters α and β, then $U = \ln(R)$ has an extreme value distribution with μ and σ parameters, where $\mu = \ln(\alpha)$, and $\sigma = \beta^{-1}$.

Loglogistic (LL) distribution: The LL distribution is often used in survival analysis to model

events that experience an initial rate increase, followed by a rate decrease. The LL distribution is considered here because it has a shape that is similar to the shape of the LM distribution; however the LL distribution has heavier tails, i.e., the tails of the histogram at high and low values are heavier [69].

Gamma (GA) distribution: The sums of exponentially distributed random variables can be well modeled by the GA distribution. If parameter a is large, the GA distribution closely approximates a NM distribution when modeling positive real numbers. The GA distribution includes the exponential distribution when $b = 1$, and also includes the chi-squared distribution with n degrees of freedom when $a = n/2$ and $b = 2$. Moreover, if R has a NA distribution with parameters m and Ω, then R^2 has a GA distribution with a shape parameter m and a scale parameter Ω/m. Because the shape parameter a takes values in the range $0 < a < \infty$, using the GA distribution eliminates the constraint ($m \geq 0.5$) that is imposed when using the NA distribution. In the context of ultrasound, the GA distribution was shown to well describe the envelope of backscattered signals obtained from amniotic fluid and fetal tissues [63].

Generalized extreme value (GE) distribution: The GE distribution was developed within extreme value theory to combine the Gumbel ($k = 0$), Frechet ($k > 0$), and WE ($k < 0$) families; it also corresponds to the type I, type II and type III extreme value distributions [74]. The GE distribution is often used as an approximation to model the maxima of long finite sequences of random variables. We consider this distribution because the envelope of ultrasound echo-signal data presents local maxima.

Generalized gamma (GG) distribution: By adding a third parameter to the GA distribution, Stacy [75] introduced the GG distribution. Shankar [76] proposed the use of the GG distribution to model the envelope of ultrasonic signals backscattered from breast tissue. Subsequently, the GG distribution was demonstrated to describe the envelope of 2D HFU signals backscattered from human skin [64]. An interesting property of the GG distribution is its ability to model amplitude as well as intensity fluctuations (if R is GG distributed, R^2 and kR (where k is a constant) are also GG distributed). This distribution also includes the following distributions as special cases: RA ($c = 2, a = 1$), exponential ($c = 1, a = 1$), NA ($c = 2$), WE ($a = 1$), GA ($c = 1$), and LM ($a \to \infty$).

3.2.2 Probability-Density-Function Parameter Estimation

The parameters of each distribution describing the envelope data were estimated according to the following relations using the method of moments. This method derives parameters from the moments of the data and provides computational efficiency. For convenience, the M envelope samples $\{r_i\}_{i=1}^{M}$ in the region of interest were assumed to be i.i.d., and $\mathrm{AVG}(R) = M^{-1}\sum_{i=1}^{M} r_i$ denotes the sample mean of the envelope R.

RA distribution: The scale parameter σ of the RA distribution can be effectively estimated as $\hat{\sigma} = \sqrt{2/\pi}\,\mathrm{AVG}(R)$.

NM distribution: The mean and standard deviation parameters of the NM distribution can be estimated using $\hat{\mu} = \mathrm{AVG}(R)$, $\hat{\sigma} = \sqrt{\mathrm{AVG}(R^2) - (\mathrm{AVG}(R))^2}$.

LM distribution: The NM and LM distributions are closely related. If R is distributed lognormally with parameters μ and σ, then $U = \ln(R)$ is distributed normally with mean μ and standard deviation σ. Consequently, the location and scale parameters of the LM distribution can be efficiently estimated as $\hat{\mu} = \mathrm{AVG}(U)$, and $\hat{\sigma} = \sqrt{\mathrm{AVG}(U^2) - (\mathrm{AVG}(U))^2}$.

NA distribution: The method of moments can be used to obtain the two parameters of the NA distribution as follows

$$\hat{\Omega} = \mathrm{AVG}\left(R^2\right) \tag{3.1}$$

$$\hat{m} = \frac{\left(\mathrm{AVG}\left(R^2\right)\right)^2}{\mathrm{AVG}(R^4) - \left(\mathrm{AVG}(R^2)\right)^2}. \tag{3.2}$$

The estimation of the parameter m using (3.2) is computationally efficient. However, the constraint $(m \geq 0.5)$ was violated by this estimation on our data. Therefore, we used the m estimator devised by Greenwood and Durand [77] because it best approximates to the maximum-likelihood estimator as indicated by Zhang [78].

$$\hat{m} = \begin{cases} \frac{0.50008 + 0.16488y - 0.05442y^2}{y} & \text{, when} \quad 0 < y \leq 0.5772 \\ \frac{8.898919 + 9.05995y + 0.9775373y^2}{y\left(17.79728 + 11.96847y + y^2\right)} & \text{, when} \quad 0.5772 < y < 17, \end{cases} \tag{3.3}$$

where $y = \ln(\hat{\mu}_2/G)$, with a sample estimate of the k^{th} moment $\hat{\mu}_k = \mathrm{AVG}\left(R^k\right)$, and $G = \left(\prod_{i=1}^{M} r_i^2\right)^{1/M}$.

WE distribution: There are no closed-form expressions for estimating the β parameter of the WE distribution. Using the method of moments [79], the parameter $\hat{\beta}$ can be estimated by solving the following implicit equation:

$$\frac{\Gamma\left(1+2\hat{\beta}^{-1}\right)}{\left[\Gamma\left(1+\hat{\beta}^{-1}\right)\right]^2} = \frac{\mathrm{AVG}\left(R^2\right)}{\left[\mathrm{AVG}\left(R\right)\right]^2}. \tag{3.4}$$

A unique solution of $\hat{\beta}$ exists because the left hand side (LHS) of (3.4) is a monotonic function of $\hat{\beta}$. A look-up table with precomputed values of the LHS as a function of finely spaced $\hat{\beta}$ (estimation accuracy of 0.0001 for $0.1 \leq \hat{\beta} \leq 5.0$) was used to obtain $\hat{\beta}$. After obtaining $\hat{\beta}$, $\hat{\alpha}$ was estimated from the equation, $\hat{\alpha} = \mathrm{AVG}\left(R\right)/\Gamma\left(1+\hat{\beta}^{-1}\right)$.

LL distribution: The LL distribution is closely related to the logistic distribution. If R is distributed loglogistically with parameters μ and σ, then $U = \ln\left(R\right)$ is distributed logistically with parameters μ and σ. Consequently, the parameters of the LL distribution are estimated using the method of moments as, $\hat{\mu} = \mathrm{AVG}\left(U\right)$, and $\hat{\sigma} = \sqrt{3}\,\pi^{-1}\sqrt{\mathrm{AVG}\left(U^2\right) - \left(\mathrm{AVG}\left(U\right)\right)^2}$.

GA distribution: Using the method of moments, the parameters of the GA distribution can be efficiently estimated as follows:

$$\hat{a} = \frac{\left(\mathrm{AVG}\left(R\right)\right)^2}{\left[\mathrm{AVG}\left(R^2\right) - \left(\mathrm{AVG}\left(R\right)\right)^2\right]}, \tag{3.5}$$

$$\hat{b} = \frac{\left[\mathrm{AVG}\left(R^2\right) - \left(\mathrm{AVG}\left(R\right)\right)^2\right]}{\mathrm{AVG}\left(R\right)}. \tag{3.6}$$

.

GE distribution: There is no closed-form solution for the parameter estimation of the GE distribution. Therefore, its three parameters were estimated using a maximum likelihood algorithm [74].

GG distribution: The three parameters of the GG distribution can be estimated using the moment of the logarithm of data [80]:

$$\frac{\Psi^{(2)}\left(\hat{a}\right)}{\left[\Psi^{(1)}\left(\hat{a}\right)\right]^{1.5}} = -\left|\frac{\mathrm{AVG}\left[\left(U-\mathrm{AVG}\left(U\right)\right)^3\right]}{\left\{\mathrm{AVG}\left[\left(U-\mathrm{AVG}\left(U\right)\right)^2\right]\right\}^{1.5}}\right| \tag{3.7}$$

$$\hat{c} = \sqrt{\frac{\Psi^{(1)}(\hat{a})}{\mathrm{AVG}\left[(U - \mathrm{AVG}(U))^2\right]}} \tag{3.8}$$

$$\hat{b} = \mathrm{AVG}(R)\frac{\Gamma(\hat{a})}{\Gamma(\hat{a} + \hat{c}^{-1})}, \tag{3.9}$$

where $U = \ln(R)$, and $\Psi^{(n)}(a) = d^{n+1}\left[\ln\Gamma(a)\right]/da^{n+1}$ is the polygamma function. The LHS of (3.7) is a monotonic function of $\hat{a}$. The solution of (3.7) was found by using a look-up table with precomputed values of the LHS as a function of finely spaced $\hat{a}$ (estimation accuracy of 0.001 for $0.1 \leq \hat{a} \leq 50.0$). Once $\hat{a}$ was obtained, the parameters $\hat{c}$ and $\hat{b}$ were estimated using (3.8) and (3.9), respectively.

3.2.3 Goodness-of-Fit Evaluation

To evaluate quantitatively the goodness of fit of each candidate distribution to the experimental envelope distribution, the Kolmogorov Smirnov (KS) metric [81] was used. The KS metric is the maximum absolute difference between the theoretical cumulative distribution function (CDF) $(F(x))$ and the experimental envelope CDF $(G(x))$; it is given by $M_{KS}(F,G) = \max|F(x) - G(x)|$. Smaller values of the KS metric indicate a better fit of the candidate distribution to the experimental distribution.

3.3 Characterization of Experimentally Acquired Ultrasound Data

3.3.1 Extraction of 3D Regions-of-Interest (ROIs)

The extraction of the ROIs plays a crucial role in statistical analysis. The size of each ROI must be large enough to contain a sufficient number of resolution cells so that each ROI contains an adequately large number of independently and identically distributed envelope voxels to maintain the stability of parameter estimation. On the other hand, the ROI must be small enough to provide acceptable spatial resolution, and to avoid getting signals affected by very different attenuation

and diffraction effects. To mitigate potential bias related to LN size, a maximum of ten non-overlapping, randomly-located ROIs at a fixed depth (distance from the transducer) were selected for LNP, PNF and NS. Any ROIs that were not fully included in depths between 10.85 mm to 13.55 mm were not processed because they were considered to be too distant from the focal zone of the transducer.

3.3.1.1 Lymph Node Parenchyma and Normal Saline

For statistical analysis of the LNP and NS, non-overlapping, randomly-located cylindrical ROIs with a 0.7 mm length and diameter were extracted from the envelope data. The number of independent resolution cells for each 3D ROI was $\left[\pi\,(700/2)^2 \times 700\right] / \left[\pi\,(116/2)^2 \times 85\right] \sim 296$, because the predicted axial and lateral resolutions of the imaging system were 85 μm and 116 μm, respectively. The centers of the ROIs were located at depths of 11.2 mm, 12.2 mm (focal distance), 13.2 mm. Figure 3.1(a) and 3.1(b) present the z-x and y-x cross-sectional planes, respectively, to illustrate the ROI dimensions in the LNP.

3.3.1.2 Perinodal Fat

Because the layer of PNF surrounding the LNP is thin and varies in extent, use of cylindrical ROIs within the PNF region of each LN is not practical. Consequently, ROIs were extracted from the PNF layer as illustrated in Figs. 3.1(c) and 3.1(d). For each LN, the ROIs in the PNF layer were placed so that the number, N, of voxels within each ROI was equal to the number within the ROIs of the LNP or NS. First, a 3D PNF-mask section with a depth range of 0.7 mm and central depth of 11.2, 12.2 or 13.2 mm, respectively, was prepared using the manually segmented PNF label (Fig. 3.1(c)). Second, within the x-y plane, triangular sections were delimited so that the apex was at the center of the LN. The angle φ of each 3D triangular section was adjusted so that the number of PNF-mask voxels contained in a 3D triangular section (with a slice-thickness of 0.7 mm) equaled to N. Finally, the voxels within the PNF (as delimited by the section thickness and the triangular sections) were treated as an independent ROI for statistical analysis.

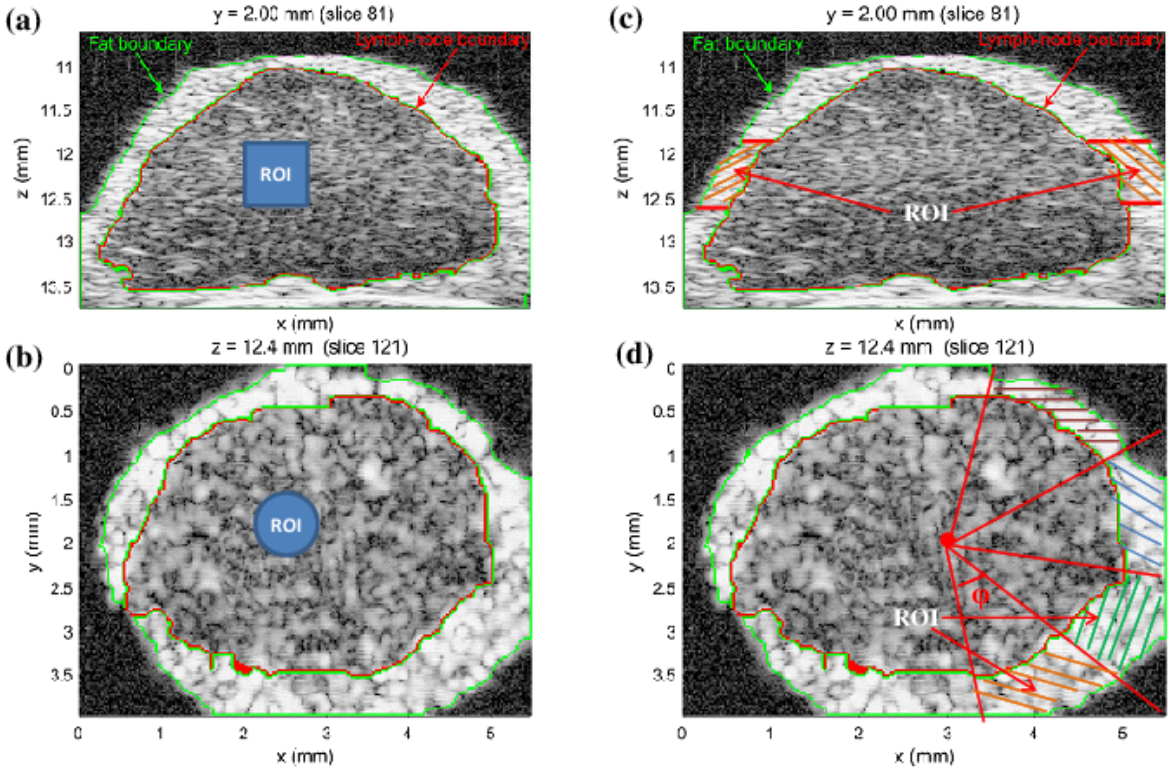

Figure 3.1: Illustration of the dimensions and positioning of a cylindrical ROI (solid blue region) in the LNP in the x-z plane (a) and the x-y plane (b). Similar positioning and ROI size was used to select ROIs in the NS. The division of the PNF layer into angular sections is illustrated by the cross-hatched regions in the x-z plane (c) and the x-y plane (d).

3.3.2 Initial Characterization of the Distributions

A database of 99 LNs dissected from colorectal-cancer patients was used to study the statistics of data at the focal depth (12.2 mm from the transducer). Eighteen nodes were entirely cancerous and 81 nodes were entirely devoid of cancer. Thirty-six LNs including 12 cancerous and 24 non-cancerous specimens were selected from the database to examine the statistics of LN data at, before and after the focal distance. These 36 LNs were selected because the semi-automatic segmentation technique [6] provided accurate segmentation throughout the entire LN (not only for regions at the focal distance). The number of ROIs for the LNP, PNF and NS media at the focal distance of the 99 LNs were 967, 956 and 468, respectively, since some small LNs provided fewer than 10 ROIs.

To facilitate comparing distributions, the vertical axes of all the box plots representing the KS metrics are presented on a log scale. For each box, the central mark is the median, the edges of the box are the 25^{th} and 75^{th} percentiles, the whiskers extend to the most extreme data points that are not considered outliers, and outliers are plotted individually. Points are drawn as outliers if they

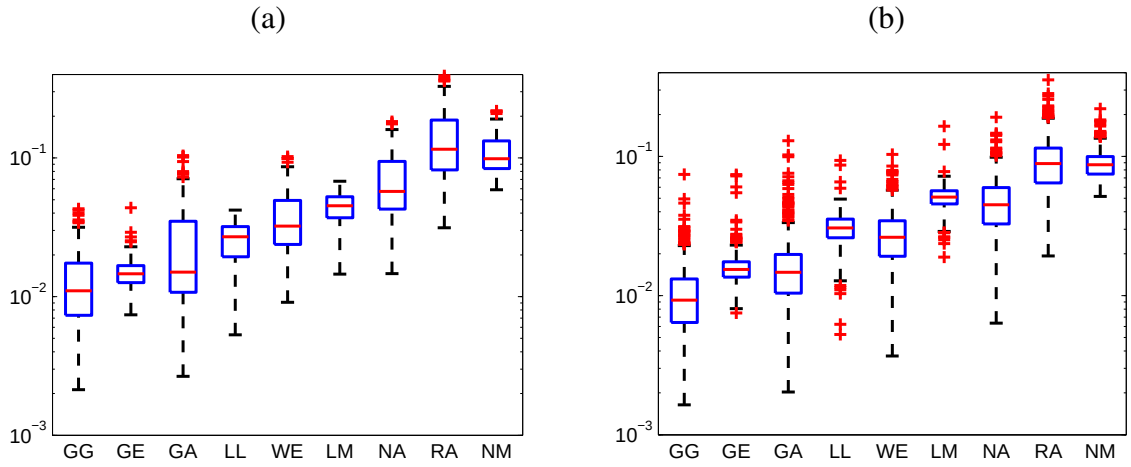

Figure 3.2: KS metrics for comparison of the goodness of fits for the different distributions describing the data from LNP ROIs centered at the focal distance. Eighteen cancerous LNs (a), and 81 non-cancerous LNs (b).

are larger than $q_3 + 1.5(q_3 - q_1)$ or smaller than $q_3 - 1.5(q_3 - q_1)$, where q_1 and q_3 are the 25^{th} and 75^{th} percentiles, respectively.

3.3.2.1 Models Describing the Statistics of Envelope Data of Lymph Node Parenchyma, Perinodal Fat and Normal Saline

The GG distribution best modeled the statistics for 66.4%, 65.2% and 61.1% of the ROIs of LNP, PNF and NS centered at the focal distance, respectively. The GG distribution also provided the lowest average values of the KS metric for the 967 LNP, 956 PNF and 468 NS ROIs. Figure 3.2 shows box plots of the KS metrics for the data from LNP ROIs of the 18 cancerous LNs and the 81 non-cancerous LNs. The plots illustrate how the GG distribution best fits the experimental envelope distribution of both cancerous and non-cancerous LNs. The GG distribution provides the lowest median values of the KS metrics for cancerous LNs (0.011) and non-cancerous LNs (0.009). Therefore, the GG distribution outperforms all the 8 remaining distributions (GE, GA, LL, WE, LM, NA, RA, NM) in fitting the envelope distributions from the three different media.

To investigate which distributions other than the GG distribution best describe the statistics of HFU envelope data acquired in cancerous and non-cancerous LNs at the focal distance, the percentage of ROIs best modeled by the remaining 8 distributions (excluding the GG distribution) was evaluated based on the KS metric. Results are summarized in Fig. 3.3. As shown in Fig. 3.3(a), the GA and GE distributions best model the statistics for 45.6% and 40.9%, respectively, of the cancerous

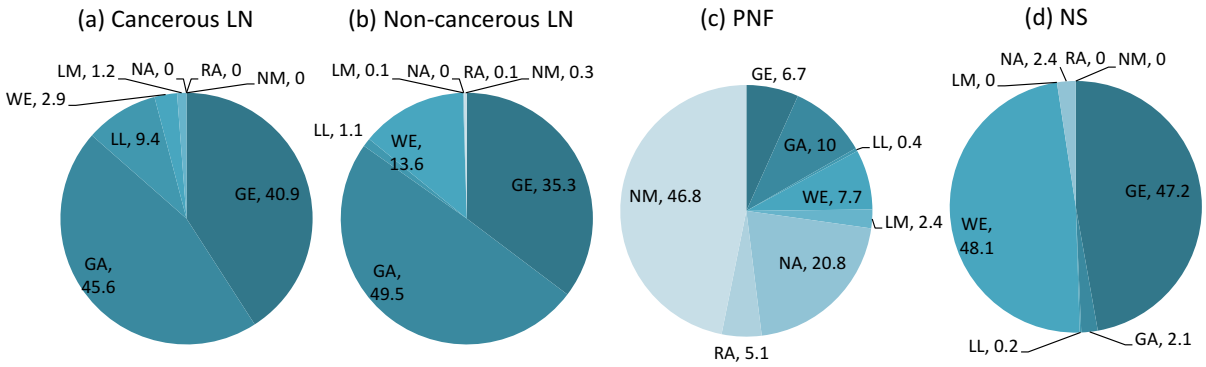

Figure 3.3: Percentages of ROIs from each medium that were best modeled by each of the eight distributions (excluding GG) as assessed using the KS metric. All ROIs were centered at the focal distance.

LNP ROIs. Thus they have approximately the same fitting performance and outperform all the remaining six distributions. Among the 81 non-cancerous LNs, the GA distribution best models the statistics for 49.5% of ROIs, followed by the GE distribution with 35.3%, as illustrated in Fig. 3.3(b). Consequently, the GA distribution fits most of the experimental envelope distribution of non-cancerous LNs better than the GE distribution does, as illustrated in Fig. 3.3(b).

Figure 3.4 presents the KS metrics for LNP ROIs centered at depths of 11.2 mm, 12.2 mm and 13.2 mm, respectively, for the 12 cancerous LNs and 24 non-cancerous LNs. The GG distribution best describes the statistics of ROIs at each depth, followed by the GA and GE distributions. Among the 12 cancerous LNs, the GE distribution fits the experimental envelope distribution slightly better than the GA distribution as shown in Figs. 3.4(a), 3.4(b), and 3.4(c). Furthermore, the distribution of the KS metrics of the GA distribution for cancerous LNs is broader than that for the non-cancerous LNs. However, the GA distribution is likely to describe the statistics of ROIs of non-cancerous LNs marginally better than the GE distribution as indicated in Figs. 3.4(d), 3.4(e), and 3.4(f).

Regarding the statistics of the envelope of the HFU data acquired in the PNF layer at the focal distance, Fig. 3.5(a) presents a box plot of the KS metrics for PNF ROIs centered at the focal distance of the 99 LNs. The GG distribution again shows the best fit by providing lowest KS metrics. The median of KS metrics of the GG distribution for PNF is 0.034 which is much higher than that for the LNP. The data summarized in Fig. 3.5(c) show that the NM distribution outperforms the other 7 distributions (excluding the GG distribution) by best describing the statistics of 46.8% of the PNF ROIs. Nevertheless, the distribution of the KS metrics of the NM, WE, NA distributions are

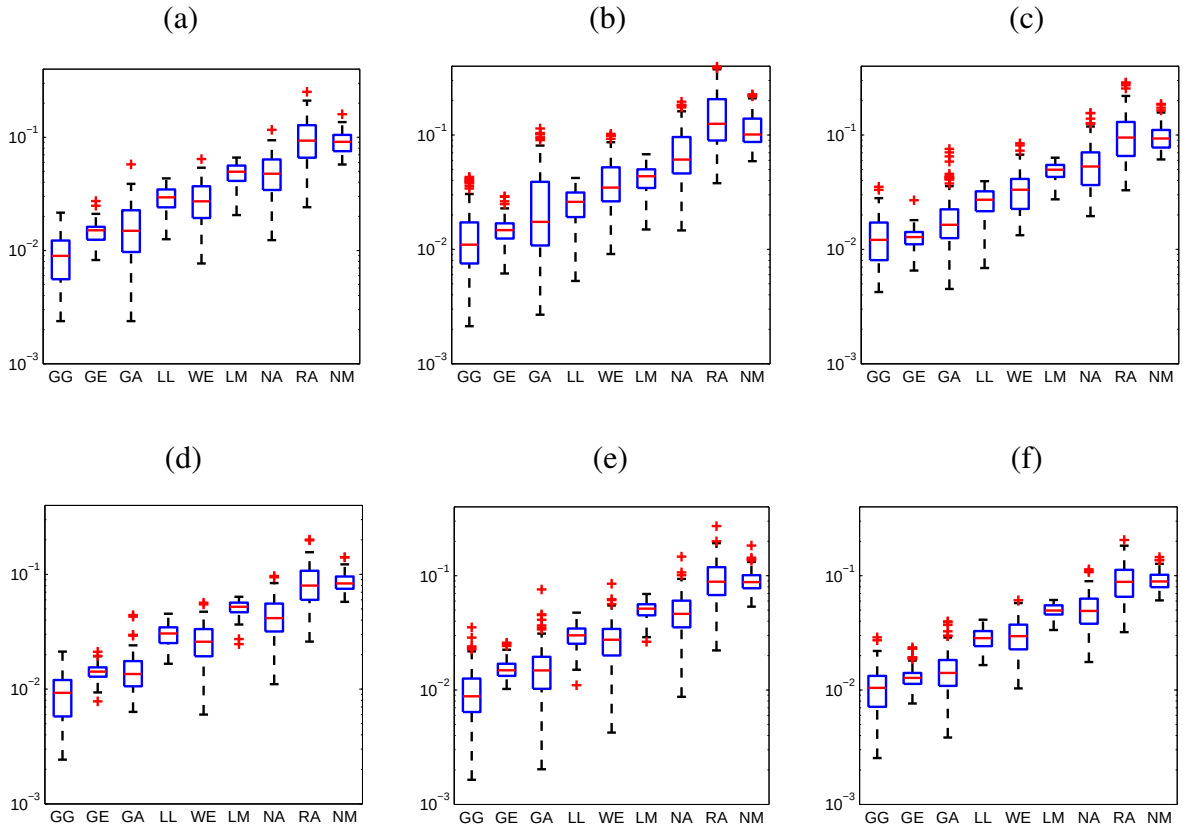

Figure 3.4: KS metrics for LNP ROIs of 12 cancerous LNs (a-c) and 24 non-cancerous LNs (d-f). The ROIs are centered at different depths: (a, d) 11.2 mm; (b, e) 12.2 mm; (c, f) 13.2 mm.

relatively similar as presented in Fig. 3.5(a). The WE distribution is superior to the NM and NA distributions because it has the lowest KS-metric median. The KS metrics for PNF ROIs centered at different depths, 11.2 mm, 12.2 mm and 13.2 mm are shown in Fig. 3.6. While the GG distribution always outperforms the other distributions, the NM distribution is fairly good at the focal distance, that is when the 75^{th} percentiles of the KS metrics of the GA distribution are the worst of the three 75^{th} GA percentiles. Away from the focal distance, apart from the GG distribution, the WE, GA and GE distributions provide reasonable alternatives as shown in Figs. 3.6(a) and 3.6(c).

The statistics of the envelope data obtained from the NS at the focal distance are best modeled by the WE and GE distributions (when the GG is excluded) as 48.1% and 47.2% of the NS ROIs, respectively, as shown in Fig. 3.3(d). The NA and GA distributions best describe the statistics of 2.4% and 2.1% of the ROIs. The same result is illustrated in Fig. 3.5(b), whereas the GG distribution obtains the best fit with the lowest median value of the KS metric (0.012), followed by the WE and GE distributions. To examine the envelope statistics for HFU data in NS at different depths, the KS metrics for the NS ROIs centered at the depths of 11.2 mm, 12.2 mm, and 13.2 mm,

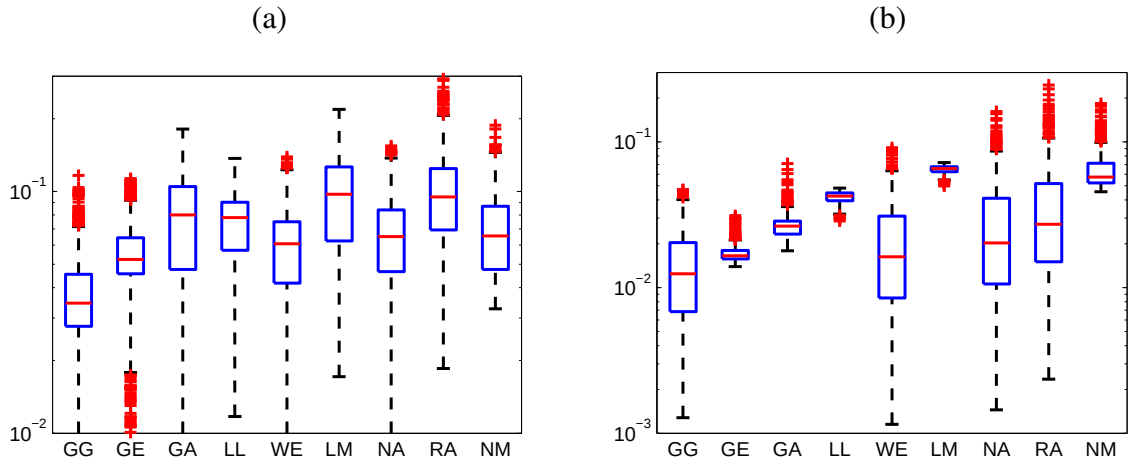

Figure 3.5: KS metrics for PNF (a) and NS (b) ROIs centered at the focal distance of the 99 LNs.

Table 3.2: Distributions best describing the envelope of HFU data as assessed using the KS metric. From left to right the distributions are listed in the order of descending accuracy.

Medium	Best-fit distributions
LNP	GG > GA> GE > WE
PNF	GG > WE > GA/NA > GE
NS	GG > WE > GE > NA/GA/RA

respectively, are shown Figs. 3.6(d), 3.6(e) and 3.6(f). In the descending order of fitting accuracy, the GG, WE, GE, NA, GA, and RA distributions best model the statistics of the NS data. This is true at all the depths considered. Ideally, the NS region contains no scatterers so statistics are anticipated to be those of the noise. Table 3.2 summarizes the distributions that best model the three media encountered in LN data ranked according to their relative accuracy as assessed using the KS metric.

Figure 3.7 shows the experimental PDFs for two representative ROIs corresponding to LNP and NS media, as well as their best estimated PDFs and the associated KS metrics. The GG and GA distributions fit the experimental envelope of the LNP and NS very well in both tails as illustrated in Fig. 3.7(a) and 3.7(b).

3.3.2.2 Parameter Examination

The *SNR* of the envelope of all LNP ROIs are less than 1.91 ($SNR = 1.50 \pm 0.16$). This result indicates that the PDF of the LNP envelope satisfies the pre-Rayleigh condition.

Because the GG distribution best models the envelope data of the LNP, PNF and NS, an examina-

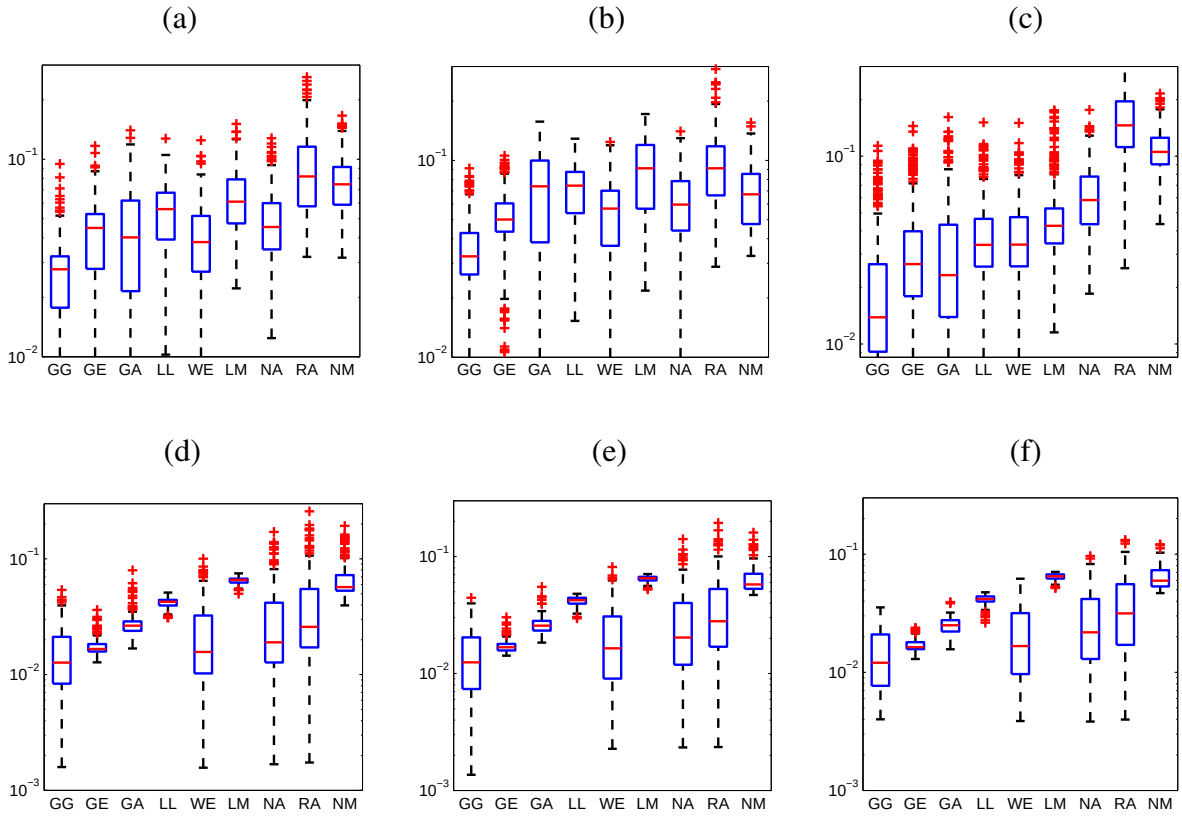

Figure 3.6: KS metrics for PNF ROIs (a-c) and NS ROIs (d-f) of the 36 LNs. The ROIs are centered at different depths: (a, d) 11.2 mm; (b, e) 12.2 mm; (c, f) 13.2 mm.

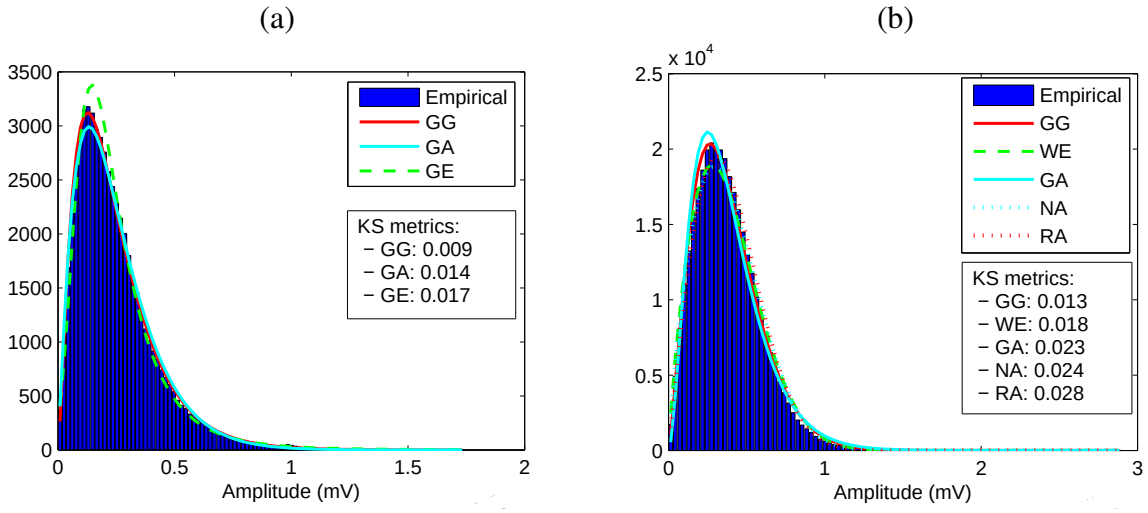

Figure 3.7: Experimental envelope PDF from representative LNP ROI (a) and NS ROI (b). Fits and associated KS metrics are shown for the best-fitting distributions.

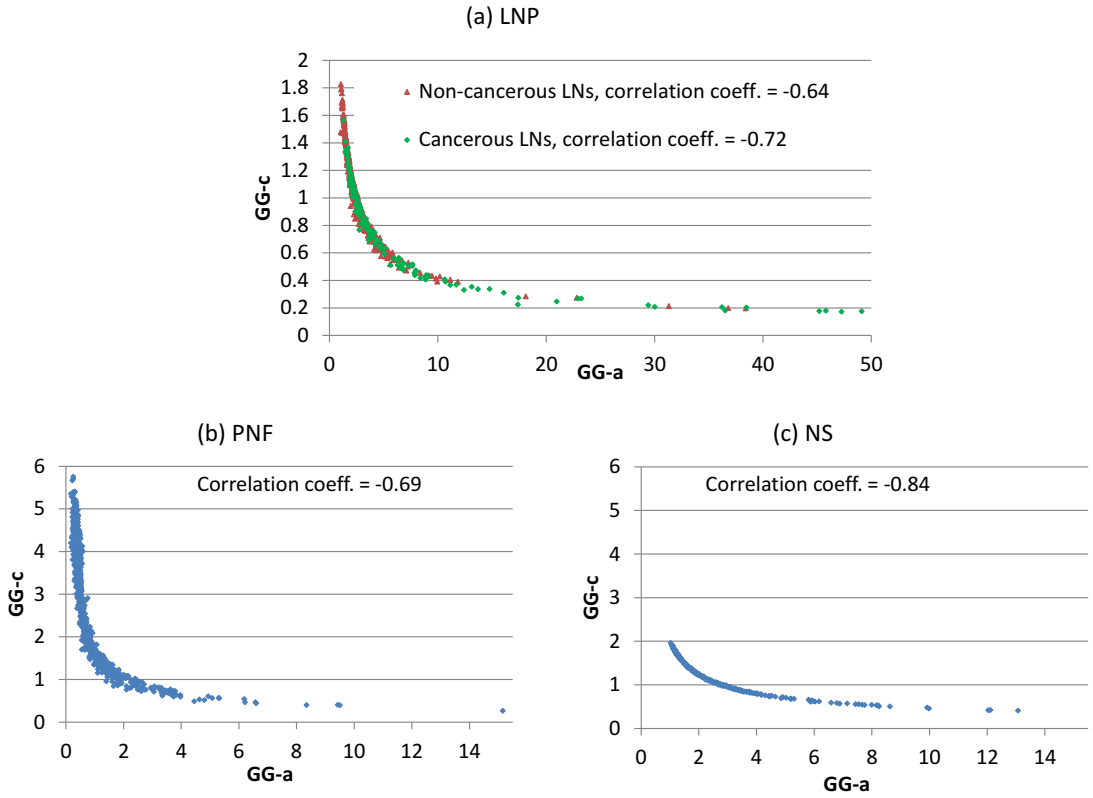

Figure 3.8: The relation between two shape parameters (GG-a, GG-c) of the GG distribution for different media. The correlation coefficients between GG-a and GG-c are also indicated.

tion of its parameters is worthwhile. As presented in Sect. 3.2, the GG distribution has a single scale parameter (GG-b) and two shape parameters (GG-a, GG-c). GG-b was not included in the study because it strongly depends on attenuation and examined depth. Depending on the values of the two shape parameters, the GG distribution may include RA $(c = 2, a = 1)$, exponential $(c = 1, a = 1)$, NA $(c = 2)$, WE $(a = 1)$, GA $(c = 1)$, and LM $(a \to \infty)$ distributions. Figure 3.8 shows the relationship between the two shape parameters of the GG distribution for the three media. ROIs at the focal zone of 18 cancerous LNs and 81 non-cancerous LNs were considered. Figure 3.8 indicates high correlations between the two shape parameters for the three media. As GG-a increases, GG-c decreases considerably. As shown in Fig. 3.8(a), GG-c never reaches the value of 2; this means that among the family of the GG distribution, the RA and NA distributions do not model the envelope data of LN parenchyma well, as reported in the previous subsection. Fig. 3.8(a) also shows a large overlap between the two shape parameters of cancerous LN ROIs and non-cancerous LN ROIs except when the GG-a parameter is greater than approximately 10. Therefore, using the two shape parameters to characterize between cancerous and non-cancerous LN ROIs can be expected to be ineffective. Nevertheless, Fig. 3.8 illustrates that the ranges of

values of the two shape parameters are different from one media to another but those ranges do overlap considerably.

3.3.2.3 Poor Modeling for Saturated Perinodal Fat Data

Although, among all the other distributions, the GG and WE distributions best model the statistics of PNF, their fitting accuracy is rather low as shown by the fact that the KS metric values are higher for PNF relative to like-cases for LNP and NS. The reason for this poorer fitting can be understood upon examination of the complicated experimental data-envelope distribution typical for data from the PNF as shown in Fig. 3.9(b). This irregular distribution results from the saturation occurring during digitization. During the acquisition, US system settings were optimized to acquire high quality RF signals in the LNP. Because PNF surrounding the LNP has a higher echogenicity than the LNP, its RF signals digitized using the 8-bit A/D board were partly saturated. This is demonstrated in Fig. 3.9(a) which displays the histogram of RF data from a region of interest (ROI) of the PNF medium. As a result of signal saturation, the envelope distribution in PNF becomes artificially multimodal with spurious peaks originating from the saturation effects on the Hilbert transform (Fig. 3.9(b)). Furthermore, in the PNF, the correlation coefficients between the percentage of saturated voxels in the HFU data and the KS metrics of the GG, WE and GA distributions are 0.70, 0.79 and 0.95, respectively. In particular, the KS metric values increase significantly as the percentage of saturated voxels in the HFU data increases. Therefore, it is necessary to restore the RF saturated values, which occurred predominantly in the PNF medium, to their true values because a unimodal distribution cannot properly model the distribution of saturated envelope data from PNF.

3.4 Restoration of Saturated Data

3.4.1 Smoothing Spline Restoration

In order to recover the saturated values, a smoothing cubic spline function, g, [82, 83] was constructed for each 1D RF signal , s, along the sound propagation direction to closely approximate non-saturated samples, and, thus, to restore RF signals. Suppose that among the sequence of N sampled values $s(t_j)$ with $j \in \{1,\ldots,N\}$, N_J samples were not saturated and $N - N_J$ samples were

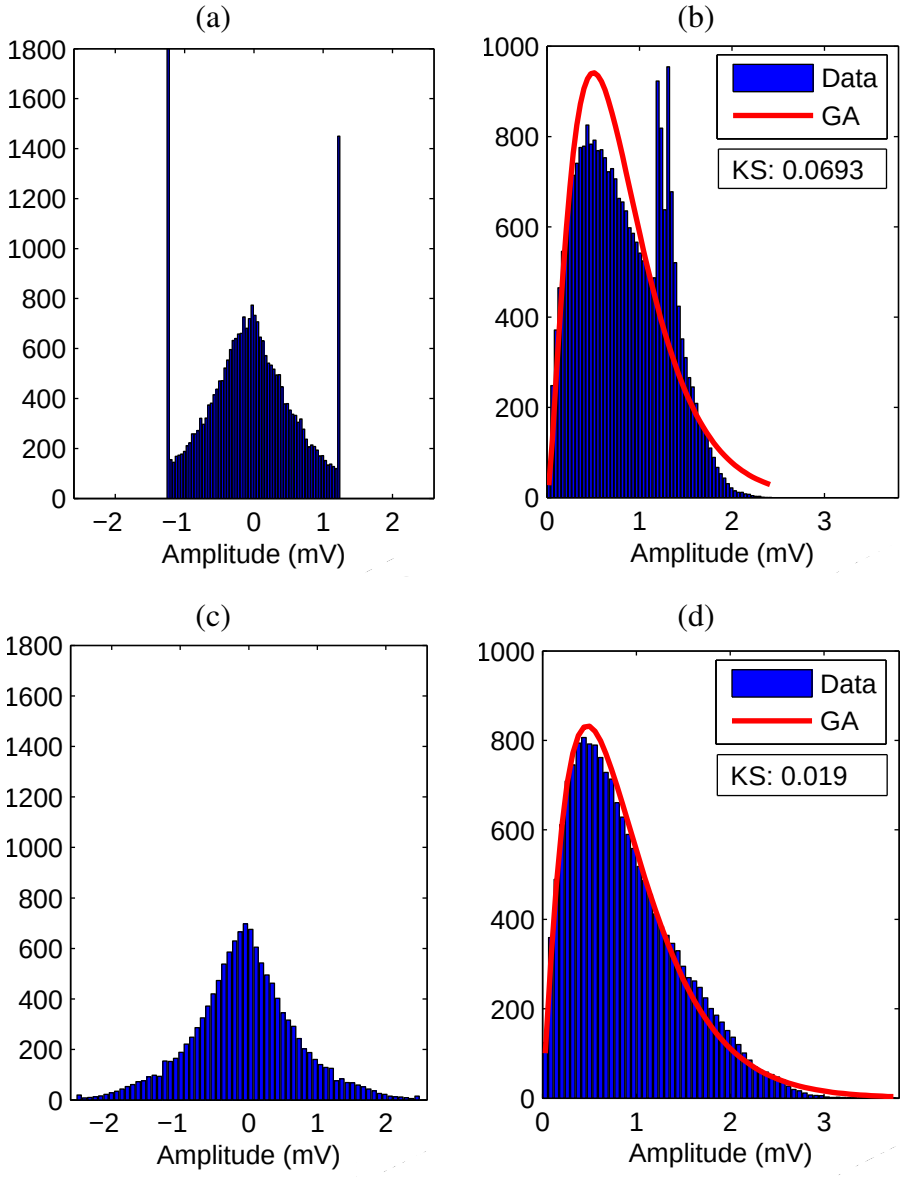

Figure 3.9: The effect of the pre-processing step on histograms describing the data from PNF. Histograms of envelope data from a ROI in the PNF medium for the original saturated RF data (a) and for the corresponding envelope data (b). After pre-processing with $\lambda = 0.9$, the histograms are (c) and (d) for the RF and envelope, respectively. The red curves designate the fit GA distributions for the envelope data before (b) and after (d) restoration of saturated RF samples.

saturated. By denoting J the subsequence of non-saturated samples and $\overline{J}$ the subsequence of saturated samples, each index $j \in \{1,\ldots,N\}$ belongs either to J or $\overline{J}$. On each interval delimited by two consecutive, non-saturated samples, the cubic spline function, g, agrees with a 4th order polynomial. By construction [82, 83], the smoothing spline function, g, has a continuous second derivative and was found by minimizing the penalized residual sum of squares (RSS)

$$RSS(g,\lambda) = \lambda \sum_{j\in J} (s(t_j) - g(t_j))^2 + (1-\lambda) \int_{-\infty}^{+\infty} |g''(t)|^2 dt, \tag{3.10}$$

where $\lambda \in (0,1]$ is a weighting and smoothing parameter. The first term is a loss function encouraging g to fit the non-saturated samples well. The second term penalizes the square of the second derivative of g. By decreasing the value of λ from 1 to 0, g gets smoother. As a result, when $\lambda = 1$, g interpolates the non-saturated samples, and when λ tends toward 0, g tends toward the linear least-squares fit of the non-saturated samples.

By changing the smoothing parameter, λ, and observing the KS metrics obtained in the envelope data of the PNF medium, the minimum of the KS metrics was obtained when the λ value was equal to 0.9. After applying restoration step, the envelope distribution in the PNF became a unimodal distribution as illustrated in Fig. 3.9(d) because the saturated RF values were recovered effectively as shown in Fig. 3.9(c).

3.4.2 Distributions Best Describing the Restored Data

Once the data were restored for saturation effects, the distributions best describing the data were once again examined. Fig. 3.10 presents the KS metrics estimated within ROIs located in PNF at the focal depth. Relative to fits obtained prior to data saturation, the KS metrics for the GG, GA and WE distributions were significantly decreased. Specifically, the p values estimated according to three Wilcoxon paired, signed-rank tests of KS metric values estimated from data before and after preprocessing for three distributions were less than 10^{-14}. The GG still provided the best fit for the PNF envelope distribution, whereas the GA and WE distributions achieved comparable fitting accuracy (Wilcoxon paired, signed-rank test, $p = 0.06$).

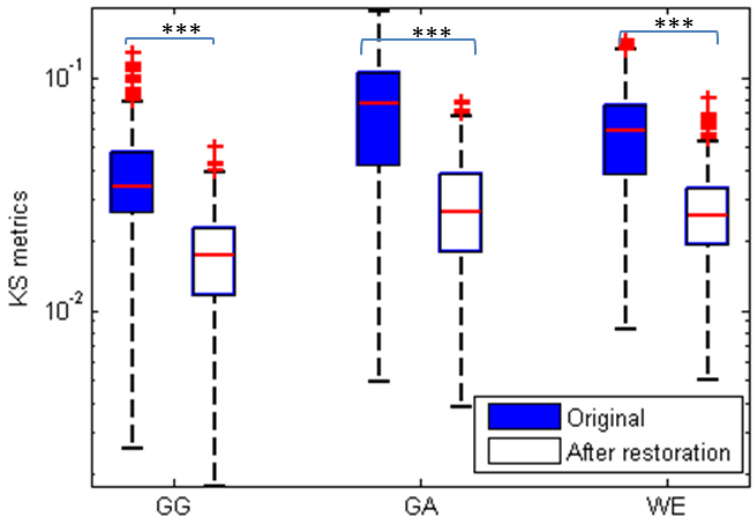

Figure 3.10: GG, GA and WE KS metric values of PNF envelope data from ROIs centered at the focal distance. The envelope was computed from the original RF signals or the RF signals after restoring the saturated samples. The asterisks *** indicate a p-value estimated according to the Wilcoxon paired, signed-rank test lower than 0.001.

3.5 Discussion and Conclusions

This work evaluates the statistics of 3D HFU envelope-signal data obtained from dissected human LNs. The results of the study indicate that the GG distribution best models the three different media (LNP, PNF and NS) interrogated during volumetric scanning because it produces the lowest values of the KS metric. The two shape parameters, GG-a and GG-c, of the GG distribution improve the fit of the heavier tails of the experimental PDFs. The GG distribution includes many distributions commonly used to characterize the speckle: gamma, Weibull, Nakagami, Rayleigh, exponential and lognormal. Therefore, it has all the advantages of these distributions. Although some differences exist between the two sets of shape parameters for the GG distribution, they present significant overlap between cancerous and non-cancerous LN ROIs. Thus, use of these shape parameters for characterization of LN types could be investigated further, but at present, such an approach seems to be of limited interest. The GG distribution has three parameters, and the high correlation between its two shape parameters (GG-a, GG-c) means that the envelope data could be effectively modeled by a 2-parameter distribution. Furthermore, the parameter estimation of the GG distribution is computationally expensive. Hence the use of the GG distribution in segmentation is not attractive. Alternatively, the two-parameter GA distribution also well described the envelope statistics for LNP data (as shown in Figs. 3.2–3.4). Its parameters can be estimated more efficiently than for the GG. Therefore, the GA distribution could provide a good option for

modeling the signal from LNP.

Closer examination of the physical interpretation of the distribution statistics can help understand why the Rayleigh distribution does not describe the data adequately. In ultrasound imaging, echo-signal envelope data statistics are described well by the Rayleigh distribution only when every resolution cell contains a large number of identical scatterers that are randomly and uniformly distributed. We applied our previously reported method [2] to estimate the two parameters (the effective number of scatterers, μ, per resolution cell and the ratio, k, of the coherent to diffuse signal) of the homodyned-K distribution for the 967 LNP ROIs centered at the focal distance (without compensation for attenuation). The average value of μ was 1.04 for cancerous LN, and 1.81 for non-cancerous LN. These values for the effective number of scatterers are too small (much smaller than 10 [44, 45]) to provide typical Rayleigh behavior and is consistent with the observed pre-Rayleigh behavior ($SNR = 1.50 \pm 0.16$). Furthermore, the average value of k was determined to be on the order of 0.57. This implies the existence of a non-negligible coherent signal, which is not a typical feature for data satisfying the Rayleigh conditions. The small number of effective scatterers per resolution cell may be partly driven by small resolution cell size (9.08×10^{-4} mm^3) obtained with the HFU imaging system. Although the tissue structures associated with the coherent signal have not been specifically identified, LNs are known to have a complex structure, and elements of this structure may contribute to producing speckle statistics that do not conform to the Rayleigh distribution. LN can be considered to be "kidney shaped" with an outer cortical layer surrounding an inner core of parenchyma and a central fatty hilum region. The cortex consists of numerous afferent lymph ductules and intertwined capillaries. These eventually converge toward small efferent ducts and blood vessels. Therefore, acoustic response from structures with very different scattering properties can be anticipated. Moreover, echoes from spatially extended structures such as the efferent vessels in the LNs may be strongly correlated (spatially coherent scattering). Clearly, to the extent that the different structures in the LN are scatterers, their sizes tend to change and increase toward the hilum. Furthermore, their orientations may depend on location within the node. Hence the scattering properties within a ROI may vary over the ROI and be dependent on the size and location of the ROI. This diversity of scatterers and their properties within the ROI may result in multiple distributions in the envelope statistics being expressed.

To describe the statistics of the envelope of the HFU in PNF, the WE distribution initially appeared to be the most appropriate as shown in Section 3.3.2.1. Although the GG and WE distributions

modeled the envelope data from PNF better than the remaining distributions, their fitting accuracy was not very good due to the complicated experimental PDF caused by saturation of the HFU echo signals from the PNF layers. Therefore, a restoration method based on smoothing-cubic spline was developed to restore saturated RF values which occurred mostly in the PNF medium. This step was necessary to recover a unimodal distribution. Once restored, the envelope data from the PNF was well-modeled by the GA distribution. To the best of our knowledge, constructing a smoothing-spline approximation to restore the saturated points in US data is novel. Previous work in the literature directs more attention to identifying statistical models that fit saturated [63] or left-censored US (linear or log-compressed envelope) data well [84] because the true values of saturated signals were considered to be lost. Note that the GE distribution modeled the statistics of the envelope data well for saturation-restored PNF as well as LNP. Nevertheless, the GE distribution is not a good candidate for incorporation in segmentation techniques because of the complicated expression for the PDF and the time-consuming estimation of parameters required to fit this expression.

For envelope data from regions within the NS, the WE provided best accuracy. The GA distribution performed next best for the characterization of statistics for data from NS. The NA and RA distributions also demonstrate an ability to model the statistics of the NS as shown in Fig. 3.7(c). In the NS, the KS metric is independent of the depth because the recorded signal in this medium were due to the noise from the acquisition system and not to backscattered echoes from scatterers.

In conclusion, based on these findings, the statistical distributions that appear to be the most promising to describe the envelope data adequately with minimal calculation time are the GA for LNP and PNF, and the WE or GA for the NS. For initial development of the segmentation method, the GA distribution can be selected to model the envelope data of the three media of LN envelope data because of its high fitting accuracy, its analytically less complex PDF expression, and its closed-form expression for parameter estimation. This provided a solid starting point for subsequent work to incorporate the statistics of the data from the three media into robust algorithms for segmentation of HFU data from human LNs.

Chapter 4

Local Region-based Gamma Distribution Fitting Segmentation Method[1]

4.1 Introduction and Literature

Segmentation is an important step in ultrasound (US) data analysis. Its main objective is to partition data into different regions in order to identify regions of interest for facilitating subsequent analyses or to allow the visualization of anatomical structures such as cardiac chambers, fetus, etc. Manual segmentation is subjective, tedious, and time-consuming, and automation of this task is highly desirable, especially for analysis of 3D data sets or dynamic image sequences. Nevertheless, automatic segmentation of US data faces many challenges, such as low contrast, lack of explicit boundaries, speckle and intensity inhomogeneities.

Speckle, depending on the density and the spatial distribution of sub-wavelength scattering structures, gives ultrasonic images their characteristic granular appearance. In Chapter 3, the gamma distribution has been found to be the best choice for statistical modeling of the envelope of the radio frequency (RF) echo signals acquired from human lymph nodes (LNs). Note that the gamma distribution has been previously introduced to model data distributions of blood and tissue in clinical B-mode cardiac images [58], and echo envelope distributions of blood and myocardial regions in echocardiographic images [59]. Throughout this chapter, we use the term "intensity" to refer to either the envelope of RF signals or the gray-scale level of clinical B-mode images. In US imaging, intensity inhomogeneities may be caused by variations in the tissue structure and/or the presence of several tissue types. Other, significant sources of intensity inhomogeneity with imaged depth arise

[1]This chapter is adapted from Thanh M. Bui, Alain Coron, Jonathan Mamou, Emi Saegusa-Beecroft, Eugene Yanagihara, Junji Machi, Alexandre Dizeux, S. Lori Bridal, and Ernest J. Feleppa, "Level-set segmentation of 2D and 3D ultrasound data using local gamma distribution fitting energy", IEEE International Symposium on Biomedical Imaging: From nano to macro (ISBI), New York, USA, pp. 1110-1113, 2015 [85]

due to acoustic focusing and attenuation. These depth-dependent effects are particularly important at high US frequencies ($>$ 15 MHz).

4.1.1 A Short Literature Review on Ultrasound Segmentation

Several segmentation methods have been developed for application to a number of clinical challenges and extensive reviews can be found in [41, 86, 87]. Various researchers have focused on employing Bayesian models to formulate a posterior energy function consisting of data likelihood (using parametric models of intensity distributions) and priors (e.g., shapes, spatial and/or temporal smoothness constraints). After estimating the parameters of the posterior energy function using stochastic or deterministic algorithms, segmentation results can be obtained. Xiao *et al.* [88] adapted the statistical method of [89] to segment B-mode clinical breast and cardiac US images in the presence of intensity inhomogeneity. The method employed maximum a *posteriori* (MAP) and Markov random field (MRF) methods to estimate the US image distortion field while labeling image regions based on the corrected intensity statistics. However, the US intensities were modeled by the Gaussian distribution. Boukerroui *et al.* [90] formulated a Bayesian MRF model to obtain an energy function consisting of a data fidelity term and a smoothness constraint to address the segmentation problem of 2D breast US data and echocardiographic sequences (2D + T). This model extended their previous work [91] by introducing a weighting function into the energy function to balance the local and global statistics in the image. The energy was then minimized using the iterated conditional mode algorithm. The conditional density distribution of the observed grey-scale intensity was also assumed to be Gaussian. Working on more-sophisticated statistical distributions, Destrempes *et al.* [92] proposed the use of a mixture of three Nakagami distributions to model three media, namely the intima-media layers, lumen and adventitia, to segment the intima-media thickness of carotid arteries based on the US B-mode image. The mixture parameters were estimated using an expectation maximization algorithm under the assumption that observations were independent. Then the MAP approach was employed to obtain the posterior distribution of the data likelihood acquired from the mixture of Nakagami and priors based on a geometric constraint, an anatomical prior and a temporal constraint. The final segmentation result was found by computing the posterior distribution iteratively using the exploration/selection algorithm. Depending on initialization, an optimal solution could be obtained. To segment lesions in multiple-tissue 2D and 3D HFU skin images acquired *in vivo*, a Bayesian algorithm combined with

a Markov chain Monte Carlo method was proposed by Pereyra *et al.* [93]. The likelihood was built using a heavy-tail generalized Rayleigh mixture to model multiple-tissue images, while the prior was based on the MRF to take into account the spatial correlation inherent in biological tissues. The posterior distribution of the Bayesian model was sampled using a hybrid Metropolis-within-Gibbs sampler to estimate the model parameters. More recently, Hansson *et al.* [84] formulated a Bayesian model for determining the position of the endocardium in clinical B-mode US cycles. The map describing the probability of pixels being classified as endocardium was constructed by using the Gibbs method to sample a posterior distribution. To obtain the posterior distribution, the data likelihood was formulated by using a gamma mixture model to handle artifacts resulting from left-censoring of the US clinical B-mode images; the spatial and temporal smoothness, and preferred shapes and position were considered as priors.

The iterative nested graph cut (NGC) method has also, very recently been proposed for segmentation of colorectal LN envelope data [94]. The method consisted of two steps: segmentation using NGC and distribution-parameter estimation. The NGC technique extended the graph cut framework to exploit the nested relationship of the three media, i.e., LNP is contained inside PNF and both media are within NS. The technique required the minimization of an energy function consisting of a length term (boundary smoothness constraint) and a data term. The data term was computed based on the use of the Gaussian distribution to model the intensity distribution of data within each media. In the distribution parameter estimation step, to account for the acoustic attenuation and focusing effects, a spline-based curve fitting was used to estimate the depth-dependent mean and variance parameters of the Gaussian distribution. Segmentation results were obtained by iterating between the two steps until convergence (about 5 iterations).

Deformable models including parametric [95–98] and geometric [99–102] models have proven to be powerful image-segmentation techniques. Geometric deformable models implemented using level-set methods have advantages over parametric models because of their ability (1) to handle topology changes automatically, (2) to remove the issue of contour parameterization and control-point regridding and (3) to facilitate implementation [103]. In contrast to the use of local edge information (gradient) to attract a contour toward the object boundaries as in edge-based methods, the statistical region-based methods evolve the contour by fitting statistical models to data within each of the separated regions. As a result, statistical region-based segmentation methods are far less sensitive to noise and initialization because fewer undesired local minima exist in their

cost functions [103]. By adapting the fundamental work of Chan and Vese [100] to segment fetal echography and echocardiography US images, Sarti *et al.* [101] proposed a region-based level-set method that employed the Rayleigh probability density function (PDF) to model the speckle statistics in US data. Segmentation was performed by minimizing an energy function formulated from Rayleigh PDFs of the gray levels of the images and a smoothness constraint. The method, however, assumed that data in each segmented region are homogeneous (i.e., that data statistics are spatially invariant). Furthermore, more-precise statistical distributions [55, 67, 104] than the Rayleigh distribution have been proposed to model the US envelope data. Integrating appropriate intensity distributions (e.g., exponential family [105, 106]) into the development of segmentation methods was demonstrated to improve segmentation accuracy when applied to noisy images. To segment the utero-fetal unit from 3D US data, Anquez *et al.* [63] proposed a region-based level-set method that used the MAP approach to formulate an energy function. The energy function is comprised of a smoothness constraint prior and a likelihood obtained by modeling data statistics with tissue-specific intensity distributions to separate the amniotic fluid (modeled by an exponential or Rayleigh distribution), from maternal and fetal tissues (modeled by a normal distribution). The gamma distribution was also introduced as a generic model that could be used for all tissue types. Because the data statistics are computed in a global way (i.e., using data from the whole inner or outer regions), the method can fail or provide inaccurate segmentation results when the regions are inhomogeneous. Therefore, Dahdouh *et al.* [107, 108] introduced an additional shape prior for the fetus envelope and a shape model of the fetus' back to improve the robustness of the segmentation method.

Alternatively, several techniques based on local statistics [85, 109–112] have been proposed to deal with the intensity inhomogeneity present in images. Lankton [110] proposed a framework that allows the localization of any region-based segmentation energy. In this framework, the optimal partition is found by allowing the contour to evolve towards a local minimum of the energy function as formulated by integrating data statistics that are computed locally in a circular region around each pixel of interest. By inserting three kinds of energies into the framework, and with an appropriate initialization, the method has been successfully applied to segmenting real-world and MRI images in the presence of inhomogeneities. Nevertheless, the computation load of this technique is more expensive than that of methods based on global statistics. Barbosa *et al.* [113] proposed an efficient framework for real-time segmentation of 3D, inhomogeneous, echocardio-

graphic data and computer tomography liver tumor images. By sacrificing topology flexibility, the framework uses B-spline explicit active surfaces to recover objects from 3D data. This enables a contour to evolve by using global and local region-based segmentation energies.

Li *et al.* [109] proposed a region-based, active-contour model to segment images with intensity inhomogeneity by introducing a kernel function to define a region-scalable fitting energy function. By integrating the weighted averages (means) of the image intensities in the window specified by a Gaussian kernel with a localization property, the model was able to segment images in the presence of intensity inhomogeneity. To segment images with strong noise or different textures, Wang *et al.* [111] extended Li's model by using Gaussian distributions with different means and variances to model the local intensity distributions (specified by the Gaussian's kernel). However, the assumption that local image intensities are described by Gaussian distributions does not account well for the range of intensity distributions encountered in US data where envelope and clinical B-mode data are more-appropriately modeled by the gamma distribution [55, 58, 59, 63].

4.1.2 Our Contribution

Inspired by Wang and Li's Gaussian-based model, we investigated a novel segmentation method and applied it to 2D and 3D US data. The method employs the gamma distribution to model local US intensities specified by the mollifying kernel. The gamma-distribution parameters are estimated efficiently using the method of moments. This method performs well in the presence of ultrasonic speckle and sources of regional intensity inhomogeneities. Furthermore, both 2- and 3-phase methods can be implemented. Segmentation performance was evaluated using simulated envelope data, 2D clinical B-mode images obtained from murine tumors, and 3D envelope data acquired from human lymph nodes (LNs).

4.2 Proposed Segmentation Method

4.2.1 Two-phase Level-set Formulation

Let Ω be a bounded open subset of $\mathbb{R}^N$, $N = \{2,3\}$, and let $I : \Omega \to \mathbb{R}$ denote a N-dimensional image to segment. We present a local region-based gamma distribution fitting (LRGDF) segmentation

method that takes into account the statistical properties of US data and deals with the intensity inhomogeneities. We first describe the 2-phase method and then extend it to 3 phases needed for segmentation of the LN data. To derive a contour (curve in 2D and surface in 3D) evolution equation for energy minimization, we employ the level-set method that represents the contour (boundary) implicitly by the zero level of a function $\phi : \Omega \to \mathbb{R}$. The sign of $\phi(\mathbf{x})$ defines two regions: Ω_1, where $\phi(\mathbf{x}) > 0$; and Ω_2, where $\phi(\mathbf{x}) < 0$. The boundary between Ω_1 and Ω_2 is implicitly defined as $\phi(\mathbf{x}) = 0$. We define the following energy function:

$$E(\phi) = \int_\Omega \int_\Omega K_\rho(\mathbf{x}-\mathbf{y}) \left[-\sum_{i=1}^{2} \lambda_i M_i(\phi(\mathbf{y})) \ln p_i(I(\mathbf{y}); \theta_i(\mathbf{x})) \right] d\mathbf{y} d\mathbf{x} + \mu \int_\Omega |\nabla H(\phi(\mathbf{x}))| \, d\mathbf{x}, \tag{4.1}$$

where $\mu, \lambda_i \in \mathbb{R}^+$ are weighting parameters; $M_1(\phi(\mathbf{y})) = H(\phi(\mathbf{y}))$, $M_2(\phi(\mathbf{y})) = 1 - H(\phi(\mathbf{y}))$ are membership functions corresponding to the two regions; H is the Heaviside function. The $p_i(.)$ is the probability density function (PDF) of the gamma distribution modeling the intensities in local regions. As presented in Chapter 3, the gamma PDF is expressed as $p(I;\theta) = \frac{1}{b^a \Gamma(a)} I^{a-1} \exp\left(-\frac{I}{b}\right)$, where $\theta = (a,b)$ are shape and scale parameters.

In the energy function (Eq. 4.1), the kernel, $K_\rho(\mathbf{x}-\mathbf{y})$, is used to specify the local region centered at $\mathbf{x}$. The kernel $K_\rho(u)$ is a nonnegative scalar function with the following properties [109]:

1. $K_\rho(u) = K_\rho(-u)$;
2. $K_\rho(u) > K_\rho(v)$ if $|u| < |v|$, and $\lim_{|u|\to\infty} K_\rho(u) = 0$;
3. $\int K_\rho(x)\, dx = 1$.

We employ the mollifying kernel expressed as $K_\rho(\mathbf{u}) = \frac{A}{\rho^2} \exp\left[-1 / \left(1 - \left| \frac{\mathbf{u}}{\rho} \right|^2 \right) \right]$, if $|\mathbf{u}| \le \rho$ and zero elsewhere, $\mathbf{u} \in \mathbb{R}^N$, $\rho > 0$ is a scale parameter; the constant $A > 0$ is selected so that $\int K_\rho(\mathbf{u})\, d\mathbf{u} = 1$. The kernel $K_\rho(\mathbf{u})$ has compact support $|\mathbf{u}| \le \rho$ (i.e., it is zero outside the compact set $|\mathbf{u}| \le \rho$).

Note that the energy function Eq. 4.1 in our work is different from the energy defined by Wang et al. [111]. In Eq. 4.1, $p_i(I;\theta)$ is the gamma PDF used to model the local intensity distribution instead of the Gaussian PDF. In addition, $K_\rho(\mathbf{x}-\mathbf{y})$ is the mollifying kernel which is different from Gaussian kernel used in [111]. The mollifying kernel has better localization property and has been demonstrated to handle intensity inhomogeneities slightly better than the Gaussian kernel [114].

The minimization of the energy function (4.1) corresponds to two minimization tasks: minimization of E with respect to θ_1 and θ_2 (with a fixed ϕ), and minimization of E with respect to ϕ (with fixed θ_1 and θ_2). The first minimization yields the maximum likelihood (ML) estimate of the PDF parameters within the local regions. Because the ML approach does not provide a closed form solution to estimate the two gamma distribution parameters, the method of moments [115] was employed to acquire the closed form without significantly affecting the estimation accuracy as $\hat{a}_i(\mathbf{x}) = \frac{\hat{m}_i(\mathbf{x})^2}{\hat{v}_i(\mathbf{x})}$, $\hat{b}_i(\mathbf{x}) = \frac{\hat{v}_i(\mathbf{x})}{\hat{m}_i(\mathbf{x})}$, $i = 1,2$, where $\hat{m}_i(\mathbf{x})$ and $\hat{v}_i(\mathbf{x})$ are computed as follows:

$$\begin{cases} \hat{m}_i(\mathbf{x}) = \frac{\int K_\rho(\mathbf{y}-\mathbf{x}) I(\mathbf{y}) M_i(\phi(\mathbf{y})) d\mathbf{y}}{\int K_\rho(\mathbf{y}-\mathbf{x}) M_i(\phi(\mathbf{y})) d\mathbf{y}}, \\ \hat{v}_i(\mathbf{x}) = \frac{\int K_\rho(\mathbf{y}-\mathbf{x}) I(\mathbf{y})^2 M_i(\phi(\mathbf{y})) d\mathbf{y}}{\int K_\rho(\mathbf{y}-\mathbf{x}) M_i(\phi(\mathbf{y})) d\mathbf{y}} - \hat{m}_i(\mathbf{x})^2. \end{cases} \tag{4.2}$$

The minimization of E with respect to ϕ is implemented using the standard gradient descent method by solving the evolution equation (see Appendix A for detailed derivation):

$$\frac{\partial \phi}{\partial t} = \delta(\phi(\mathbf{x})) \left[\lambda_1 e_1(\mathbf{x}) - \lambda_2 e_2(\mathbf{x}) + \mu \operatorname{div}\left(\frac{\nabla \phi(\mathbf{x})}{|\nabla \phi(\mathbf{x})|} \right) \right], \tag{4.3}$$

where

$$e_i(\mathbf{x}) = \int_\Omega K_\rho(\mathbf{y}-\mathbf{x}) \ln p_i\left(I(\mathbf{x}); \hat{\theta}_i(\mathbf{y})\right) d\mathbf{y}, \tag{4.4}$$

and δ is the Dirac function.

In (4.3), the term, $\delta(\phi(\mathbf{x}))(\lambda_1 e_1(\mathbf{x}) - \lambda_2 e_2(\mathbf{x}))$, plays the key role in the segmentation model, since it drives the contour toward object boundaries. The second term is used to maintain the regularity of the contour.

4.2.2 Multiphase Level-set Formulation for Lymph Node Segmentation

4.2.2.1 Energy Function and Evolution Equations

A multiphase approach is implemented to allow simultaneous segmentation of more than 2 objects [116, 117]. Two or more level set functions $\phi_1, \phi_2 \ldots \phi_k$ are used to make a definition of N membership functions M_i of regions Ω_i, $i = 1,2\cdots,N$, such that $M_i(\phi_1(\mathbf{y}), \phi_2(\mathbf{y}) \cdots \phi_k(\mathbf{y}))$ equals 1 where $\mathbf{y} \in \Omega_i$, and zero elsewhere. To segment 3 media (i.e., LN parenchyma (LNP), perinodal fat (PNF), and normal saline (NS)) in the LN envelope data acquired from dissected human LNs,

we use two level set functions ϕ_1 and ϕ_2 to define 3 membership functions, $M_1(\phi_1(\mathbf{y}),\phi_2(\mathbf{y})) = H(\phi_1(\mathbf{y}))H(\phi_2(\mathbf{y}))$, $M_2(\phi_1(\mathbf{y}),\phi_2(\mathbf{y})) = (1-H(\phi_1(\mathbf{y})))H(\phi_2(\mathbf{y}))$ and $M_3(\phi_1(\mathbf{y}),\phi_2(\mathbf{y})) = 1 - H(\phi_2(\mathbf{y}))$, corresponding to the three regions. The gamma distribution is used to model the envelope data in LNP, PNF and NS regions. The energy function $E(\phi_1,\phi_2,\theta_1,\theta_2,\theta_3)$ is expressed as:

$$E(\phi_1,\phi_2,\theta_1,\theta_2,\theta_3) = \int_\Omega \int_\Omega K_\rho(\mathbf{x}-\mathbf{y}) \left[-\sum_{i=1}^{3} \lambda_i M_i(\phi_1(\mathbf{y}),\phi_2(\mathbf{y})) \ln p_i(I(\mathbf{y}),\theta_i(\mathbf{x})) \right] d\mathbf{y}d\mathbf{x} + \sum_{k=1}^{2} \mu_k \int_\Omega |\nabla H(\phi_k(\mathbf{x}))|\, d\mathbf{x}. \tag{4.5}$$

The parameters are estimated as presented in Section 4.2.1 and the final segmentation result is found by solving the gradient flow equation as follows (detailed derivation is presented in Appendix A):

$$\begin{cases} \frac{\partial \phi_1}{\partial t} = \delta\phi_1(\mathbf{x}) \left[H(\phi_2(\mathbf{x}))(\lambda_1 e_1 - \lambda_2 e_2) + \mu_1 \mathrm{div}\left(\frac{\nabla\phi_1(\mathbf{x})}{|\nabla\phi_1(\mathbf{x})|} \right) \right], \\ \frac{\partial \phi_2}{\partial t} = \delta\phi_2(\mathbf{x}) \left[H(\phi_1(\mathbf{x}))(\lambda_1 e_1 - \lambda_2 e_2) + \lambda_2 e_2 - \lambda_3 e_3 + \mu_2 \mathrm{div}\left(\frac{\nabla\phi_2(\mathbf{x})}{|\nabla\phi_2(\mathbf{x})|} \right) \right], \end{cases} \tag{4.6}$$

where e_1, e_2 and e_3 are computed as in (4.4).

4.2.2.2 Numerical Implementation and Initialization

For numerical implementation, the Heaviside and Dirac delta functions were replaced by their smoothed versions, $H_\varepsilon(x)$ and $\delta_\varepsilon(x)$ [109] given by:

$$H_\varepsilon(x) = \frac{1}{2}\left[1 + \frac{2}{\pi} \arctan\left(\frac{x}{\varepsilon} \right) \right], \tag{4.7}$$

$$\delta_\varepsilon(x) = H_\varepsilon'(x) = \frac{1}{\pi}\left[\frac{\varepsilon}{\varepsilon^2 + x^2} \right]. \tag{4.8}$$

The estimation of the parameter of the gamma distribution and the computation of e_i, $i = 1,2,3$ were implemented using convolutions as follows:

$$e_i = \ln(I) K_\rho * (\hat{a}_i - 1) - I K_\rho * \left(1/\hat{b}_i\right) - K_\rho * \left(\hat{a}_i \ln \hat{b}_i + \ln\Gamma(\hat{a}_i) \right). \tag{4.9}$$

The convolution ($*$) was implemented efficiently using the fast Fourier transform. The optimal parameter sets for the two-phase and three-phase segmentation methods are $\lambda_1 = 1.0$, $\lambda_2 = 1.04$, $\mu = 1.5$, $\rho = 12$, and $\lambda_1 = 1.04$, $\lambda_2 = 1.0$, $\lambda_3 = 1.01$, $\mu_1 = 1.2$, $\mu_2 = 1.0$, $\rho = 0.4$ mm, respectively.

A signed distance function of an ellipsoid centered at the center of the LN data was used to initialize for ϕ_1. To initialize automatically for ϕ_2 identifying the NS region, an anisotropic filter [118] and the Otsu thresholding algorithm were employed. To preserve the regularity of the level set functions, they were reinitialized every two iterations by computing the signed distance function map to their corresponding zero level set [63].

4.3 Evaluation Data and Methods

Reliable segmentation of tumors in clinical B-mode images is a critical step for monitoring tumor vasculature during therapy. B-mode images were acquired with a Sequoia 512 (Siemens Medical Solutions, Mountain View, CA) using a 15L8w linear-array transducer with a bandwidth of 8–15 MHz and a dynamic range of 80 dB.

The 2D, 2-phase LRGDF method was evaluated using twelve B-mode images of murine tumors. The 3D, 3-phase LRGDF method was evaluated using the simulated data as described in Section 2.2 of Chapter 2 and a representative, experimentally acquired database of envelope data from 54 LNs (18 metastatic and 36 nonmetastatic LNs) from 38 colorectal-cancer patients. The success of the segmentation method was quantified using the Dice similarity coefficient (DSC) [119]:

$$\mathrm{DSC} = \frac{2\,|X \cap Y|}{|X| + |Y|}, \tag{4.10}$$

where X and Y are, respectively, the automatic segmentation result and the reference result (the ground truth data in case of the simulated data or the expert manual segmentation in case of the clinical LN envelope data and B-mode images of murine tumor). The value of DSC is always between 0 and 1, and a value of 1 indicates perfect agreement between the two results.

To further evaluate the LRGDF segmentation method, results of the 2-phase method on the twelve 2D clinical, B-mode images of murine tumor were compared with respect to those obtained by the method proposed by Wang and Li *et al.* [111], which used the Gaussian distribution to model local intensities specified by the Gaussian kernel. In addition, results obtained by the 3-phase LRGDF

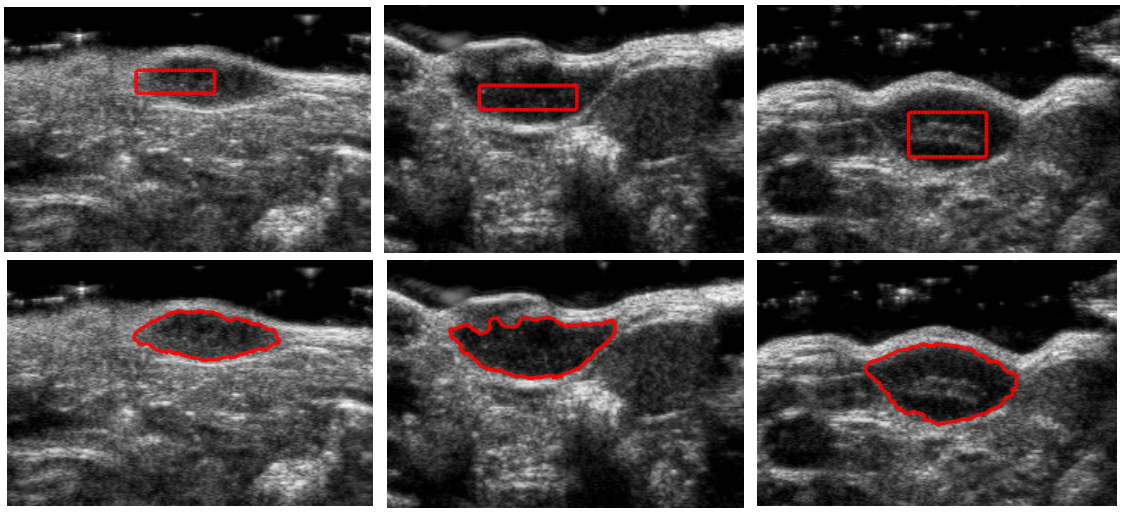

Figure 4.1: Segmentation results on B-mode images (80 dB dynamic range) acquired from murine tumors. Initializations (upper row) and their corresponding final results (bottom row). The DSCs of 3 images from left to right are 0.945, 0.882 and 0.936, respectively.

method on envelope data of 54 LNs were compared with those obtained by the $\text{Seg}_{\text{Gauss}}$ method of Wang and Li *et al.* adapted for 3D, 3-phase version.

4.4 Results

The 2-phase LRGDF method successfully demarcated tumors in the B-mode images by providing high DSC values. For the twelve B-mode images considered, the 2-phase method achieved a mean DSC value of 0.915 ± 0.026 compared to the DSC value obtained with the Wang and Li *et al.* method [111] of 0.896 ± 0.038. A few segmentation results are presented in Fig. 4.1.

On 20 3D simulated data sets, the average DSC values for LNP-like, PNF-like and NS-like regions obtained by the 3D, 3-phase LRGDF method were 0.975 ± 0.003, 0.919 ± 0.003 and 0.980 ± 0.001, respectively. To facilitate visual evaluation, Figure 4.2 presents segmentation results overlaid on the log compressed B-mode images (40 dB dynamic range). As shown in Fig. 4.2, the three regions are correctly delimited. Note that the signed distance functions of ellipsoids were used to initialize two level set functions.

The 3-phase LRGDF method was used to segment 3D envelope data for 54 LNs dissected from colorectal cancer patients. Fig. 4.3 shows a representative segmentation result overlaid on B-mode LN data. Automatic segmentation with the 3-phase and $\text{Seg}_{\text{Gauss}}$ methods were compared with manual segmentation by an expert using the DSC. The average DSC values for each method and

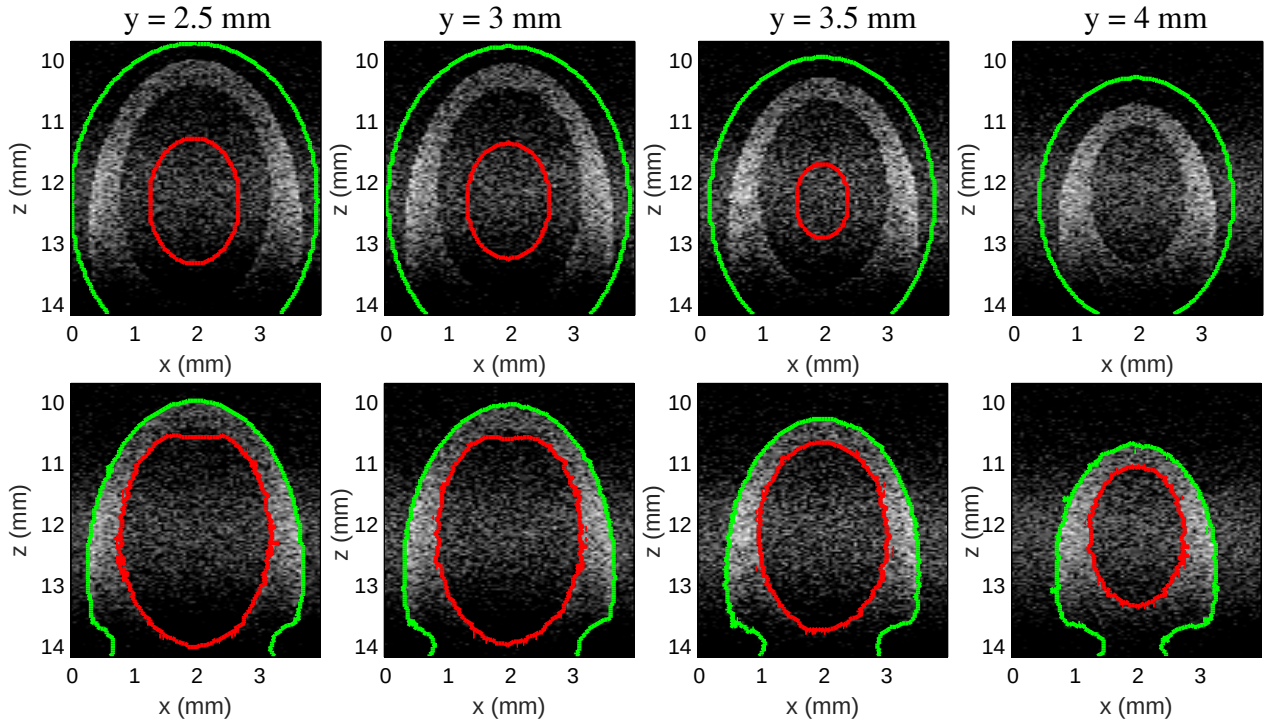

Figure 4.2: Slices extracted from 3D data from the simulated LN data set show initializations (top) and final segmentation boundaries (bottom) overlaid on corresponding B-mode display. Note that the red curve is the boundary between LNP and PNF; the green curve is the boundary between PNF and NS.

Table 4.1: The DSC (MEAN $\pm$ STD) of the LRGDF method and the $\text{Seg}_{\text{Gauss}}$ method over 54 LNs with the p-value estimated according to the Wilcoxon paired, signed-rank test.

Media	**LRGDF**	**$\text{Seg}_{\text{Gauss}}$**	**P-value**
LNP	0.920 ± 0.039	0.884 ± 0.082	$< 10^{-5}$
PNF	0.806 ± 0.110	0.767 ± 0.108	$< 10^{-5}$
NS	0.975 ± 0.009	0.968 ± 0.014	$< 10^{-9}$

segmented zone are summarized in Table 4.1. Table 4.1 indicates that the LRGDF method outperforms the $\text{Seg}_{\text{Gauss}}$ method. The Wilcoxon paired, signed-rank test indicated that the DSCs for the segmentation of the three media with the LRGDF method were statistically significantly better (p-value < 0.05) than those achieved with segmentation using the $\text{Seg}_{\text{Gauss}}$ method. Furthermore, the LRGDF method ran faster than the $\text{Seg}_{\text{Gauss}}$ method. Specifically, for the 54 LN data, the average execution time required to converge to the final result was 34.9 ± 20.3 and 38.2 ± 23.9 min for the LRGDF and the $\text{Seg}_{\text{Gauss}}$ methods, respectively, with the average LN volume of $18,081,250$ voxels. The segmentation methods were implemented in Matlab 7.12 (R2011a) without code optimization and evaluated on a desktop computer with the Intel® Xeon(R) CPU E5-2643 at 3.3GHz.

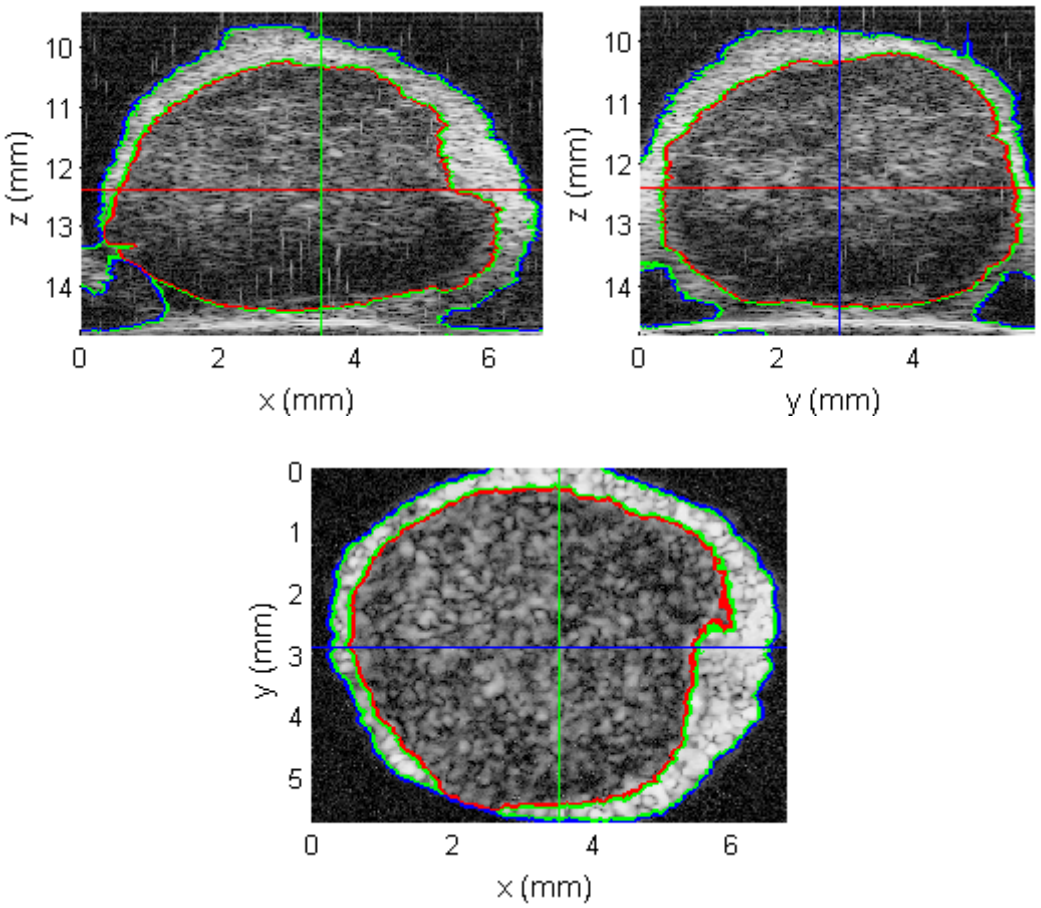

Figure 4.3: Three slices corresponding to three planes of a representative segmentation result overlaid on the B-mode image of a nonmetastatic LN. The DSCs for LN parenchyma, PNF and NS are 0.932, 0.855 and 0.981, respectively.

4.5 Discussion and Conclusions

These results show that the LRGDF segmentation method is robust to speckle noise in US data because the gamma distribution models the local data statistics well. When modeling positive real numbers, the gamma distribution will approximate the Gaussian distribution if its shape parameter is large. Therefore, the LRGDF method provides a more generalized model that could be adjusted to the special case of the local intensities distributed according to the Gaussian distribution [109, 111]. To demonstrate this point, Fig. 4.4 shows the results of the 2-phase LRGDF method applied to segment vessels in an X-ray image (first row) as well as in MRI images of left ventricle (second row) and tumor (last row). Although, the images present challenges such as weak boundaries, noise and intensity inhomogeneities, the LRGDF method correctly segments the regions of interest.

To handle the characteristic intensity inhomogeneities of US data, the mollifying kernel, $K_\rho(\mathbf{u})$,

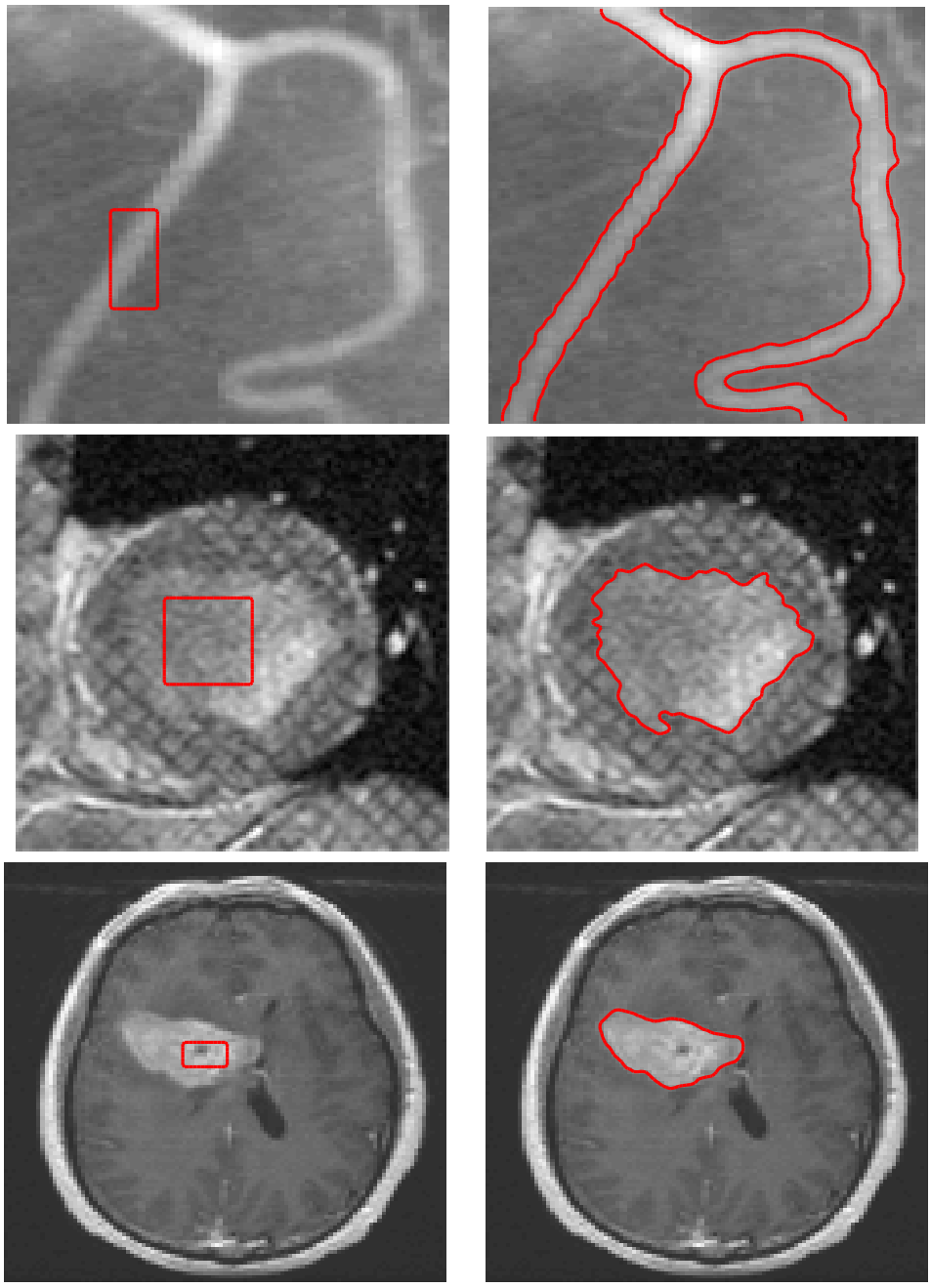

Figure 4.4: Results of the proposed method for segmentation of medical images (X-ray and MRI). For each row, initialization (left) and final result (right).

was employed to specify the local region statistics on a selected spatial scale. The choice of the scale parameter ρ is important in characterizing the localization property of this mollifying kernel because $K_\rho(\mathbf{u})$ is zero in $\left\{\mathbf{u} \in \mathbb{R}^N : |\mathbf{u}| > \rho\right\}$. When a small scale value ρ is selected, intensity inhomogeneities are handled better; however, segmentation becomes more sensitive to initialization. For larger value of ρ, the method is less dependent on initialization; however, intensity inhomogeneities can lead to incorrect segmentation results and computational cost is higher. We used the "coarse to fine" scheme to determine an optimized ρ value of 0.4 mm for the LN data set.

In conclusion, we presented a LRGDF segmentation method that deals well with speckle noise in US data and handles intensity inhomogeneities that typically are present in US data. The method provides more-accurate segmentation than the $\text{Seg}_{\text{Gauss}}$ method when applied to our data sets. Furthermore, the LRGDF method required less time to obtain final results because it converged faster than the $\text{Seg}_{\text{Gauss}}$ method. However, results still depend on initialization. The execution time significantly increases if initialization is too far from the correct boundary. Thus, future work will investigate an improved, automatic initialization technique for the LRGDF segmentation method.

Although the LRGDF method executes faster than the $\text{Seg}_{\text{Gauss}}$ method, it is still computationally expensive. Because the LN data were acquired with a high-frequency (HF), focused transducer, the intensity inhomogeneities in the LN envelope data are mostly due to the attenuation and focusing effects. Therefore, the data acquired from the same media within a limited axial depth (thickness) are relatively homogeneous. This seminal characteristics of the HFU data can be taken into account to develop a more efficient segmentation method. Chapter 5 will present an alternative solution to do so.

Chapter 5

Statistical Transverse-slice-based Level-set Segmentation Method[1]

5.1 Introduction

The LRGDF segmentation method presented in Chapter 4 was capable of segmenting ultrasound (US) data in the presence of data inhomogeneities. The ability of the method relies on the fact that it took into account the gamma statistics of data in local regions specified by the mollifying kernel. Depending on the level of data inhomogeneities, the scale parameter of the kernel and thus the kernel size can be adapted. For example, large scale parameters and kernel sizes make the method less dependent on initialization but weaken the method's ability to handle data inhomogeneities, and the computational cost becomes heavy. Furthermore, estimating the gamma-distribution parameters in local regions was the most computationally expensive part of the method because each local region required estimating its own set of parameters, and the number of local regions was large, especially in 3D datasets.

Understanding how data are acquired is essential to understand the sources causing data inhomogneities and thus data characteristics. As presented in Chapter 2, to acquire high resolution data, the lymph nodes (LN) were scanned using a single-element, spherically-focused, high-frequency transducer. Because of focusing and attenuation effects, the data evolved significantly with imaged depth, leading to the variability with depth of the statistical parameters of distributions modeling the envelope data. Therefore, the LN envelope data are mostly inhomogeneous along the axial

[1]This chapter is adapted from Thanh Minh Bui, Alain Coron, Jonathan Mamou, Emi Saegusa-Beecroft, Tadashi Yamaguchi, Eugene Yanagihara, Junji Machi, S. Lori Bridal, and Ernest J. Feleppa, "Local Transverse-slice-based Level-set Method for Segmentation of 3D, High-frequency Ultrasonic Backscatter from Dissected Human Lymph Nodes", IEEE Transactions on Biomedical Engineering (Resubmitted after getting review with decision "Minor Revisions")

direction (i.e., ultrasound beam direction) of the acquisition system. This important information should be taken into consideration when developing a method for segmenting the LN data.

Based on the axial inhomogeneity of the HFU LN envelope data, we chose to modify the form of the kernel used in the local-region based segmentation method developed in the previous chapter so that, instead of considering spherical kernels throughout the LN volume, local homogeneity was assumed within planes that were equidistant with respect to the ultrasound transducer. Thus transverse-slice masks were introduced to take into account the characteristic depth-dependence of HFU data. This statistical transverse slice based level-set (STS-LS) method provides segmentation envelope of HFU data acquired from these LNs in 3D into three phases (i.e., LN parenchyma (LNP), perinodal fat (PNF) and normal saline (NS)). This novel segmentation makes use of the tissue-dependent statistical distribution of envelope data in each of the three media and handles the depth-dependent nature of ultrasonic data by finding optimal statistical parameters for each tissue type within each transverse slice. A new energy function was developed by incorporating gamma distributions to model the three corresponding media (LNP, PNF, NS) in each transverse slice. The gamma-distribution parameters were then estimated from each of the 3 media in each transverse slice using the method of moments (MoM) as before. This refinement provided better efficiency and effectiveness for simulated and LN envelope data compared to the global-energy [63] and original Lankton region-based [110] segmentation methods.

5.2 Characterizing Spatial Variability of Lymph Node Envelope Data

Because of strong diffraction of the spherically-focused transducer and significant attenuation at high frequencies, the distribution parameters modeling the envelope data evolve significantly with imaged depth. The aims of this section are to demonstrate and characterize the variability of gamma-distribution parameters with depth in our data. Results are used to determine appropriately transverse slices so that data from a single tissue-type in each transverse slice can be considered as approximately homogeneous during subsequent segmentation.

Firstly, for each LN, fifteen non-overlapping, cylindrical ROIs with a length and diameter of 0.5 mm were extracted from manually-segmented LNP envelope data. The centers of the ROIs were

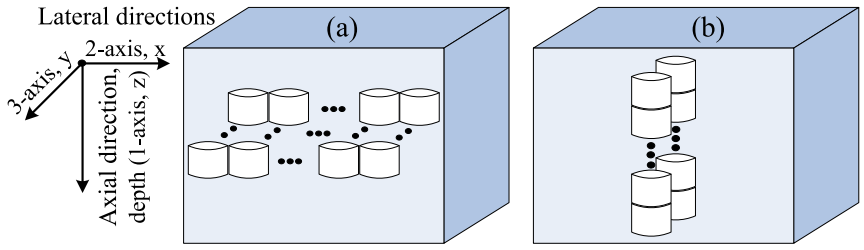

Figure 5.1: Illustration of the extraction of ROIs to evaluate data inhomogeneity. (a) ROIs were extracted from independent positions at fixed 12.2 mm depth to assess lateral inhomogeneity. (b) ROIs were extracted along the sound propagation direction (axial direction).

located at a fixed depth as illustrated in Fig. 5.1(a). In each ROI, two gamma-distribution parameters (shape-a, and scale-b) were estimated so that fifteen values for each parameter corresponding to the fifteen ROIs were obtained. We then computed the sample mean, $MEAN$, and sample standard deviation, STD, of the two gamma-distribution parameters over the 15 ROIs. These values were used to calculate the relative standard deviation (RSD), $RSD = \left|\frac{STD}{MEAN}\right| \times 100$, to obtain RSD_a^L and RSD_b^L for the parameters a and b (L stands for lateral direction). A lower percent RSD indicates a lower variability in the parameter set estimated from different ROIs of the same LN. For example, for each LN, RSD_a^L was obtained from fifteen shape parameters, a, estimated from the fifteen corresponding ROIs. In a similar way, the fifteen ROIs were extracted from independent depths along the sound propagation direction (axial direction) as presented in Fig. 5.1(b). In a similar way, the fifteen ROIs were extracted from independent depths along the sound propagation direction (axial direction) as presented in Fig. 5.1(b). In most LNs, we were able to extract 15 non-overlapped ROIs along the axial direction. In smaller nodes, the axial dimensions were not sufficient for this to be done. In such cases, to reach 15 non-overlapped ROIs, we randomly selected additional adjacent, non-overlapped ROIs but at the same depth. The centers of adjacent ROIs were 1 mm apart which should be sufficient to provide independent data using the transducer which has a lateral resolution at the focal zone of approximately 116 μm. RSD_a^A and RSD_b^A were then computed for the two gamma-distribution parameters (A stands for axial direction).

Fig. 5.2 shows the RSD of the two parameters of the gamma distribution acquired from ROIs in the LNP envelope data of 54 LNs. Fig. 5.2 indicates that:

1. The variability of the scale parameters (RSD_b^L, RSD_b^A) is much larger than that of the shape parameters (RSD_a^L, RSD_a^A).

2. The scale parameters obtained from ROIs along the axial direction present higher variability

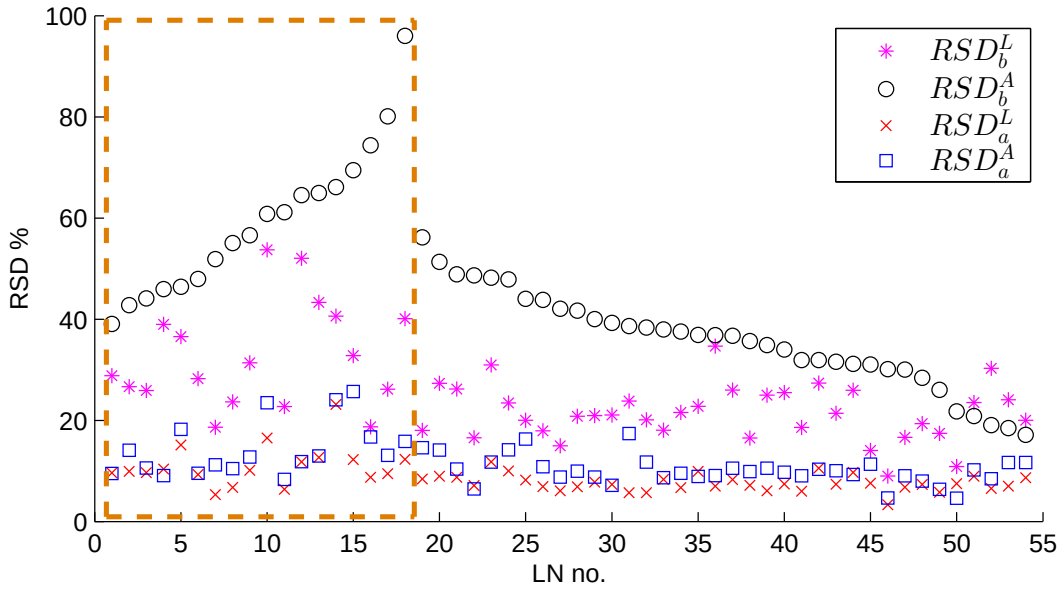

Figure 5.2: The relative standard deviation (RSD) of the gamma-distribution parameters modeling the LNP envelope data along the lateral (RSD_a^L, RSD_b^L) or axial (RSD_a^A, RSD_b^A) direction over 54 LNs. The 18 metastatic LNs are outlined with a dashed rectangular border. Note that LN numbers are arbitrary but consistent with Fig. 5.7.

than those along the lateral direction. Therefore, the data inhomogeneities along the axial direction are more severe than those along the lateral direction such that envelope data localized within a transverse slice with an appropriate thickness would be less inhomogeneous than data distributed across the depth of the LN.

3. The LNs with higher *RSD* values tend to be metastatic LNs. Thus, the acoustic speckle in HFU data from metastatic LNs is generally more inhomogeneous than that from non-metastatic LNs.

5.3 Segmentation Methods

In this section, we first summarize previous studies on region-based level-set segmentation methods and highlight their limitations when applied to the HFU data. We then describe our STS-LS segmentation method and justify its feasibility on our data set.

5.3.1 Related Methods

Let Ω be a bounded open subset of $\mathbb{R}^3$, and let $I : \Omega \to \mathbb{R}$ denote a 3D image to be segmented into an inner region Ω_1 and its complement Ω_2. Anquez *et al.* [63] proposed solving the segmentation problem by finding an optimal partition in the image domain. They employed the level-set framework and the maximum a posteriori (MAP) approach to formulate the following energy function that is minimized to obtain the segmentation result:

$$E_G(\phi, \theta_1, \theta_2) = \int_\Omega \mathscr{F}(\mathbf{x}, I, \phi)\, d\mathbf{x} + \mu \int_\Omega |\nabla H(\phi(\mathbf{x}))|\, d\mathbf{x}, \tag{5.1}$$

where the second term is the regularization term to keep the contour smooth. It can be noted that the regularization term is equal to $\mu|C|$, where $|C|$ is the surface area of the contour boundary C and μ is a weighting constant. The first term is the data fidelity term with an image criterion $\mathscr{F}(\mathbf{x}, \phi, I) = -H(\phi(\mathbf{x})) \ln p_1(I(\mathbf{x}); \theta_1) - (1 - H(\phi(\mathbf{x}))) \ln p_2(I(\mathbf{x}); \theta_2)$, H is the Heaviside function. The function $\phi : \Omega \to \mathbb{R}$ is the level-set function that implicitly represents the boundary contour (curve in 2D and surface in 3D) as its zero level-set ($\phi(\mathbf{x}) = 0$). Specifically, the sign of $\phi(\mathbf{x})$ defines the two regions: Ω_1, where $\phi(\mathbf{x}) > 0$, and Ω_2, where $\phi(\mathbf{x}) < 0$. Furthermore, $p_1(I(\mathbf{x}); \theta_1)$ and $p_2(I(\mathbf{x}); \theta_2)$ are the probability density functions (PDF) modeling the intensity distribution of data within the regions Ω_1 and Ω_2, respectively; θ_1 and θ_2 are the parameters of the corresponding PDFs estimated in a global way (i.e., using the whole inner Ω_1 and outer Ω_2 regions delimited by the contour).

Because the data fidelity term is computed in a global way, the method cannot handle data inhomogeneity (i.e., when data statistics vary spatially). In US imaging, data inhomogeneities may be caused by variations in the tissue structure and/or the presence of several tissue types. Speckle statistics may also evolve with imaged depth due to attenuation and acoustic focusing effects. These depth-dependent effects are particularly important in HFU as analyzed in Section 5.2.

To handle intensity inhomogeneities, Lankton *et al.* [110] proposed a local region-based framework reformulating segmentation energies in a local way. The localized region-based energy function to be minimized is as follows:

$$E_L(\phi) = \int_\Omega \delta(\phi(\mathbf{x})) \int_\Omega B(\mathbf{x}, \mathbf{y})\, \mathscr{F}(\mathbf{x}, \mathbf{y}, I, \phi, B)\, d\mathbf{y} d\mathbf{x} + \mu \int_\Omega |\nabla H(\phi(\mathbf{x}))|\, d\mathbf{x}, \tag{5.2}$$

where $\mathbf{x} = (x_1, x_2, x_3)$, $\mathbf{y} = (y_1, y_2, y_3) \in \Omega$; $\mathscr{F}(\mathbf{x}, \mathbf{y}, I, \phi, B)$ is a local image criterion; $B(\mathbf{x}, \mathbf{y})$ represents a mask function used to specify local regions (neighborhoods) as shown in Fig. 5.3(a) where local parameters driving the contour evolution are estimated. In other words, the parameters used to compute the image criterion $\mathscr{F}(\mathbf{x}, \mathbf{y}, I, \phi, B)$ at each $\mathbf{x}$ are locally estimated in the data within the mask specified by $B(\mathbf{x}, \mathbf{y})$.

It is worthwhile mentioning the energy functions proposed by Lankton et al. (Eq. (5.2)), Li et al. [109], Wang et al. [111] and our work in Chapter 4 (Eq. (4.1)) are similar in that they all take into account the properties of local inner and outer regions delimited by the zero-level of the level-set function representing the boundary. The methods differ, however, with respect to the ways by which the localization is specified and what kinds of image criteria are computed to handle different kinds of data. For example, to specify localization, in Eq. (5.2), the mask function $B(\mathbf{x}, \mathbf{y})$ is used; whereas Eq. (4.1) used the mollifying kernel function $K_\rho(\mathbf{u})$ with the property that $K_\rho(\mathbf{u})$ decreases and approaches zero as $|\mathbf{u}|$ increases.

To compute the energy $E_L(\phi)$ in Eq. (5.2), due to the presence of the $\delta(\phi(\mathbf{x}))$ Dirac function, only points near the contour are taken into account and intensity inhomogeneities arising far away are ignored, so the framework demonstrates its ability to segment images with intensity inhomogeneities. Lankton's framework is, however, more sensitive to initialization and also more computationally expensive than methods based on globally computed energies.

Flexibility in the neighborhood size (size of the mask specified by $B(\mathbf{x}, \mathbf{y})$) and the image criterion ($\mathscr{F}(\mathbf{x}, \mathbf{y}, I, \phi, B)$) provided in Lankton's framework can be adapted for the segmentation of specific types of data, e.g., HFU. The mask size can be adapted based on the scale of object(s) of interest and the spatial scale of the data inhomogeneities. In the original paper [110], three kinds of image criteria, $\mathscr{F}(\mathbf{x}, \mathbf{y}, I, \phi, B)$, including uniform modeling, mean separation and histogram separation energies were considered. Yet, none of these criteria makes use of prior knowledge about US speckle statistics.

5.3.2 Two-phase Statistical Transverse-slice-based Level-set (STS-LS) Method

The proposed STS-LS segmentation method is adapted from the localized energy function in Lankton's framework Eq. (5.2) modified with respect to the shape of the mask specified by $B(\mathbf{x}, \mathbf{y})$ and the image criterion $\mathscr{F}(\mathbf{x}, \mathbf{y}, I, \phi, B)$. The method will first be developed in two phases and then

extended to the three phases necessary for segmentation of the LN data. Unlike Lankton's framework that used a spherical mask in the image criterion (see Fig. 5.3(a)), we introduce an additional mask B_T for computing the image criterion. Furthermore, the gamma PDF is employed, and its associated parameters are estimated within the new mask B_T. The energy function is as follows:

$$E_L(\phi) = \int_{\Omega} \delta(\phi(\mathbf{x})) \int_{\Omega} B(\mathbf{x},\mathbf{y}) \mathscr{F}_S(\mathbf{x},\mathbf{y},I,\phi,B_T)\, d\mathbf{y} d\mathbf{x} + \mu \int_{\Omega} |\nabla H(\phi(\mathbf{x}))|\, d\mathbf{x}. \tag{5.3}$$

In our context, the mask function $B_T(\mathbf{x},\mathbf{y}) = B_T(x_1,y_1)$ specifies a transverse slice B_{T,x_1} as presented in Fig. 5.3(b) and (c). Specifically, the transverse slice, B_{T,x_1}, has the same length (second dimension) and width (third dimension) as the image I and a thickness of h so that $B_T(x_1,y_1)$ equals 1 where $|y_1 - x_1| < h/2$ and zero elsewhere. Selecting a transverse slice provides efficiency for the energy function calculation (Eq. (5.3)) because all points at the same depth and belonging to the same medium are described by the same PDF distribution parameters. This efficiency is directly associated with the data dimensionality, i.e., the higher the data dimensionality, the higher efficiency will be gained when compared to the Lankton's framework. In the energy function (Eq. (5.3)), we kept a mask function $B(\mathbf{x},\mathbf{y})$ but it deliberately specifies a small region $B_{\mathbf{x}}$ centered at $\mathbf{x}$ for which $B(\mathbf{x},\mathbf{y}) = 1$. The small region $B_{\mathbf{x}}$ was used to specify local regions around the zero-level of the level-set function for which the image criteria were computed and summed up.

The image criterion $\mathscr{F}_S(\mathbf{x},\mathbf{y},I,\phi,B_T)$ includes the log-probability of the intensity $I(\mathbf{x})$ with parameter $\theta_i(y_1)$ estimated for points $\mathbf{y}$ belonging to $B_{\mathbf{x}}$:

$$\mathscr{F}_S(\mathbf{x},\mathbf{y},I,\phi,B_T) = -\sum_{i=1}^{2} \lambda_i M_i(\phi(\mathbf{y})) \ln p_i(I(\mathbf{x});\theta_i(y_1)), \tag{5.4}$$

where $M_1(\phi(\mathbf{y})) = H(\phi(\mathbf{y}))$, and $M_2(\phi(\mathbf{y})) = 1 - H(\phi(\mathbf{y}))$ are the membership functions. The two positive constants, λ_1, λ_2, are introduced to weight the local interior and exterior energies. The PDFs $p_1(I(\mathbf{x});\theta_1(y_1))$ and $p_2(I(\mathbf{x});\theta_2(y_1))$ are gamma PDFs. $\theta_i(y_1) = (a_i(y_1), b_i(y_1))$, $i = 1,2$, are the local gamma-distribution parameters which are spatially varied according image depths.

The parameters of each PDF are estimated within the data specified by transverse slice and each

membership function as follows :

$$\hat{\theta}_i(y_1) = \arg\min_{\theta_i(y_1)} \left(- \int_{\Omega_i(y_1)} B_T(x_1, y_1) \ln p_i(I(\mathbf{x}); \theta_i(y_1)) \, d\mathbf{x} \right). \tag{5.5}$$

Because the maximum likelihood approach does not provide a closed-form expression for estimating the gamma-distribution parameters, the MoM [115] is used to estimate the two gamma-distribution parameters as $\hat{a}_i(y_1) = \frac{\hat{m}_i^2(y_1)}{\hat{v}_i(y_1)}$, $\hat{b}_i(y_1) = \frac{\hat{v}_i(y_1)}{\hat{m}_i(y_1)}$, where $\hat{m}_i(y_1)$ and $\hat{v}_i(y_1)$ are the sample mean and sample variance estimated in local regions $\Omega_i(y_1)$, specified by the transverse slice and the membership functions (i.e., $H(\phi)$ and $1 - H(\phi)$), as follows:

$$\begin{cases} \hat{m}_i(y_1) = \dfrac{1}{|\Omega_i(y_1)|} \int_{\mathbf{y} \in \Omega_i(y_1)} I(\mathbf{x}) \, d\mathbf{x}, \\ \hat{v}_i(y_1) = \dfrac{1}{|\Omega_i(y_1)|} \int_{\mathbf{y} \in \Omega_i(y_1)} (I(\mathbf{x}) - \hat{m}_i(y_1))^2 \, d\mathbf{x}. \end{cases} \tag{5.6}$$

The minimization of $E_L(\phi)$ with respect to ϕ (with fixed θ_i) can be achieved by taking the Euler-Lagrange equation and updating the level-set function by the gradient descent method (see Appendix B for detailed derivation):

$$\begin{cases} \dfrac{\partial \phi}{\partial t} = \delta(\phi(\mathbf{x})) \left[F_D(\mathbf{x}) + \mu \operatorname{div}\left(\dfrac{\nabla \phi(\mathbf{x})}{|\nabla \phi(\mathbf{x})|} \right) \right], \\ F_D(\mathbf{x}) = \int_\Omega B(\mathbf{x}, \mathbf{y}) \, \delta(\phi(\mathbf{y})) \ln \dfrac{\left[p_1\left(I(\mathbf{y}); \hat{\theta}_1(x_1)\right) \right]^{\lambda_1}}{\left[p_2\left(I(\mathbf{y}); \hat{\theta}_2(x_1)\right) \right]^{\lambda_2}} d\mathbf{y}. \end{cases} \tag{5.7}$$

In the level-set evolution equation (5.7), the second term, $\delta(\phi(\mathbf{x})) \mu \operatorname{div}(\nabla \phi(\mathbf{x}) / |\nabla \phi(\mathbf{x})|)$, has a smoothing effect on the zero-level surface to maintain the regularity of the surface. The first term, $\delta(\phi(\mathbf{x})) F_D$, is the data term derived from the local intensity distributions $p_1\left(I(\mathbf{y}); \hat{\theta}_1(x_1)\right)$ and $p_2\left(I(\mathbf{y}); \hat{\theta}_2(x_1)\right)$. It plays a key role in the evolution of the surface since it is responsible for driving the surface toward the object boundaries. This evolution equation is rather similar to the one derived by Lankton et al. [110] using Gaussian PDFs with the same variance:

$$\begin{cases} \dfrac{\partial \phi}{\partial t}(\mathbf{x}) = \delta(\phi(\mathbf{x})) \left[F_D(\mathbf{x}) + \mu \operatorname{div}\left(\dfrac{\nabla \phi(\mathbf{x})}{|\nabla \phi(\mathbf{x})|} \right) \right], \\ F_D(\mathbf{x}) = \int_\Omega B(\mathbf{x}, \mathbf{y}) \, \delta(\phi(\mathbf{y})) \left[(I(\mathbf{y}) - m_2(x_1))^2 - (I(\mathbf{y}) - m_1(x_1))^2 \right]. \end{cases} \tag{5.8}$$

However, the image criterion (5.4)) is slightly different from the Lankon's image criterion $\mathscr{F}_{UM}$:

$$\mathscr{F}_{UM}(\mathbf{x},\mathbf{y},I,\phi,B) = -\sum_{i=1}^{2} \lambda_i M_i(\phi(\mathbf{y})) \left[(I(\mathbf{y}) - m_2(\mathbf{x}))^2 - (I(\mathbf{y}) - m_1(\mathbf{x}))^2 \right], \tag{5.9}$$

regarding the role of $\mathbf{x}$ and $\mathbf{y}$. This point is discussed in Section 5.5.2.

5.3.3 Multiphase Level-set Formulation for Lymph Node Segmentation

A multiphase approach is implemented to allow simultaneous segmentation of multiple objects [116, 117]. To correctly segment the LNP, PNF, and NS ($N = 3$), we use two level-set functions (ϕ_1, ϕ_2) (as in Section 4.2.2.1) to define 3 membership functions $M_1(\phi_1,\phi_2)$, $M_2(\phi_1,\phi_2)$, $M_3(\phi_1,\phi_2)$ corresponding to the three regions. The LNP, PNF and NS regions are modeled by the $p_1(I(\mathbf{x});\theta_1(y_1))$, $p_2(I(\mathbf{x});\theta_2(y_1))$ and $p_3(I(\mathbf{x});\theta_3(y_1))$ gamma distributions, respectively. The membership functions $M_1(\phi_1,\phi_2) = H(\phi_1)H(\phi_2)$, $M_2(\phi_1,\phi_2) = (1-H(\phi_1))H(\phi_2)$ and $M_3(\phi_1,\phi_2) = 1-H(\phi_2)$ give a three-phase level-set formulation. The energy function, $E(\phi_1,\phi_2) = E_1(\phi_1,\phi_2) + E_2(\phi_1,\phi_2)$, where $E_k(\phi_1,\phi_2)$, $k = 1,2$, is expressed as follows:

$$E_k(\phi_1,\phi_2) = \int_\Omega \delta\phi_k(\mathbf{x}) \int_\Omega B(\mathbf{x},\mathbf{y}) \mathscr{F}_S(\mathbf{x},\mathbf{y},I,\phi_1,\phi_2,B_T)\, d\mathbf{y} d\mathbf{x} + \mu_k \int_\Omega |\nabla H\phi_k(\mathbf{x})|\, d\mathbf{x}, \tag{5.10}$$

where $\mathscr{F}_S(\mathbf{x},\mathbf{y},I,\phi_1,\phi_2,B_T) = -\sum_{i=1}^{3} \lambda_i M_i(\phi_1(\mathbf{y}),\phi_2(\mathbf{y})) \ln p_i(I(\mathbf{x});\theta_i(y_1))$, and λ_1, λ_2 and λ_3 are positive constants. The minimization of $E(\phi_1,\phi_2)$ with respect to ϕ_k (with fixed θ_1, θ_2, θ_3) can be achieved using the gradient descent method by solving the following evolution equations (see Appendix B for detailed derivation):

$$\begin{cases} \dfrac{\partial\phi_1}{\partial t} = \delta(\phi_1(\mathbf{x})) \left[F_{D1}(\mathbf{x}) + \mu_1 \mathrm{div}\left(\dfrac{\nabla\phi_1(\mathbf{x})}{|\nabla\phi_1(\mathbf{x})|} \right) \right] \\ F_{D1}(\mathbf{x}) = H(\phi_2(\mathbf{x})) \int_\Omega B(\mathbf{x},\mathbf{y}) \left(\sum_{k=1}^{2} \delta(\phi_k(\mathbf{y})) \right) \ln \dfrac{\left[p_1\left(I(\mathbf{y});\hat{\theta}_1(x_1)\right) \right]^{\lambda_1}}{\left[p_2\left(I(\mathbf{y});\hat{\theta}_2(x_1)\right) \right]^{\lambda_2}} d\mathbf{y} \\ \dfrac{\partial\phi_2}{\partial t} = \delta(\phi_2(\mathbf{x})) \left[F_{D2}(\mathbf{x}) + \mu_2 \mathrm{div}\left(\dfrac{\nabla\phi_2(\mathbf{x})}{|\nabla\phi_2(\mathbf{x})|} \right) \right] \\ F_{D2}(\mathbf{x}) = \int_\Omega B(\mathbf{x},\mathbf{y}) \left(\sum_{k=1}^{2} \delta(\phi_k(\mathbf{y})) \right) \left[H(\phi_1(\mathbf{x})) \ln \dfrac{\left[p_1\left(I(\mathbf{y});\hat{\theta}_1(x_1)\right) \right]^{\lambda_1}}{\left[p_2\left(I(\mathbf{y});\hat{\theta}_2(x_1)\right) \right]^{\lambda_2}} + \ln \dfrac{\left[p_2\left(I(\mathbf{y});\hat{\theta}_2(x_1)\right) \right]^{\lambda_2}}{\left[p_3\left(I(\mathbf{y});\hat{\theta}_3(x_1)\right) \right]^{\lambda_3}} \right] d\mathbf{y}. \end{cases} \tag{5.11}$$

The weighting constants, λ_i, $i = 1,2,3$, play an important role in the evolution equations (5.11).

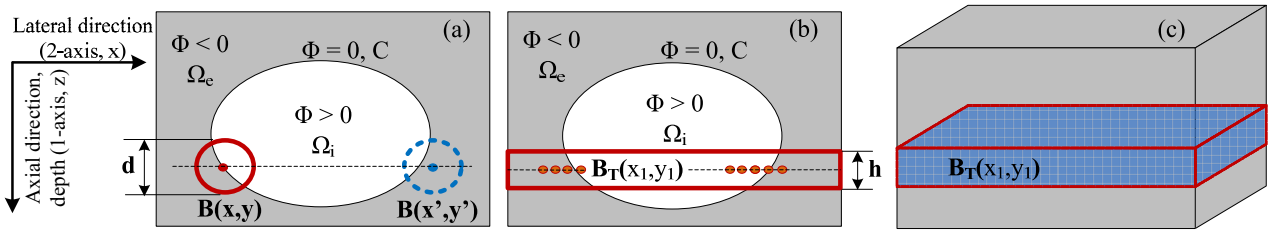

Figure 5.3: A cross section of the 3D data representing the level-set framework for segmentation of an object and the shape of a proposed transverse slice in 3D. The contour, C, identifying the boundary of the object is implicitly defined as $\phi = 0$. (a) Lankton's method uses the mask function, $B(\mathbf{x},\mathbf{y})$, to specify a spherical mask for each point along the contour. (b) the proposed method, where the mask function $B_T(x_1,y_1)$ delimits an area of the red rectangle as the transverse slice. All points $\mathbf{x}$ under evaluation having the same depth (distance to transducer - 1-axis) share the same transverse slice. Each transverse slice is split by the contour into the local interior and local exterior regions. (c) the shape of a transverse slice is presented in 3D.

Because the values of LN envelope data are less than 1 ($\approx 10^{-3}$V), the values of PDFs $p_i(.)$, $i = 1,2,3$, are greater than 1 as indicated in Fig. 3.7 and 3.9 in Chapter 3. Therefore, when $\lambda_1 > \lambda_2$ the evolution surface represented by ϕ_1 tends to inflate toward the object boundaries and vice versa. The tuning of the two weighting constants is useful, especially when the data topology is known. This tuning helps the level-set function converge faster and avoids convergence to unexpected local minima. Particularly, because the LNP is surrounded by the fat and NS media, we initialize the level-set function ϕ_1 as a signed distance function of a small ellipsoid within the LNP region, and choose $\lambda_1 > \lambda_2$. Then the evolution surface represented by ϕ_1 will expand toward the LNP boundaries.

5.3.4 Implementation

To improve the computational efficiency and accuracy of the proposed STS-LS method, three strategies were combined: narrow band [120], multiresolution [121] and good initializations. A narrow band technique [120] was applied so that only points close to a zero level-set function were considered. Using a multiresolution technique, the original data were down sampled by a factor of 2 in each dimension and the segmentation results obtained on the down sampled version were then up sampled to the same factor and used to initialize the full-resolution segmentation. This multiresolution technique decreased computation time while also helping to avoid incorrect local minima that would otherwise lead to inaccurate segmentation. Finally, good initialization for the two level-set functions, ϕ_1 and ϕ_2 plays an important role in the final segmentation results. To

facilitate comparison, the same initialization techniques presented in Section 4.2.2.2 of Chapter 4 were used for all segmentation methods in this chapter.

Pseudo code for the segmentation of LN data is presented in Algorithm 5.1. The two level-set functions, ϕ_1, ϕ_2, were reinitialized every 4 iterations by computing the signed distance map to their corresponding zero level-set [122] in order to preserve their regularity. The Heaviside and Dirac delta functions were replaced by their smoothed versions, $H_\varepsilon(x)$ and $\delta_\varepsilon(x)$ as in Equations (4.7) and (4.8), respectively. Regarding the convergence criterion, the segmentation algorithm stops when the partition of the image is stationary (i.e., the image partition does not evolve significantly between two consecutive reinitializations) or when the number of iterations reaches a certain value (e.g., 250 for the LN data).

5.4 Results

The STS-LS segmentation method was evaluated using clinical LN envelope data and simulated data mimicking the characteristics of LN envelope data. Similar to Chapter 4, the success of the segmentation method was quantified using the Dice similarity coefficient (DSC) to compare automatic segmentation result with reference result (the ground truth data in case of the simulated data or the expert manual segmentation in case of the clinical LN envelope data).

5.4.1 Results on Simulated Data

The STS-LS segmentation method successfully demarcated the 3 regions in the simulated data by providing high DSC values. For 20, 3D simulated data sets, the DSC values of LNP, PNF and NS regions were 0.981 ± 0.001, 0.914 ± 0.002 and 0.974 ± 0.001. Fig. 5.4 presents slices showing the initializations and their corresponding segmentation results to demonstrate the success of the proposed method. Note that the segmentation method was evaluated with the parameter settings: $\mu_1 = 0.2$, $\mu_2 = 0.2$, $\lambda_1 = 1.0$, $\lambda_2 = 1.0$, $\lambda_3 = 1.0$, $h = 0.5$ mm. Accurate segmentation results were obtained in about 120 iterations.

Algorithm 5.1 Segmentationof the LN data in each resolution

Input: I: image to segment defined on Ω; $\mathbf{x}$: voxel; ϕ_{01}, ϕ_{02}: initialization for ϕ_1, ϕ_2 functions; h: the thickness of the transverse slice; μ_1, μ_2: regularization parameters; λ_1, λ_2, λ_3: positive weighting constants.
Result: seg(I): Segmentation result, LNP: $\phi_1 > 0$, $\phi_2 > 0$; PNF: $\phi_1 < 0$, $\phi_2 > 0$; NS: $\phi_2 < 0$.

$\phi_1 \leftarrow \phi_{01}$; $\phi_2 \leftarrow \phi_{02}$;
its = 0
while convergent criterion is not met **do**
    its $\leftarrow$its + 1;
    Find the indices of the voxels belonging to the narrow band areas of ϕ_1, ϕ_2.
    Identify the transverse slice with the thickness of h for all the voxels belonging to the narrow band areas.
    for each $\mathbf{x}$ belonging to narrow band areas having different depth **do**
        Estimate the gamma-distribution parameters in local regions specified by membership functions (M_1, M_2, M_3) and the transverse slices.
        Assign similar values for parameters of the points that have the same depth and belong to the same local region.
    end for
    Compute $\frac{\partial \phi_1(\mathbf{x})}{\partial t}$, $\frac{\partial \phi_2(\mathbf{x})}{\partial t}$ using (5.11);
    $\triangle t_1 = 0.8/\max\left(\frac{\partial \phi_1(.)}{\partial t}\right)$;
    $\triangle t_2 = 0.8/\max\left(\frac{\partial \phi_2(.)}{\partial t}\right)$;
    $\phi_1(\mathbf{x}) \leftarrow \phi_1(\mathbf{x}) + \triangle t_1 \frac{\partial \phi_1(\mathbf{x})}{\partial t}$;
    $\phi_2(\mathbf{x}) \leftarrow \phi_2(\mathbf{x}) + \triangle t_2 \frac{\partial \phi_2(\mathbf{x})}{\partial t}$;
    if modulo(its,4)$\equiv$ 0 **then**
        $\phi_1(\mathbf{x}) \leftarrow$reinitialization$(\phi_1(\mathbf{x}))$;
        $\phi_2(\mathbf{x}) \leftarrow$reinitialization$(\phi_2(\mathbf{x}))$;
    end if
end while
seg(I) = binarize(ϕ_1, ϕ_2);

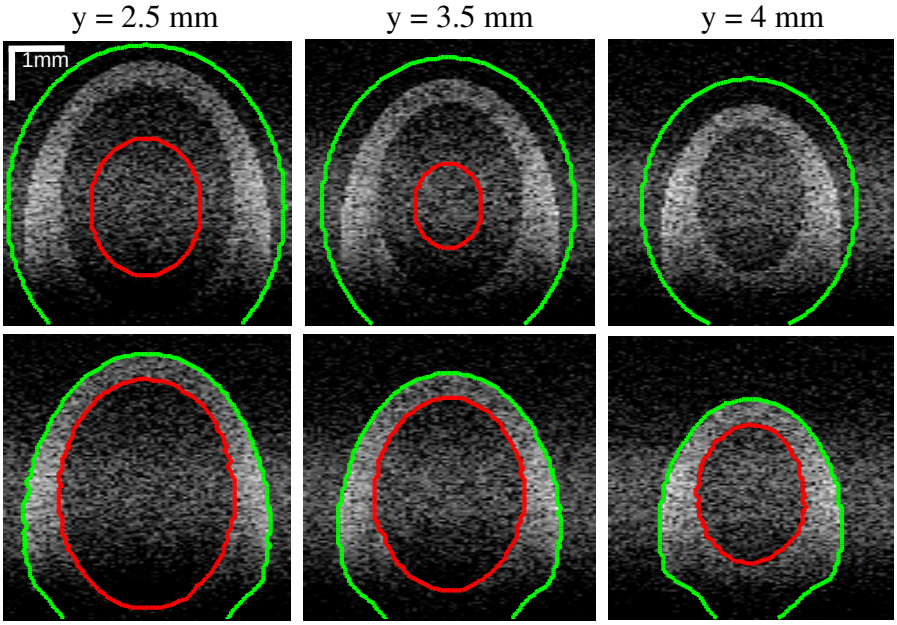

Figure 5.4: Three slices showing segmentation results obtained from simulated volumetric data. Initializations (upper row) and their corresponding segmentation results (bottom row).

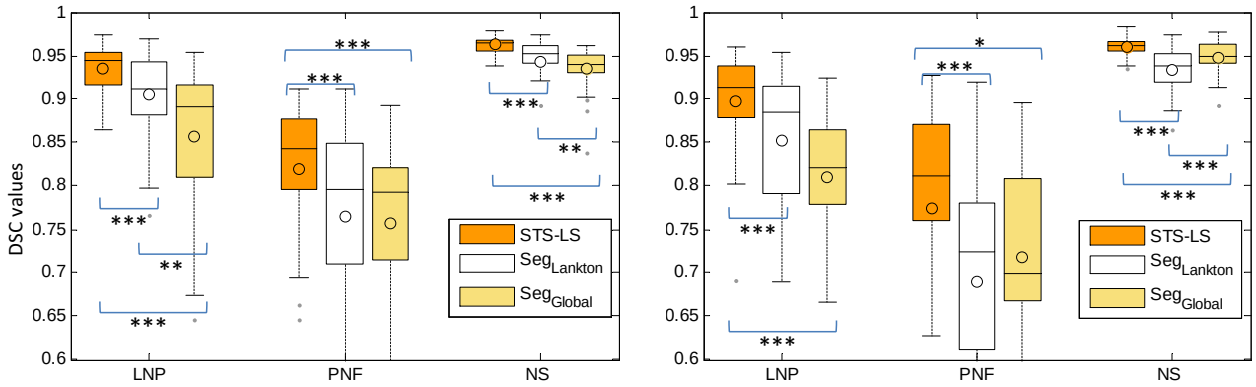

Figure 5.5: Boxplots showing the distributions of DSC values obtained from 3 segmentation methods for the 3 media in 54 colorectal LNs (left) and 30 breast LNs (right). The asterisks *, ** and *** indicates that the p values estimated according to the Wilcoxon paired, signed-rank test lower than the adjusted (i.e., Bonferroni correction) significance levels $\alpha = 0.017$, $\alpha/5$ and $\alpha/50$, respectively.

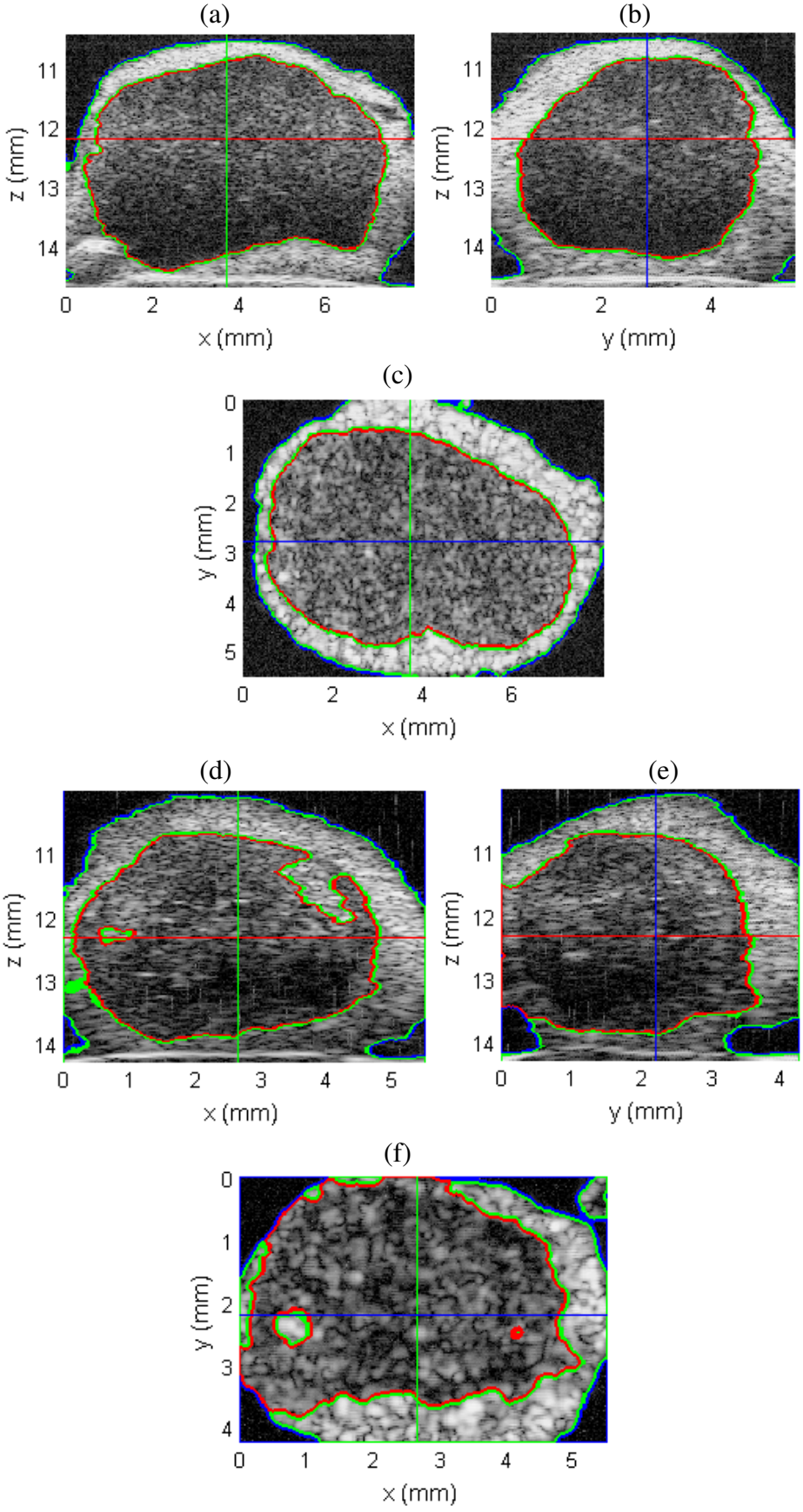

Figure 5.6: Segmentation results overlaid on the B-mode images corresponding to 3 planes. (a, b, c) Slices extracted from the best segmentation result of a nonmetastatic LN, the Dice coefficients for LNP, PNF and NS are 0.975, 0.899 and 0.965, respectively. (d, e, f) Slices extracted from the worst segmentation result of a metastatic LN, the Dice coefficients for LNP, PNF and NS are 0.883, 0.825 and 0.956, respectively.

5.4.2 Results on Clinical Lymph Node Database

We also evaluated the STS-LS method using the US envelope data of the database of 54 LNs dissected from colorectal cancer patients and 30 LNs dissected from breast-cancer patients. The database was divided into two groups based on primary-tumor organ because segmentation of the breast LNs is more challenging than that of colorectal LNs due to their more complicated shape and topology. The whole database was processed with the optimal set of parameters: $\mu_1 = 0.2$, $\mu_2 = 0.2$, $\lambda_1 = 1.04$, $\lambda_2 = 1.0$, $\lambda_3 = 1.0$ and $h = 0.7$ mm. We also compared the performance of the STS-LS method with two other methods denoted $\text{Seg}_{\text{Global}}$ and $\text{Seg}_{\text{Lankton}}$. The $\text{Seg}_{\text{Global}}$ method was proposed by Anquez *et al.* [63], adapted to the 3-phase level-set method formulated in the global way by using the gamma distribution to model the LNP, PNF and NS regions. The second method, $\text{Seg}_{\text{Lankton}}$, is based on the original Lankton's framework, adapted to 3 phases with the radius of the local region of 0.7 mm, we inserted in the framework the local energy functions formulated by using the gamma distribution to model the LNP, PNF and NS regions. Therefore, the STS-LS method differs from the $\text{Seg}_{\text{Lankton}}$ in terms of the shape of the mask (i.e., instead of a spherical local region, a transverse slice is considered). The same initializations were used for all three methods.

Fig. 5.5 presents the performance of the STS-LS, $\text{Seg}_{\text{Global}}$ and $\text{Seg}_{\text{Lankton}}$ methods on our databases. The STS-LS method outperforms the two other methods by providing higher DSC values for the three media. The DSC values for LNP, PNF and NS media are 0.935 ± 0.027, 0.820 ± 0.083 and 0.963 ± 0.009, respectively, for colorectal LNs, and 0.900 ± 0.057, 0.774 ± 0.137 and 0.961 ± 0.011, respectively, for breast LNs. The STS-LS method provided almost perfect results for the NS region. For the PNF region, we obtained slightly lower mean DSC values because the PNF region is thin and has a high variation in the shape. The Friedman test indicated a statistically significant difference in the DSC values depending on the segmentation methods (p values less than 10^{-10} for the three media of the 54 colorectal-cancer LNs, and p values less than 10^{-6} for the three media in the 30 breast-cancer LNs). The nonparametric Friedman test was used because it does not assume normality of the data distributions. To examine which pairs of methods provided significantly different DSC values for the three different combinations of methods (STS-LS vs. $\text{Seg}_{\text{Lankton}}$, $\text{Seg}_{\text{Lankton}}$ vs. $\text{Seg}_{\text{Global}}$ and $\text{Seg}_{\text{Global}}$ vs. STS-LS), we applied the Wilcoxon paired, signed-rank tests with a Bonferroni correction [123] resulting in a significance level set at $\alpha = 0.05/3 = 0.017$. For the 54 colorectal LNs, there were statistically significant differences

in the DSC values between the STS-LS and $\text{Seg}_{\text{Lankton}}$ methods and between the STS-LS and $\text{Seg}_{\text{Global}}$ methods ($p < 0.7 \times 10^{-4}$ for the three media); there were also significant differences in the DSC values between the $\text{Seg}_{\text{Lankton}}$ and $\text{Seg}_{\text{Global}}$ methods for the LNP ($p = 0.001$) and NS ($p = 0.0005$) media, whereas there was no statistically significant difference in the DSC values between the $\text{Seg}_{\text{Lankton}}$ and $\text{Seg}_{\text{Global}}$ methods for the PNF medium ($p = 0.65$). For the 30 breast LNs, there were statistically significant differences in the DSC values between the STS-LS and the $\text{Seg}_{\text{Lankton}}$ methods and between the STS-LS and $\text{Seg}_{\text{Global}}$ methods ($p < 0.004$ for the three media); there was also significant difference in the DSC values between the $\text{Seg}_{\text{Lankton}}$ and $\text{Seg}_{\text{Global}}$ methods for the NS medium ($p = 0.2 \times 10^{-4}$), whereas there were no statistically significant differences in the DSC values between the $\text{Seg}_{\text{Lankton}}$ and $\text{Seg}_{\text{Global}}$ methods for the LNP ($p = 0.04$) and PNF ($p = 0.4$) media.

Fig. 5.6 presents the best and the worst LNP segmentation results of the STS-LS method. As visually shown in Fig. 5.6(a-c), the method nearly perfectly demarcates the three regions in the envelope data. Conversely, Fig. 5.6(d-f) shows the worst segmentation result acquired from a metastatic LN. Because the envelope data exhibit the intensity variability with small high intensity regions within the LNP, the method misidentifies these regions as PNF.

To further examine and compare the performance of the three methods, Fig. 5.7 displays DSC values obtained for LNP segmentation applied to each of the 54 colorectal LNs. The STS-LS method outperforms the $\text{Seg}_{\text{Lankton}}$ method in most of the LNs (i.e., 38 out of 54). In addition, the STS-LS method demonstrates its robustness in case of metastatic LNs in which the $\text{Seg}_{\text{Global}}$ method almost fails. This result was anticipated because the metastatic LNs are more inhomogeneous than the nonmetastatic LNs as indicated in Section 5.2. Although the $\text{Seg}_{\text{Global}}$ method performs better in nonmetastatic LNs, it is still outperformed by the STS-LS method.

Table 5.1 presents the average segmentation time for the three methods applied to the 54 colorectal LNs. The computational load of $\text{Seg}_{\text{Lankton}}$ method increases dramatically when extending to higher dimension, whereas the proposed method provides computational efficiency approaching that of the $\text{Seg}_{\text{Global}}$ method. Note that all the segmentation methods have been implemented using Matlab 7.12 (R2011a) and evaluated on a Desktop computer with the Intel® Xeon (R) CPU E5-2643 at 3.3 GHz.

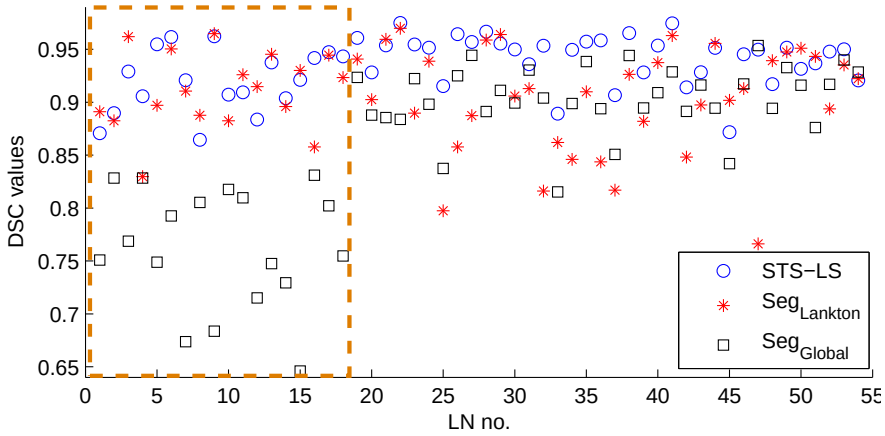

Figure 5.7: DSCs for LNP over 54 colorectal LNs. The 18 metastatic LNs are outlined with a dashed rectangular border.

Table 5.1: Average segmentation time (in minutes) over 54 colorectal LNs.

STS-LS	$\text{Seg}_{\text{Lankton}}$	$\text{Seg}_{\text{Global}}$
20.9 ± 14.4	434.3 ± 255.7	17.6 ± 14.1

5.5 Discussion

5.5.1 General Discussion

A novel, automatic STS-LS segmentation method has been described in this chapter and applied to segmentation of LNP, PNF and NS in LN envelope, HFU data. The method is robust to acoustic speckle, deals well with the depth-dependent intensity inhomogeneity in the envelope data, and is efficient.

Because of significant attenuation and focusing effects in the HFU data, the segmentation technique needed to remain robust in spite of axial inhomogeneities in the data. Data inhomogeneities with imaged depth caused by attenuation and focusing effects were handled well by transverse slices where the gamma-distribution parameters are estimated. The thickness, h, of the transverse slice can be adjusted depending on the spatial scale of the focusing and attenuation-based inhomogeneities. Specifically, smaller values of h handle data inhomogeneities better, but cause the variance of the estimated gamma-distribution parameters to increase and the segmentation to become more sensitive to initialization. Whereas large values of h cause segmentation to be less dependent on initialization but less able to handle data inhomogeneities well. When h has the size of the entire segmented image, then the STS-LS method is identical to the $\text{Seg}_{\text{Global}}$ method.

Note that this approach for dealing with axial inhomogeneities of data could be extended to other biomedical-imaging applications in HFU, such as segmentation of skin lesions [93].

Lateral inhomogeneities in the LNP data also influence segmentation performance. Such inhomogeneity is demonstrated, even for the nonmetastatic LNs, by RSD values greater than 10% along the lateral dimension of the LNP for the gamma-distribution scale parameter (Fig. 5.2). The metastatic LNs generally are larger and more inhomogeneous than the nonmetastatic ones as reflected by higher RSD values of the gamma-distribution parameters presented in Fig. 5.2. Because the STS-LS method is more robust to the data inhomogeneities than the $\text{Seg}_{\text{Global}}$ method, it provided more-accurate segmentation even in metastatic LNs that were poorly segmented by the $\text{Seg}_{\text{Global}}$ method (Fig. 5.7). In addition, the STS-LS method provided more-accurate segmentation than the $\text{Seg}_{\text{Lankton}}$ method because it is less sensitive to initialization than the $\text{Seg}_{\text{Lankton}}$ method.

When dealing with 3D data, minimizing the segmentation time is a very important consideration for the design of a practical segmentation technique. The execution time of the STS-LS method is approximately the same as that for the $\text{Seg}_{\text{Global}}$ method while the $\text{Seg}_{\text{Lankton}}$ method is very computationally expensive (Table 5.1). The efficiency of the segmentation methods depends on the number of gamma-distribution parameters estimated during the energy minimization process. For example, assuming that the methods are applied to a 3D data set with a size of $N \times M \times K$, where N is the depth dimension, then for each iteration, the $\text{Seg}_{\text{Global}}$ method requires the estimation of 3×2 parameters corresponding to the three segmented media for the two parameters (shape-a, scale-b) of the gamma distribution. The STS-LS method requires estimation of approximately $3 \times N \times 2$ parameters. Meanwhile, the $\text{Seg}_{\text{Lankton}}$ method requires estimation of $5 \times \sigma \times N \times M \times K \times 2$ parameters ($2 \times \sigma \times N \times M \times K \times 2$ for ϕ_1 and $3 \times \sigma \times N \times M \times K \times 2$ for ϕ_2), where σ ranges between 5% and 8% depending on the architectural properties of the LNs because the narrow band technique was used. Note that the number of voxels involved in the estimation of each parameter of the $\text{Seg}_{\text{Lankton}}$ method is smaller than that of the STS-LS method, which in turn is smaller than that of the $\text{Seg}_{\text{Global}}$ method. Thus the execution time does not increase proportionally to the difference in the number of estimated parameters but it exhibits a correlation. Furthermore, if the STS-LS method is implemented using C/C++, the execution time will be significantly reduced.

5.5.2 Discussion on the Image Criterion

The image criterion Eq. (5.4) is not the log-likelihood of the regions and leads to the evolution equation (5.7). We now consider the image criterion derived from the log-likelihood of the regions:

$$\begin{aligned}\mathscr{F}_{\mathscr{L}}(\mathbf{x},\mathbf{y},I,\phi,B_T) = &-\lambda_1 H(\phi(\mathbf{y}))\ln p_1(I(\mathbf{y});\theta_1(x_1)) \\ &-\lambda_2(1-H(\phi(\mathbf{y})))\ln p_2(I(\mathbf{y});\theta_2(x_1)).\end{aligned} \tag{5.12}$$

Note that the variables $\mathbf{y}$ and x_1 are exchanged in $p_i(.)$ functions as compared to Eq. (5.4). The evolution equation is (see Appendix B for detailed derivation)

$$\begin{cases}\dfrac{\partial\phi}{\partial t} = \delta(\phi(\mathbf{x}))\left[F_D(\mathbf{x}) + \mu\,\mathrm{div}\left(\dfrac{\nabla\phi(\mathbf{x})}{|\nabla\phi(\mathbf{x})|}\right)\right], \\ F_D(\mathbf{x}) = \int_\Omega B(\mathbf{x},\mathbf{y})\,\delta(\phi(\mathbf{y}))\ln\dfrac{\left[p_1\left(I(\mathbf{x});\hat{\theta}_1(y_1)\right)\right]^{\lambda_1}}{\left[p_2\left(I(\mathbf{x});\hat{\theta}_2(y_1)\right)\right]^{\lambda_2}}d\mathbf{y}.\end{cases} \tag{5.13}$$

Therefore, the evolution equations (5.7) and (5.13) are different in such a way that the intensities I and parameters $(\hat{\theta}_1, \hat{\theta}_2)$ are fixed or vary when computing $F_D(\mathbf{x})$. Specifically, during the computation of $F_D(\mathbf{x})$, in Eq. (5.7), the parameters $\hat{\theta}_1(x_1), \hat{\theta}_2(x_1)$ are fixed, and $I(\mathbf{y})$ scans the values of the intensity within the local region identified by $B(\mathbf{x},\mathbf{y})\,\delta(\phi(\mathbf{y})) > 0$. In contrast, in Eq. (5.13), the intensity $I(\mathbf{x})$ is fixed and the parameters $\hat{\theta}_1(y_1), \hat{\theta}_2(y_1)$ vary as in Chapter 4 (Eq. (4.4)).

To illustrate these differences, we simplify the evolution equations by assuming that data follow a Gaussian statistics, and that weighting parameters and regularization term are discarded. Therefore, the Lankton's style evolution equation (Eq. (5.7)) can be rewritten:

$$\begin{cases}\dfrac{\partial\phi}{\partial t}(\mathbf{x}) = \delta(\phi(\mathbf{x}))\int_\Omega B(\mathbf{x},\mathbf{y})\,\delta(\phi(\mathbf{y}))\,F_1(\mathbf{y})\,d\mathbf{y}, \\ F_1(\mathbf{y}) = \left[(I(\mathbf{y})-m_2(x_1))^2 - (I(\mathbf{y})-m_1(x_1))^2\right],\end{cases} \tag{5.14}$$

and the log-likelihood style evolution equation (Eq. (5.13)) becomes:

$$\begin{cases}\dfrac{\partial\phi}{\partial t}(\mathbf{x}) = \delta(\phi(\mathbf{x}))\int_\Omega B(\mathbf{x},\mathbf{y})\,\delta(\phi(\mathbf{y}))\,F_2(\mathbf{y})\,d\mathbf{y}, \\ F_2(\mathbf{y}) = \left[(I(\mathbf{x})-m_2(y_1))^2 - (I(\mathbf{x})-m_1(y_1))^2\right],\end{cases} \tag{5.15}$$

where $m_1(x_1)$ (resp. $m_2(x_1)$) are the mean intensities of the intersections of the transverse slice $B_{T,x1}$ and the membership functions $M_1(\phi)$(resp. $M_2(\phi)$).

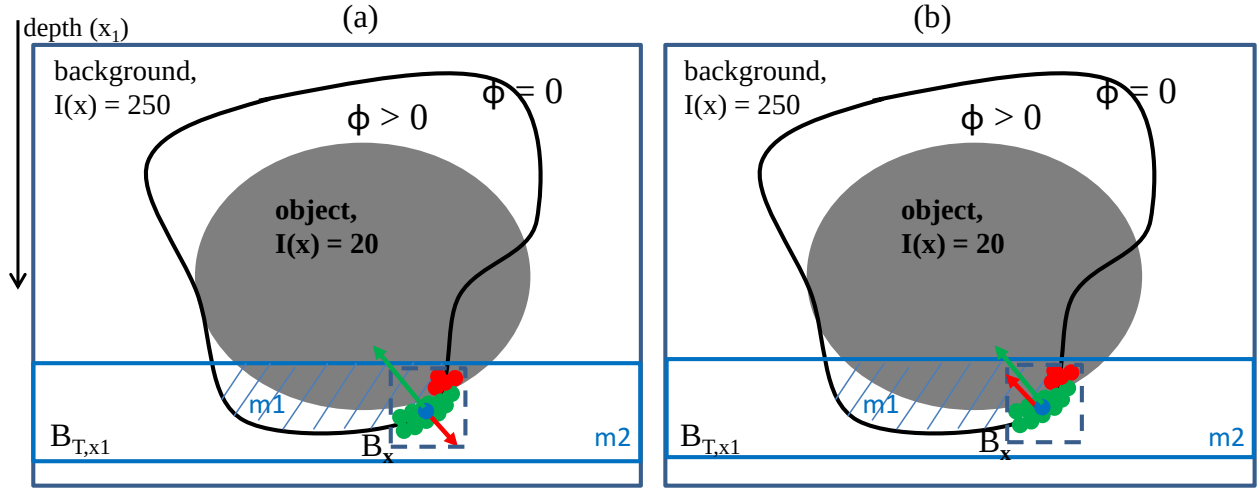

Figure 5.8: Illustration of the differences between the evolution equations (5.14) and (5.15). The gray object with intensity of 20 is surrounded by a white background with intensity of 250. At a specific point $\mathbf{x}$ in blue, the transverse slice B_{T,x_1} is delimited by the blue rectangular border, whereas the small region $B_{\mathbf{x}}$ is delimited by the small dashed rectangular border. Within a small region $B_{\mathbf{x}}$ and close to the zero-level set, the green points belong to the sought background, whereas the red points belong to the sought object. For point $\mathbf{x}$, the green and red arrows represent the direction of the forces that the green and red points affect the zero-level set $\phi(\mathbf{x}) = 0$. (a) Lankton's evolution equation (5.14). (b) Evolution equation (5.15) derived from log-likelihood of the regions.

In the example image shown in Fig. 5.8, the intensities of the object and background are 20 and 250, respectively. The current level-set function ϕ separates the image into the object ($\phi > 0$) and the background ($\phi < 0$). If $\frac{\partial \phi}{\partial t} > 0$, the zero-level set that is expected to delimit the object inflates. Conversely, if $\frac{\partial \phi}{\partial t} < 0$, the curve $\phi = 0$ deflates. Let us consider the sought-background point $\mathbf{x}$ in blue. At $\mathbf{x}$, the level-set function has to shrink to be close to the sought object. We now evaluate how each of the two evolution equations behaves.

Considering Eq. (5.14), at pixel $\mathbf{x}$ (blue color point in Fig. 5.8(a)), $m_2(x_1) \approx 250$, and $m_1(x_1) \approx 80$, the intensity $I(\mathbf{y})$ varies over the local regions closed to the zero level of ϕ because of the presence of $B(\mathbf{x},\mathbf{y})\,\delta(\phi(\mathbf{y}))$. Let consider the green points in Fig. 5.8(a), they belongs to the sought background, so their intensity is 250. Using Eq. (5.14) to compute $F_1(\mathbf{y})$, we obtain $F_1(\mathbf{y}) < 0$ for each of these points, meaning that green points tend to locally deflate the zero-level set (i.e., correct direction). This is represented by the green arrow at $\mathbf{x}$ in Fig. 5.8(a). Considering the red points which belong to the sought object, their intensity is 20. For each of those points, we obtain $F_1(\mathbf{y}) > 0$, meaning that they tend to inflate the zero-level set (i.e., incorrect direction). This is represented by the red arrow in Fig. 5.8(a). Therefore, within local regions specified by

$B(\mathbf{x},\mathbf{y})\,\delta(\phi(\mathbf{y}))$, the points belonging to the sought object (red points) compete with the ones belonging the sought background (green points) during the evolution of the zero-level set. Consequently, using the evolution equation (5.14), the size of $B_{\mathbf{x}}$ should be small to minimize the number of points (i.e., red points in our example) that have incorrect contribution to the evolution of ϕ.

Considering Eq. (5.15), at the same point $\mathbf{x}$, the intensity value $I(\mathbf{x})$ is fixed and equal to 250 (i.e., $I(\mathbf{x}) = 250$); whereas the means $m_1(y_1)$, $m_2(y_1)$ vary. For the green points, the associated mean intensities vary with the center of the transverse slices B_T but can be approximated by $m_2(y_1) \approx 250$, $m_1(y_1) \approx 100$ as shown in Fig. 5.8(b). Using Eq. (5.15), we thus obtain $F_2(\mathbf{y}) < 0$ for those points, meaning that the green points tend to locally deflate the zero-level set. Let consider again the red points, the mean intensities associated with them are: $m_2(y_1) \approx 250$, $m_1(y_1) \approx 30$. We thus obtain $F_2(\mathbf{y}) < 0$ for these red points, so they also correctly contribute to locally deflating the zero-level set. The contributions of the red and green points to the evolution of the zero-level set at $\mathbf{x}$ are represented by the red and green arrows in Fig. 5.8(b). Because points belonging to the sought object and sought background make proper contributions to the evolution of ϕ, the level-set function ϕ is expected to converge faster than the one in Eq. (5.14), and the size of $B_{\mathbf{x}}$ can be large.

From the above analysis, the computations of the image criterion (i.e., whether based on data log-likelihood or not) will lead to different evolution equations that in turn affect the behaviors of the level-set functions. The evolution equations become less different when the size of $B_{\mathbf{x}}$ gets smaller. In special case, when $B_{\mathbf{x}}$ is so small that the size of the local region specified by $B(\mathbf{x},\mathbf{y})\,\delta(\phi(\mathbf{y}))$ is 1 point, both evolution equations are similar. From a practical point of view, when using Lankton's style Eq. (5.7), the size of $B_{\mathbf{x}}$ should be small to maintain low computational cost and better behavior of the level-set function (i.e., containing fewer points that have opposite effects on the evolution of the level-set function). But if $B_{\mathbf{x}}$ is too small, the method will not handle well strong noise. In our work, the size of $B_{\mathbf{x}}$ is empirically set to $3 \times 3 \times 3$ voxels around $\mathbf{x}$. Note that in the original implementation provided by Lankton[2], the size of $B_{\mathbf{x}}$ (or $B(\mathbf{x},\mathbf{y})\,\delta(\phi(\mathbf{y}))$) is 1 point. The evolution equation (5.13) derived from the data log-likelihood is likely to converge faster than Eq. (5.7) because all points within $B_{\mathbf{x}}$ properly contribute to the evolution of the level-set function. The size of $B_{\mathbf{x}}$ may be important, especially for rather small B_T. In our context of large B_T, parameter maps vary slowly so a small $B_{\mathbf{x}}$ is probably more appropriate. If $B_{\mathbf{x}} = B_T$, we reach the solution developed in Chapter 4 except that the evolution here is more local. The evaluation of this evolution

[2] http://www.shawnlankton.com/2008/04/active-contour-matlab-code-demo/

equation on our dataset is ongoing.

5.6 Conclusions

In conclusion, we designed and implemented a STS-LS segmentation method that deals with speckle noise and handles inhomogeneity in the LN envelope echo-signal data. The STS-LS method provided accurate segmentation results and also outperformed the $\text{Seg}_{\text{Lankton}}$ and $\text{Seg}_{\text{Global}}$ methods when applied to our data sets. This new automatic segmentation method can facilitate and expedite accurate QUS-based cancer detection in LNs without the need for operator-dependent segmentation. Therefore, this advance can enable more-efficient QUS-based cancer detection in LNs.

Future refinements to the technique could be developed to further improve segmentation. For example, because the STS-LS method is based on local statistics, it is sensitive to initialization. The closer the initialization is to the true boundaries, the faster the segmentation will converge. Additional work developing more-effective initialization technique could significantly improve the efficiency of the STS-LS method. We also note that an additional strategy is available to extend the two-phase segmentation to multiphase segmentation based on the idea of competing regions proposed by T. Brox [124], and it potentially can be applied to the STS-LS method. We consider investigation of these options to be the subject of future work. In addition, other techniques are needed to identify regions subject to strong localized shadowing effects. Currently, such shadowing can compromise the STS-LS segmentation, which assumes that data are relatively homogeneous within each transverse slice. The investigation of a machine-learning based approach for better initialization of the STS-LS segmentation method is the subject of the next chapter.

Chapter 6

Segmentation with a Machine Learning Technique[1]

6.1 Introduction

The two proposed segmentation methods (LRGDF and STS-LS) presented in Chapters 4 and 5 provided satisfactory segmentation results on our LN envelope data. The success of the methods was based on the use of the level-set framework and parametric modeling (i.e., gamma probability density function) of speckle statistics in local regions specified by membership functions and the mollifying kernels or transverse slices. Nevertheless, how to improve the computational efficiency of the methods while still maintaining their high segmentation accuracy. Because both methods require initialization, the closer the initialization is to the sought boundaries, the faster the segmentation will converge, thus reducing the execution time. Therefore, better initializations greatly contribute to improving the efficiency of the LRGDF and STS-LS methods.

As presented in Chapter 2, we have acquired a large dataset with 445 LNs from 169 colorectal-cancer patients and 418 LNs from 119 breast-cancer patients, and many of them were manually segmented by experts. Furthermore, the LRGDF and STS-LS methods provided almost perfect segmentation results in several LNs that could be potentially considered to be labeled data. These raise questions that how we can integrate the information of many correctly segmented LNs (i.e., many labeled LNs) into segmenting an upcoming LN data, and that how we can apply the experience of correctly segmenting previous LNs to segmentation of subsequent LNs. The feasible solution is to use machine learning techniques in a supervised fashion. As defined by Ethem Al-

[1]This chapter is adapted from Thanh M. Bui, Alain Coron, Jonathan Mamou, Emi Saegusa-Beecroft, Eugene Yanagihara, Junji Machi, S. Lori Bridal, and Ernest J. Feleppa, "Random Forest Classification and Local Region-Based, Level-Set Segmentation for Quantitative Ultrasound of Human Lymph Nodes", IEEE International Ultrasonics Symposium (IUS), Taipei, Taiwan, pp. 1-4, 2015. [125]

paydin, machine learning is "programming computers to optimize a performance criterion using example data or past experience" [126]. Supervised learning is a machine learning task of estimating an unknown (input, output) mapping from known (input, output) examples that are usually called labeled training data [127].

Random forests [128] that are ensembles of randomly trained decision trees have been empirically demonstrated to outperform other state-of-the-art machine learning techniques when applied to high dimensional data [129]. The learning framework can handle a large amount of training data efficiently, inherently suit for multi-class problems (e.g., simultaneous segmentation of different tissues) and are easily distributed on parallel-hardware architectures (easily parallelizable) [130–132]. Random forests have been well adapted to classification, regression and other problems [132]. In the classification problems of 3D data, when the number of labeled voxels is large, the computational efficiency of random forests is essential to significantly reduce the execution time required for training and classifying.

Random forest classification (RFC) has been successfully applied to medical image segmentation [133–135]. Lempitsky et al. [133] employed RFC to segment the myocardium in 3D echocardiography data automatically. For each voxel, the features including appearance (a sum of intensities within a cuboid centered at the voxel) and position were considered. Recently, Yaqub et al. [135] described two extensions to the traditional random forest framework and demonstrated that the extended framework outperformed the traditional framework as well as many state-of-the-art techniques on segmenting adult brain magnetic resonance imaging and 3D fetal femoral ultrasound datasets. Their extensions involved introducing a feature selection step to retain strong features and neglect weak features, and weighting each tree in the forest in the classification (testing) phase.

Contribution to researches on random forests could be carried out in two manners. On the one hand, efforts have been made to propose improvements in the random forest model itself [131, 135–137]. These contributions could be evaluated using standard databases such as Kinect body part classification [138], ImageNet [139], Caltech Pedestrian Dataset [140], etc. On the other hand, researchers could propose new discriminative features [133, 138, 141] and incorporate them into a traditional random forest framework to achieve their goals (e.g., realtime, accuracy, etc.) for a specific application. Our contribution in this chapter can be categorized as the latter.

To segment the LN parenchyma (LNP), perinodal fat (PNF) and normal saline (NS) media in LN

envelope data, we investigate RFC to obtain preliminary segmentation results to initialize level-set methods automatically. The RFC makes use of features consisting of backscattered energy, statistical parameters, contextual information and distance information. To obtain more efficient segmentation results, the results provided by the RFC were used to initialize the LRGDF and STS-LS methods, yielding two new segmentation methods namely RFC_LRGDF and RFC_STS-LS. The RFC_LRGDF and RFC_STS-LS methods call upon the level-set methods to correct for spatially-inconsistent misclassifications of the RFC and to account for the variability of ultrasound statistical properties associated with focusing and attenuation effects.

6.2 Methods

6.2.1 Segmentation using Random Forest Classification

To fix the coordinate system, $\vec{x_1}$ is the axis parallel to the ultrasound beam, while $\vec{x_2}$ and $\vec{x_3}$ are orthogonal axes lying in a plane perpendicular to the beam direction. $I(\mathbf{x})$ is the acquired 3D ultrasound envelope data at position $\mathbf{x} = (x_1, x_2, x_3)$.

6.2.1.1 Features

The initial segmentation is formulated as a 3-class classification of voxels. For each voxel V^i, fifteen features were extracted for training and classification as presented in Table 6.1. The backscattered energy corresponds to the amount of energy that has been backscattered. Distance information, consisting of distance to the transducer and the length of the acquisition along the axial direction, takes into account the voxel position and the LN size information. The contextual information becomes important to discriminate voxels belonging to LNP from ones belonging to NS, especially at distant parts of the LN data where the signals are highly attenuated. Finally, because the envelope data were well modeled by the gamma distribution which is not a symmetric distribution, the shape and scale parameters as well as average and median can be considered to be good statistical features. To compute these statistical features, two sizes of cubic region of interest (i.e. lengths of 0.3 mm and 0.5 mm) were used to take into account data properties in different spatial scales. Note that apart from distance features (i.e., x_1 and acquisition length), we replaced the original values of other features by their natural logarithm.

Table 6.1: Description of the 15 features extracted for each voxel located at $\mathbf{x} = (x_1, x_2, x_3)$.

Category	Description
Backscattered energy	$BE(\mathbf{x}) = \int_0^{x_1} I^2(u, x_2, x_3)\, du$ provides information about tissues that the ultrasound beam has propagated through.
Distance information	x_1, distance to transducer. Length of the acquisition along $\overrightarrow{x_1}$.
Contextual information	The four maximum intensities along the four rays, with an origin at the center of the voxel of interest, radiating outward along the $\vec{x_2}$ or $\vec{x_3}$ axes. For example, $CI\_x2- = \max_{-\infty \leq u < x_2} I(x_1, u, x_3)$, $CI\_x2+ = \max_{x_2 < u \leq \infty} I(x_1, u, x_3)$.
Statistical parameters	Four features were estimated within each cubic region of interest (ROI) centered on each voxel. 2 ROIs (edge length of 0.3 mm or 0.5 mm) were extracted around each voxel $\mathbf{x}$. The four parameters are: • shape and scale parameters of the gamma distribution that best models the empirical distribution of I; • average and median of I.

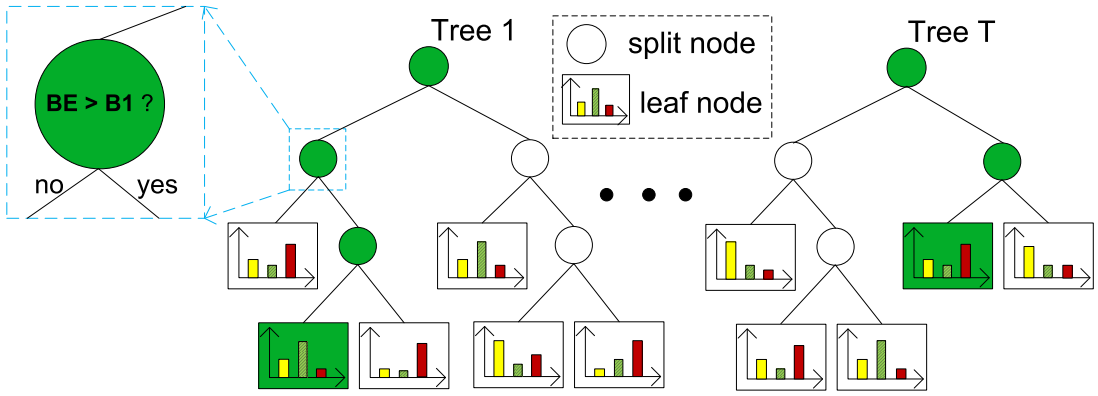

Figure 6.1: Diagram of classification forest using 3 classes (LNP, fat and NS). A forest contains T trees. After training, each split node stores a binary test, while each leaf node stores a class distribution. The enlarged split node illustrates how the binary test is carried out by applying the threshold (B1) for the feature (BE, backscattered energy) that was selected for this node during training. A feature vector is classified by traversing each tree and is sent to the left or right child node depending on its response to the binary test at each split node. This process gives a path from root to leaf (as illustrated in green) and a class distribution at the leaf node.

6.2.1.2 Training the Random Forest

As illustrated in Fig. 6.1, random forest [128, 132] is an ensemble of decision trees; each tree consists of split nodes and terminal nodes. By merging the decisions of all trees, this ensemble has higher accuracy than a single tree. The RFC can be separated into an off-line phase (training) and on-line phase (classification). As we use the RFC to classify voxels in a supervised setting, in the training step, the classifier is trained using a collection of N labeled voxels, $V = \left\{(\mathbf{f}^i, c^i)_{i=1}^N\right\}$, where $\mathbf{f}^i$ is the feature vector including the 15 elements of the i-th training voxel, and $c^i \in \{1,2,3\}$ corresponding to LNP, PNF and NS media, respectively, is its class label provided by an expert.

The training phase is responsible for building T random decision trees. A decision tree is a graph with no loops consisting of split nodes and terminal nodes as shown in Fig. 6.1. To build each tree, a small random subset $V' \subseteq V$ of the original labeled voxels V is used. By using the subset V', each tree is grown by repeating the following steps at each split node:

1. Randomly select m features from the full feature set ($m = 4$ features from a full feature set containing 15 features, in our case).

2. Find the feature among these m features that provides the maximum information gain at its optimized threshold. The information gain that reflects the quality of a split (i.e., it measures how a binary test successfully splits the labeled voxels of different classes into different child nodes) is computed using the Gini index as follows:

$$\triangle G(V_n, n) = Gini(V_i, n) - w^l Gini\left(V_{nl}, n^l\right) - w^r Gini(V_{nr}, n^r), \tag{6.1}$$

   where V_n is the labeled voxels at node n; w^l and w^r are the proportion of the labeled voxels at node n assigned to the left n^l and right n^r child nodes. The Gini index at split node n, $Gini(n)$, is computed by:

$$Gini(n) = \sum_{k=1}^{3} p_k^n (1 - p_k^n), \tag{6.2}$$

   where p_k^n is the proportion of labeled voxels belonging to class k at node n.

3. Split the training labeled voxels at the node into two child subsets according to the threshold level for the node's feature.

This process is repeated to split nodes until either the number of training labeled voxels at the

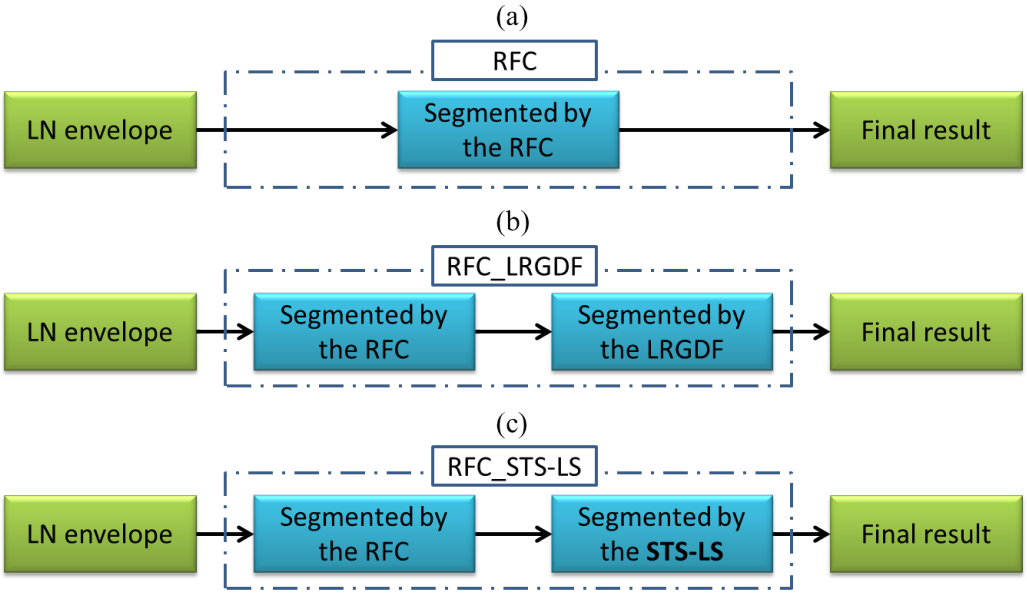

Figure 6.2: RFC (a) and segmentation methods (b, c) obtained by combining RFC with the LRGDF and STS-LS methods

node falls below a certain threshold or no gain of information is achieved if training labeled voxels are split to left and right subsets. The feature and thresholds selected for each node and the tree architecture are stored for use during subsequent classification. A node where the split does not take place is called a leaf (or terminal) node. After finishing the training, T trees are created. Each node in any tree contains a weak classifier (i.e., a feature and optimized threshold). Each leaf node contains a distribution (histogram) of training class labels that reach it.

6.2.1.3 Classifying with the Random Forest

As shown in Fig. 6.1, during classification, each feature vector traverses each tree separately until, for each tree, a leaf node is reached. At each split node, the feature vector is sent to the left or right child node depending on the result of the binary test associated with the node and chosen during training. The class distributions (calculated during training) of reached leaf nodes of all trees are combined to provide the final probabilistic output. The class of maximum probability is chosen to label the feature vector and the corresponding voxel within the data set.

6.2.2 Final Segmentation

The RFC was applied to the segmentation of the three media in the LN envelope data. The segmentation results of the RFC were evaluated and were used as an initialization for the LRGDF and STS-LS methods. The RFC and its combination with the two level-set methods yield 3 new segmentation methods, namely RFC, RFC_LRGDF and RFC_STS-LS as shown in Fig. 6.2.

6.2.3 Parameter Settings and Evaluation Methods

We used an RFC of 60 trees ($T = 60$). During the training, among 15 features, 4 features were randomly selected to be evaluated at each split node. The minimum size of a leaf node was set as 1. To train each tree, two-thirds of the original training labeled voxels were randomly selected. From a database of 54 LNs (18 metastatic, 36 non-metastatic) acquired from colorectal-cancer patients, 12 LNs (6 metastatic, 6 non-metastatic) were selected for training the RFC, and the 42 remaining LNs were used to evaluate the RFC and then the RFC_LRGDF and RFC_STS-LS methods. Using the RFC_LRGDF and RFC_STS-LS methods, the parameter settings for the LRGDF and STS-LS methods were similar to those presented in Chapter 4 and 5, except that the number of iterations for the two methods was set to 80.

In implementing and evaluating the RFC method, it is necessary to know which features play more important roles than others, so that we can optimize the method afterwards. Therefore, the feature importance was computed by the summation of the decreases in the information gain at each split node for each individual feature over all the trees.

Similar to Chapters 4 and 5, the success of segmentation methods was quantified using the Dice similarity coefficient (DSC) to compare the automatic and expert manual segmentations. Furthermore, we also evaluated the segmentation method in terms of QUS estimates from automatically segmented LNs and manually segmented LNs using a Bland-Altman plot [142].

6.2.4 Statistical Test

In addition to two segmentation methods (LRGDF and STS-LS) presented in Chapters 4 and 5, we have described three new methods (i.e., RFC, RFC_LRGDF and RFC_STS-LS) in this chapter. It is important to identify which method performs better than others on our dataset. Therefore, we

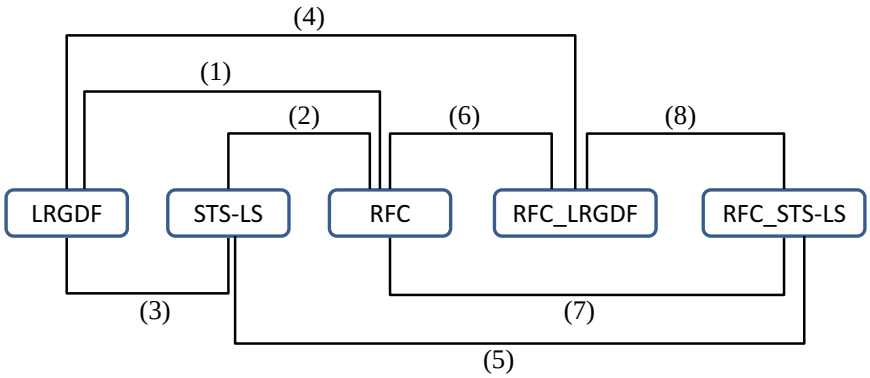

Figure 6.3: Eight pairs of methods that were applied Wilcoxon paired, signed-rank tests. The numbers correspond to the questions that we wanted to answer.

compared DSC values obtained from the five methods when segmenting each of three media (i.e., LNP, PNF and NS). The Friedman's test was carried out to identify statistically significant difference in the DSC values depending on the segmentation methods. The non-parametric Friedman's test was used because it does not assume normality of the data distributions. More importantly, we also wanted to answer to the following 8 questions:

1. How does the RFC perform as compared to the LRGDF method?
2. How does the RFC perform as compared to the STS-LS method?
3. How is the performance of the LRGDF method in comparison with that of the STS-LS method?
4. Are the segmentation results of LRGDF method improved when the ellipsoid-based initialization is replaced by the RFC initialization?
5. Are the segmentation results of STS-LS method improved when the ellipsoid-based initialization is replaced by the RFC initialization?
6. Does the LRGDF method improve the RFC segmentation?
7. Does the STS-LS method improve the RFC segmentation?
8. Between LRGDF and STS-LS methods, which one is better at refining the RFC segmentation?

To respond to these questions, Wilcoxon paired, signed rank tests were carried out to compare eight pairs of methods as illustrated in Fig. 6.3. By taking into account the Bonferroni correction [123], the significance level for the paired tests was set at $\alpha = 0.05/8 = 0.006$.

Table 6.2: The DSC (MEAN±STD) of the initial segmentation using the RFC in comparison with other four segmentation methods over 42 LNs.

Media	LRGDF	STS-LS	RFC	RFC_LRGDF	RFC_STS-LS
LNP	0.927 ± 0.035	0.937 ± 0.025	0.922 ± 0.022	0.942 ± 0.028	0.936 ± 0.020
PNF	0.814 ± 0.104	0.822 ± 0.088	0.801 ± 0.074	0.841 ± 0.099	0.820 ± 0.079
NS	0.976 ± 0.009	0.963 ± 0.008	0.959 ± 0.013	0.976 ± 0.008	0.961 ± 0.009

6.3 Results

For each medium, the Friedman's test indicated statistically significant differences in the DSC values depending on the segmentation methods (p values less than 10^{-7} for the three media of 42 LNs).

6.3.1 Segmentation with RFC, LRGDF and STS-LS Methods

Table 6.2 summarizes the DSC values provided by the five segmentation methods on 42 LNs. As indicated by Table 6.2, the DSC values provided by the RFC method are relatively high but they are lower than the those provided by LRGDF and STS-LS methods. Specifically, the DSC values for LNP and PNF of the RFC segmentation are significantly smaller than those of the STS-LS method as indicated in Fig. 6.4; DSC values for NS of the RFC method are significantly smaller than that of the LRGDF method.

Visual examination of the segmentation results allows us to identify the reason why the RFC method did not perform well enough. As shown in Fig. 6.5(b), RFC does not produce smooth segmentation. This is due to the fact that RFC classifies each voxel independently. Furthermore, spatially inconsistent misclassifications can occur as indicated in Fig. 6.6(b).

Fig. 6.7 presents feature importance based on the information gain computed using the Gini splitting index. The backscattered energy proves to be the most important feature for RFC. Additionally, the larger cubic ROIs provided more important statistical features (shape, scale, median, average) than the smaller cubic ROIs.

Although the DSC values for LNP and PNF of the STS-LS method are slightly higher than those of the LRGDF method as indicated in Table 6.2, no statistical difference in their DSC values was found using the Wilcoxon paired, signed-ranked test (Fig. 6.4). Table 6.2 and Fig. 6.4 indicate that the LRGDF method provided statistically higher DSC values for NS medium than the STS-LS

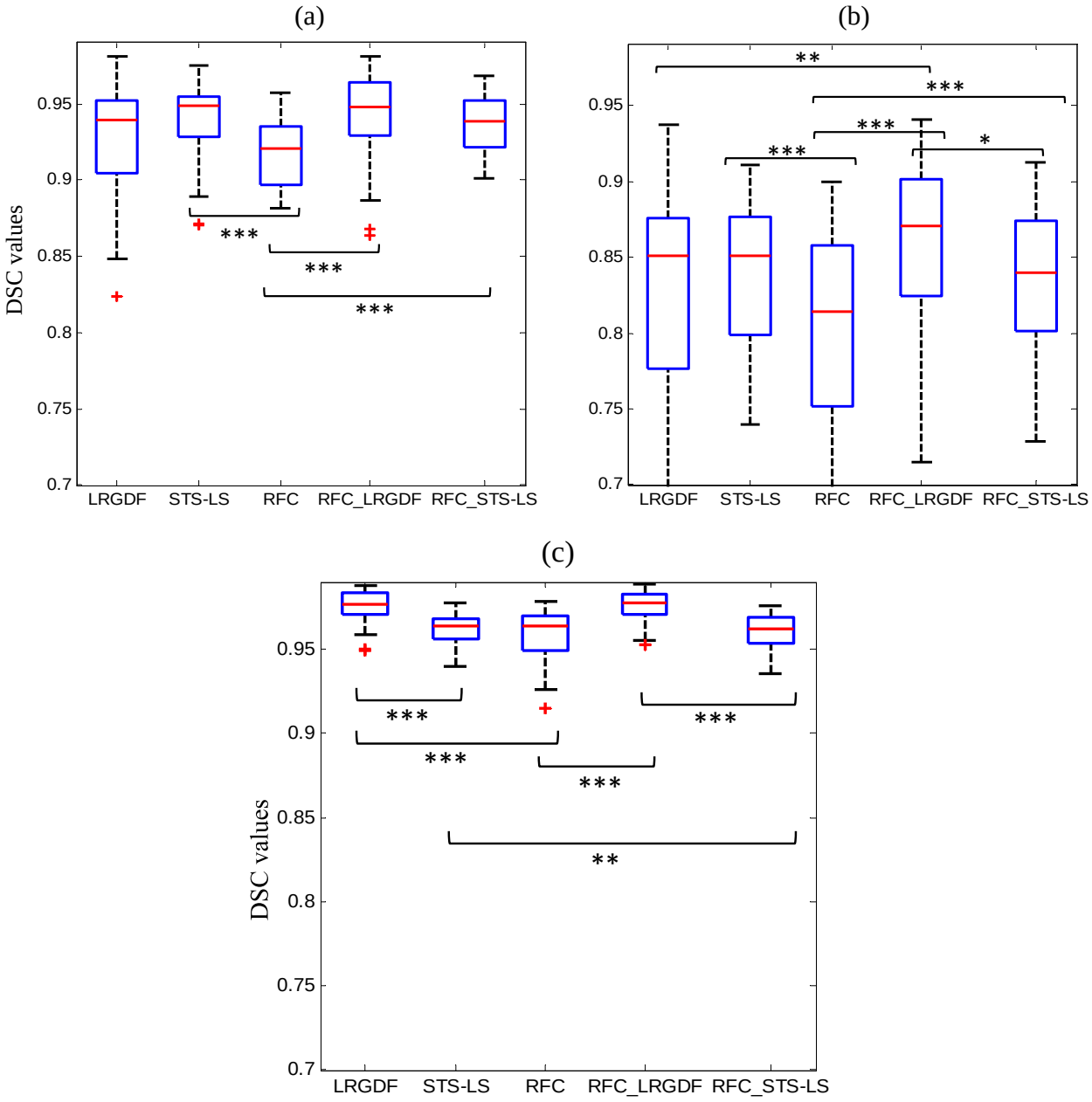

Figure 6.4: Boxplots showing the distributions of DSC values obtained from each of the 5 segmentation methods for the 3 media in 42 LNs. (a) LNP; (b) PNF; (c) NS. The asterisks *, ** and *** indicate the p values estimated according to the Wilcoxon paired, signed-rank test lower than the adjusted (i.e., Bonferroni correction) significance levels $\alpha = 0.006$, $\alpha/5$ and $\alpha/50$, respectively.

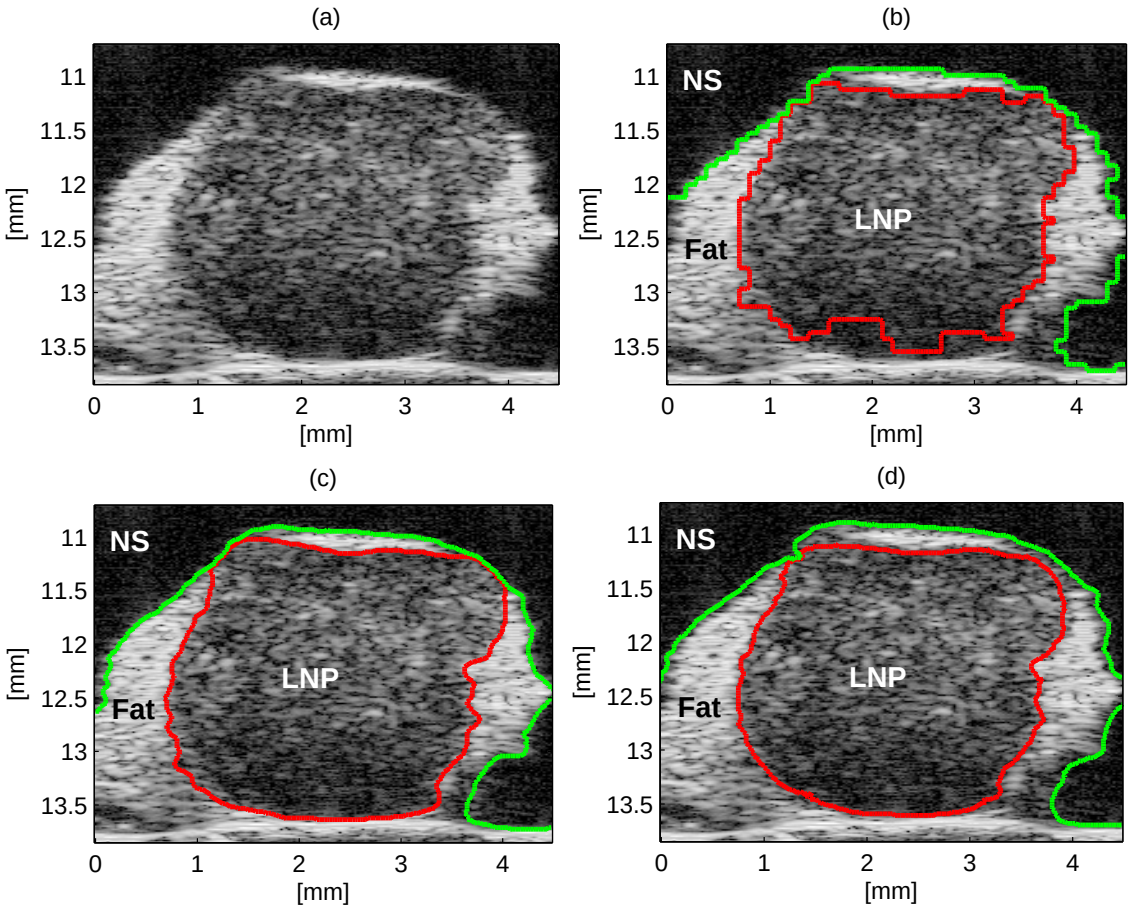

Figure 6.5: A representative segmentation result obtained from a nonmetastatic LN overlaid on the log-compressed B-mode image (40 dB dynamic range). Original B-mode image (a); segmentations using the RFC (b), the RFC_LRGDF (c) and the RFC_STS-LS (d) methods. The DSC values of the RFC_STS-LS segmentation were 0.934, 0.843 and 0.948 for LNP, PNF and NS, respectively.

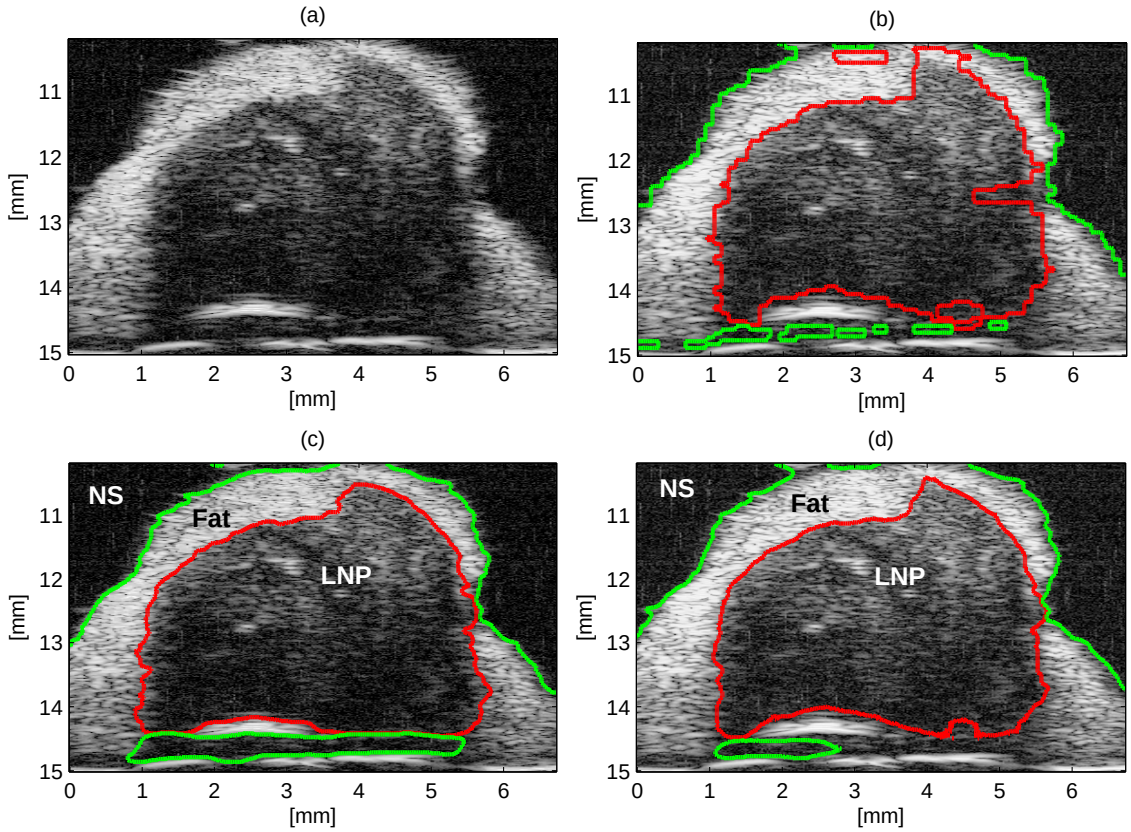

Figure 6.6: Segmentations of a metastatistic LN overlaid on the B-mode image. Original B-mode image (a); segmentations using the RFC (b), the RFC_LRGDF (c) and the RFC_STS-LS (d) methods. The DSC values of the refined segmentation were 0.951, 0.871 and 0.965 for LNP, PNF and NS, respectively.

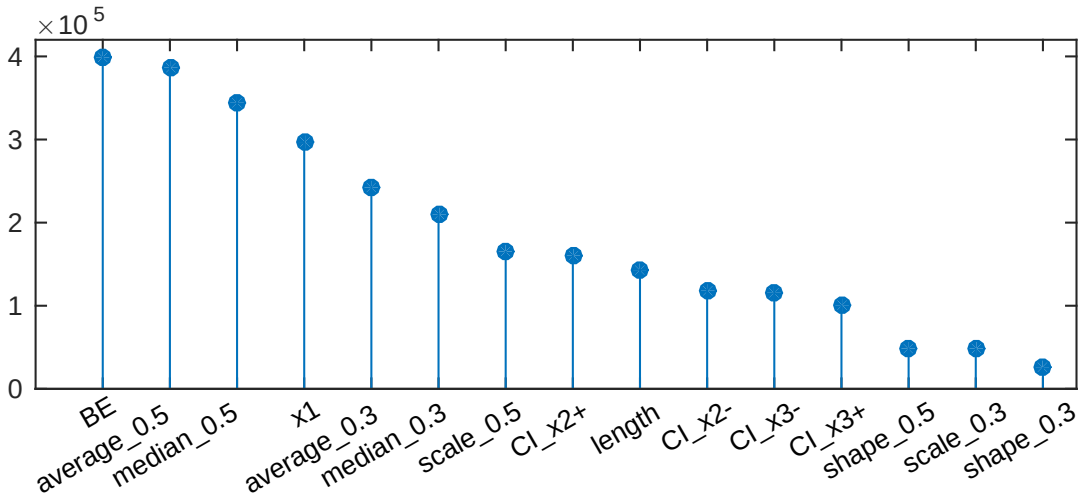

Figure 6.7: Feature importance based on the Gini splitting index. The larger the score, the more important the feature. 0.3 or 0.5 at the end of a feature name indicates the size of the cubic ROI.

method.

6.3.2 Refining the RFC Segmentation

For segmenting LNP and PNF media, the RFC_LRGDF and RFC_STS-LS methods provided statistically significantly better DSC values than the RFC method because the level-set methods (i.e., LRGDF and STS-LS methods within the RFC_LRGDF and RFC_STS-LS methods) smoothed the segmentation boundaries and corrected some spatially inconsistent segmentation provided by the RFC segmentation as shown in Fig. 6.5(c,d) and 6.6(c,d). As can be seen in Fig. 6.6(c,d), the bottom of the LN is not perfectly segmented, however this does not affect the QUS processing because QUS parameters are only estimated in the more supercial data for depths from 10.5 mm to 13.5 mm [2]. Importantly, because the LRGDF method took into account speckle statistics in local regions specified with mollifying kernels, it is very effective in refining the RFC initialization that is close to the sought boundaries. This is demonstrated by the fact that for segmenting the three media, the RFC_LRGDF method provided highest DSC values (Table 6.2) that are statistically significantly higher than those provided by the RFC method (Fig. 6.4); whereas the RFC_STS-LS method produced statistically significantly better DSC values for two media (i.e., LNP and PNF) in comparison with the RFC method. In order to refine the RFC initialization, the LRGDF method is therefore preferable to the STS-LS method.

6.3.3 Segmentation Time

In terms of segmentation time, the RFC method took much less time to obtain the final segmentation results compared to other methods as shown in Table 6.3. Note that using the RFC method, significant time was required for feature extraction, while the classification only took a few seconds. The RFC_LRGDF and RFC_STS-LS methods provided comparable segmentation time which is about half of the segmentation time required by the STS-LS method. Note that the segmentation methods were implemented in Matlab 7.12 (R2011a) without code optimization in mind and evaluated on a desktop computer with the Intel® Xeon(R) CPU E5-2643 at 3.3GHz.

Table 6.3: Execution time (MEAN±STD) in minutes over 42 colorectal LNs.

LRGDF	STS-LS	RFC	RFC_LRGDF	RFC_STS-LS
33.8 ± 20.2	20.8 ± 14.5	2.6 ± 1.7	10.2 ± 5.7	10.6 ± 6.3

6.3.4 Quantitative Ultrasound Evaluation using Automatic and Manual Segmentation

In general, QUS parameters obtained from LNs segmented using RFC, RFC_LRGDF and RFC_STS-LS methods were very close to those obtained from manually segmented LNs. We present here the Bland-Altman plots for the average-effective-scatterer size, D, and the average-acoustic concentration, C, because they are important estimates in characterizing metastatic and non-metastatic colorectal LNs as indicated in previous work [1, 2].

As indicated in Fig. 6.8, the D estimates made in LNP segmented with the automatic methods vs. manual segmentation by an expert agreed well. The mean differences and the 95% limits of agreement (MEAN±1.96*STD) for the RFC vs. manual segmentation, RFC_LRGDF vs. manual segmentation and RFC_STS-LS vs. manual segmentation were -0.02 μm and $[-1.37, 1.32]$ μm, -0.11 μm and $[-1.03, 0.81]$ μm, and -0.12 μm and $[-0.92, 1.16]$ μm, respectively. Therefore, the D values estimated from LNs segmented by the RFC_LRGDF method are closest to those obtained from manually segmented LNs.

Fig. 6.9 presents the Bland-Altman plot for the C values estimated from LNs segmented by automatic methods vs. manual expert. The mean differences and the 95% limits of agreement (MEAN±1.96*STD) for the RFC vs. manual segmentation, RFC_LRGDF vs. manual segmentation and RFC_STS-LS vs. manual segmentation were -0.39 dB/mm^3 and $[-1.62, 0.83]$ dB/mm^3, -0.15 dB/mm^3 and $[-0.89, 1.19]$ dB/mm^3, and -0.37 dB/mm^3 and $[-1.53, 0.78]$ dB/mm^3, respectively. Compared to the C values obtained from manually segmented LNs, the RFC_LRGDF method provided closest C values, followed by the RFC_STS-LS method.

6.4 Discussion and Conclusions

In this chapter, three new segmentation methods (i.e., RFC, RFC_LRGDF and RFC_STS-LS) have been described to automatically segment the three media in LN envelope data. Their segmentation accuracy (quantified by the DSC values) and segmentation time were compared. These new

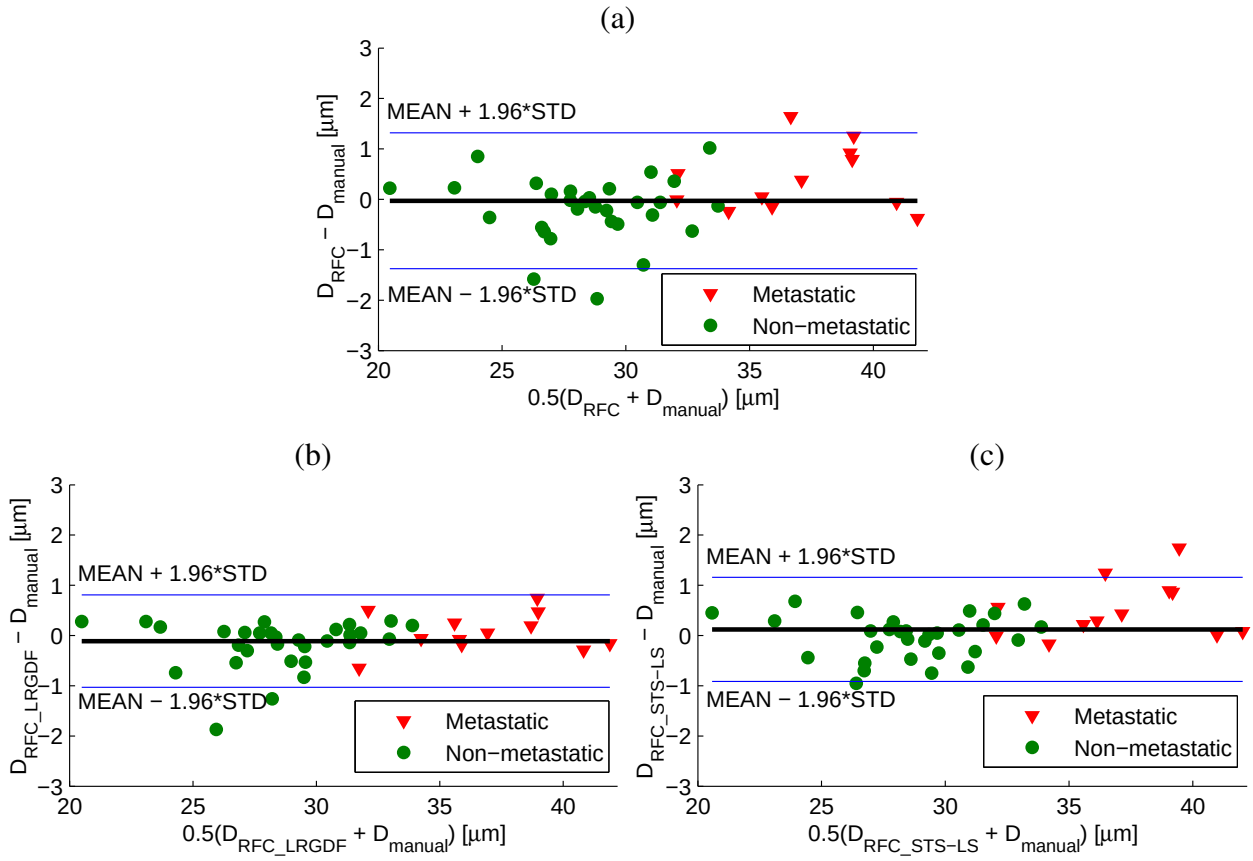

Figure 6.8: Difference vs. the mean for the average-effective-scatterer size (D) estimated on 42 LNs segmented with an expert and each of 3 automatic segmentation methods (i.e., RFC, RFC_LRGDF, RFC_STS-LS).

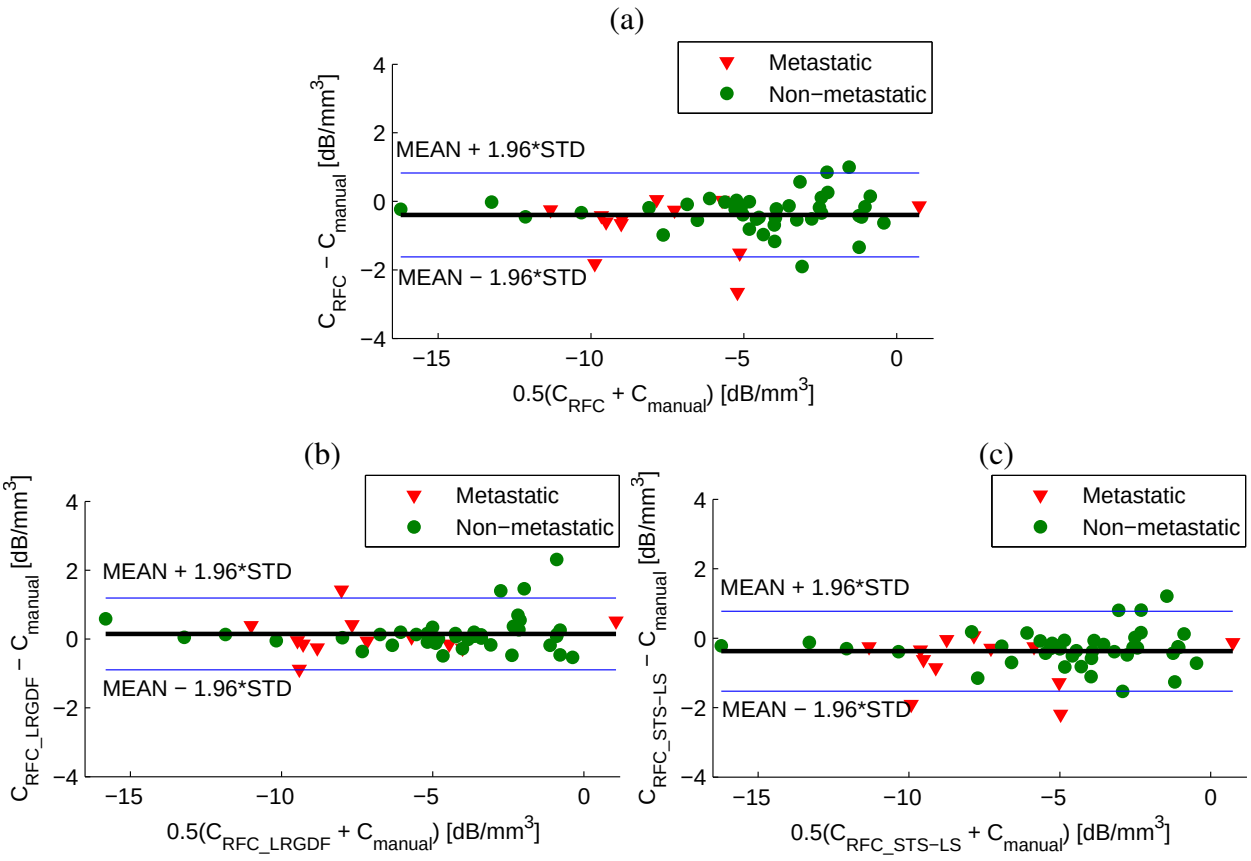

Figure 6.9: Difference vs. the mean for the average-acoustic concentration (C) estimated on 42 LNs segmented with an expert and each of 3 automatic segmentation methods (i.e., RFC, RFC_LRGDF, RFC_STS-LS).

methods were also compared to those obtained by the LRGDF and STS-LS methods as presented in Chapters 4 and 5. In addition, QUS estimates obtained from LNs segmented by the three new methods were evaluated with those obtained from manually segmented LNs.

The RFC method was more computationally efficient than the LRGDF and STS-LS methods and provided relatively accurate segmentation results on our dataset. Furthermore, the backscattered energy was the most important feature in the feature set for the RFC. Note that the RFC method could be improved in several ways. Firstly, the feature sets could be enriched to include texture features computed using the gray-level co-occurrence matrix [143–145] or using local binary patterns [146, 147] or wavelet package texture descriptors [148, 149]. Secondly, the efficiency of RFC method could be improved. Currently the training took about 10 hours to finish, but it was done off-line, while the on-line classification took about a few seconds. Therefore, the time reported in Table 6.3 for the RFC method can be considered to be the time required for extracting features which was implemented using Matlab. Reimplementing the feature extraction process using C/C++ would significantly reduce the execution time for the RFC method. Thirdly, increasing the number of LNs used for training would improve classification accuracy but could increase the time required for training. The online random forest [150, 151] could also be considered to allow online building of decision trees and thus to avoid retraining the classifier from scratch. Finally, the performance of the RFC method is associated with the labeled data used for training the classifier. The labeled data were mostly based on the manual expert segmentation. Therefore, improving the quality of manual segmentation for being used as labeled data would improve the performance of the RFC method.

The combinations of the RFC framework with the level-set methods yield the RFC_LRGDF and RFC_STS-LS segmentation methods. The two new methods are well adapted to high-frequency ultrasound envelope data of soft-tissues whose statistics vary with depth due to focusing and attenuation effects. As being inherent within the level-set framework, the LRGDF and STS-LS methods naturally handled topology changes, therefore they compensated for some local inconsistencies obtained using the RFC. Additionally, the RFC_LRGDF method provided slightly better results in terms of DSC values and QUS parameter estimates as compared to the RFC_STS-LS method (Table 6.2 and Fig. 6.4). This can be explained by the fact that the LRGDF method (within the RFC_LRGDF method) was more effective in refining the segmentation provided by the RFC method because the initialization (provided by the RFC) was very close to the sought boundaries

and the LRGDF method took into account the statistics of data in more-local regions specified by the mollifying kernels.

In conclusion, the RFC_LRGDF and RFC_STS-LS methods provided accurate segmentation results on our data set when compared to manual expert segmentation. In addition, the QUS parameters obtained from the LNs with automatic segmentations were close to those obtained when manual segmentation was used. Therefore, these results demonstrate that these methods can contribute to obtaining accurate QUS estimates in excised colorectal LNs without operator-dependent segmentation.

Chapter 7

Conclusions and Perspectives

7.1 Goals and Results

The main objective of this work was to investigate whether advanced signal and data analysis techniques could enable automatic segmentation of the three media (i.e., LNP, PNF and NS) in LN envelope data. Such automatic segmentation is necessary to fully automate the QUS processing to detect metastases in dissected human LNs.

A preprocessing method based on cubic smoothing splines was developed to restore the saturated radio-frequency signals occurring predominantly in the PNF medium of the LN data. This preprocessing method is important to convert the empirical multi-modal distribution of PNF envelope data into a unimodal distribution. In addition, a study on the statistical modeling of the envelope of LN ultrasound data was conducted. Results indicated that the three-parameter generalized gamma distribution modeled the envelope data of the three media (i.e., LNP, PNF and NS) well. The two-parameter gamma distribution, however, was ultimately selected to model the three media due to its high fitting accuracy, its analytically less-complex probability density function (PDF) expression, and its closed-form expression for parameter estimation using the method of moments.

Two novel level-set segmentation methods (LRGDF and STS-LS) were developed to segment the three media in the LN envelope data. The methods make use of localized gamma statistics of envelope data to handle data inhomogeneities caused by attenuation and focusing effects. The LRGDF method employed the gamma PDFs to model speckle statistics of envelope data in local regions at a controllable scale using a smooth function with a compact support, i.e., the gamma-distribution parameters of the local data are considered as spatially-varying functions. To obtain more efficient segmentation, the STS-LS method used gamma PDFs to locally model the speckle statistics within consecutive transverse slices. Because the data belonging to a same medium and

transverse slice are relatively homogenous, they could be properly described by the same PDF distribution parameters. Therefore, this transverse-slice approach is well adapted to the HFU data that is subject to depth-related inhomogeneities and provided faster segmentation results than the LRGDF method.

Nevertheless, an intrinsic shortcoming of level-set methods based on local statistics is their dependence on initialization. To overcome this problem and to obtain more efficient segmentation results, a method based on RFC with new proposed features was developed to initialize for the LRGDF and STS-LS methods effectively and automatically. The combination of RFC with two level-set methods yielded composite methods referred to as: RFC_LRGDF and RFC_STS-LS.

As compared with manual expert segmentation, the novel methods, especially the RFC_LRGDF method, designed and evaluated in this research provided accurate and automatic segmentation results on simulated envelope data and data acquired for LNs from colorectal-cancer and breast-cancer patients. Results also demonstrated that accurate QUS estimates are maintained when automatic segmentation is applied to evaluate excised LN data. Thus, segmentation techniques designed to account for local ultrasonic speckle statistics should eliminate the need for operator-dependent, manual segmentation for QUS evaluation of human LNs.

7.2 Perspectives

A straightforward extension of the work in this thesis is to evaluate the segmentation methods across the entire LN data set. QUS parameters [2, 4] will be estimated automatically using the automatic segmentation results provided by our methods. The sensitivity, specificity and area under the receiver-operator characteristic curve will then be computed to evaluate the QUS methods for the detection of LN metastases.

Athough occuring predominantly in the PNF, the signal saturation may also occur in the LNP. Therefore, the preprocessing method based on smoothing cubic spline that was developed in this thesis to restore the saturated signals could be helpful for QUS parameters. For example, using spectral analysis of RF signals to quantify the frequency-dependent information of tissues, QUS parameters (e.g., effective scatterer size and acoustic concentration) were estimated from the normalized power spectra (or backscatter coefficient as shown in Fig. 1.6) of the RF signals. Saturation has impacts on the RF signals such as causing the loss of signal power and modifying the

form of signals, and thus changes the frequency-related information of the RF signals.

The segmentation methods provided accurate segmentation results for colorectal LNs as well as a limited number of breast LNs. The segmentation of breast LNs remains challenging because of their irregular shapes and topologies and because significant fat deposits occur within the LNP. Basically, in our dataset, the breast LNs can be devided into three groups. A majority of breast LNs can be categorized in the first group consisting of LNs that are similar to colorectal LNs (i.e., bean-shaped parenchyma surrounded by a thin layer of perinodal fat). The second group contains LNs that are quite similar to the LNs of the first group but contain significant fat within the LNP; LNs may also be elongated along one axis. LNs belonging to the third group are elongated and exhibited irregular topologies, highly echogenic structures; fat may be embedded in the LNP. These LNs are very difficult to segment even by human experts. In addition to axillary LNs, the third group also contains sentinel LNs that were cut in two halfs during the sentinel LN biopsy. The third group is the most challenging group for segmentation.

Methods developed in this thesis provided accurate segmentation results for the first group and good segmentation results for the second group of breast LNs. For the third group of breast LNs, correct segmentation could not be provided by experts, therefore it is not possible to evaluate our segmention methods in this group. To segment LNs in the third group, one idea is to refer to the histology data and use the information of histology data (e.g., shapes, topologies, etc.) to obtain reference segmentation of ultrasound data. If accurate segmentations for data in a number of LNs in this group are be obtained, the reference data can be used to train the RFC. RFC_LRGDF and RFC_STS-LS methods could subsequently be applied to obtain and evaluate segmentation results within an additional set of LNs.

The LRGDF method provided accurate segmentation results on the LN envelope data and B-mode tumor data. The gamma distribution well modeled the envelope data as well as the B-mode data. In addition, use of a mollifying kernel to take into account the local statistics helps the LRGDF method to handle data inhomogeneities. With an appropriate initialization, the LRGDF method could be applied to the segmentation of other kinds of ultrasound data such as liver [52], prostate [152] and skin [93]. The STS-LS method efficiently handles the depth-dependent inhomogeneities which are characteristics of HFU data presenting strong attenuation effects. Data that exhibit strong shadowing effects, however, may not be well handled by either the LRGDF or STS-LS methods. In such cases, shape priors [152, 153] could be integrated as an additional data term into the energy

functions of the LRGDF and STS-LS methods.

In this thesis, random forest classification (RFC) was employed to obtain an initial segmentation that was considered to be an initialization for the level-set methods. As discussed in Chapter 6, the RFC presented in this thesis could be extended in several ways by enriching the feature set, speeding up the feature extraction process by using C/C++ implementation, applying on-line random forest to avoid training from scratch, and improving the quality of manual segmentation used as labeled data for training the random forest classifier. Recently, stack random forest feature fusion [137] and deep neural decision forests [131] have been described and demonstrated to outperform traditional random forests. Future work could evaluate these two new frameworks within our dataset.

Appendix A

The LRGDF Method: From the Energy to the Evolution Equations

A.1 Two phases

The energy function $E(\phi)$

$$E[\phi] = E_D[\phi] + \mu E_R[\phi], \tag{A.1}$$

is the sum of a data term E_D and a regularization term E_R.

The data term is

$$E_D[\phi] = \int_\Omega \int_\Omega K_\rho(\mathbf{x}-\mathbf{y}) \left[-\sum_{i=1}^{2} \lambda_i M_i(\phi(\mathbf{y})) \ln p_i(I(\mathbf{y}); \theta_i(\mathbf{x})) \right] d\mathbf{y} d\mathbf{x}, \tag{A.2}$$

where $M_1(x) = H_\varepsilon(x)$, $M_2(x) = 1 - H_\varepsilon(x)$, and H_ε a regularized version of the Heaviside function which tends to H when $\varepsilon \to 0$.

The regularization term penalizes the length in 2D or surface in 3D of the boundary between the two regions,

$$E_R[\phi] = \int_\Omega |\nabla H_\varepsilon(\phi(\mathbf{x}))| \, d\mathbf{x}. \tag{A.3}$$

To minimize E, we derive the evolution equation:

$$\frac{\partial \phi}{\partial t} = -\left(\nabla E_D[\phi] + \mu \nabla E_R[\phi]\right). \tag{A.4}$$

from the Euler-Lagrange equation.

However we focus on the contribution of the data term as the contribution of the regularization term is well known [100] and is

$$\nabla E_R[\phi] = -\delta(\phi(\mathbf{x}))\,\mathrm{div}\left(\frac{\nabla\phi(\mathbf{x})}{|\nabla\phi(\mathbf{x})|}\right). \tag{A.5}$$

We rewrite $E_D[\phi]$ as

$$E_D[\phi] = -\int_\Omega \sum_{i=1}^{2} \lambda_i \int_\Omega K_\rho(\mathbf{x}-\mathbf{y}) \ln p_i(I(\mathbf{y});\theta_i(\mathbf{x}))\,d\mathbf{x} M_i(\phi(\mathbf{y}))\,d\mathbf{y}, \tag{A.6}$$

and we define $e_i(\mathbf{x})$, $i = 1,2$ as

$$e_i(\mathbf{x}) = \int_\Omega K_\rho(\mathbf{y}-\mathbf{x}) \ln p_i(I(\mathbf{x});\theta_i(\mathbf{y}))\,d\mathbf{y}. \tag{A.7}$$

So,

$$E_D[\phi] = -\int_\Omega \sum_{i=1}^{2} \lambda_i e_i(\mathbf{x}) M_i(\phi(\mathbf{x}))\,d\mathbf{x}. \tag{A.8}$$

For a small variation h, the G$\hat{a}$teaux variation of E_D is

$$\begin{aligned}\delta E_D[h,\phi] &= \frac{d}{dt} E_D[\phi + th]_{t=0} \\ &= -\int_\Omega \sum_{i=1}^{2} \lambda_i e_i(\mathbf{x}) M_i'(\phi(\mathbf{x}))\,h(\mathbf{x})\,d\mathbf{x}\end{aligned} \tag{A.9}$$

with

$$M_1'(x) = \delta_\varepsilon(x) \tag{A.10}$$

$$M_2'(x) = -\delta_\varepsilon(x). \tag{A.11}$$

The G$\hat{a}$teaux variation is interpreted as the scalar product of h and the function of interest:

$$\begin{aligned}\nabla E_D[\phi](\mathbf{y}) &= -\sum_{i=1}^{2} \lambda_i e_i(\mathbf{x}) M_i'(\phi(\mathbf{x})) \\ &= -\delta_\varepsilon(\phi(\mathbf{x}))\,(\lambda_1 e_1(\mathbf{x}) - \lambda_2 e_2(\mathbf{x})).\end{aligned}$$

Then the evolution equation is

$$\frac{\partial \phi}{\partial t}(\mathbf{x}) = \delta_\varepsilon(\phi(\mathbf{x}))\left[\lambda_1 e_1(\mathbf{x}) - \lambda_2 e_2(\mathbf{x}) + \mu \operatorname{div}\left(\frac{\nabla\phi(\mathbf{x})}{|\nabla\phi(\mathbf{x})|}\right)\right]. \tag{A.12}$$

A.2 Three phases

The three-phase energy function is

$$E[\phi_1, \phi_2] = E_D[\phi_1, \phi_2] + E_R[\phi_1, \phi_2], \tag{A.13}$$

with the data term:

$$E_D[\phi_1, \phi_2] = \int_\Omega \int_\Omega K_\rho(\mathbf{x}-\mathbf{y})\left[-\sum_{i=1}^{3} \lambda_i M_i(\phi_1(\mathbf{y}), \phi_2(\mathbf{y})) \ln p_i(I(\mathbf{y}); \theta_i(\mathbf{x}))\right] d\mathbf{y} d\mathbf{x}, \tag{A.14}$$

and the regularization term:

$$E_R(\phi_1, \phi_2) = \sum_{k=1}^{2} \mu_k \int_\Omega |\nabla H_\varepsilon(\phi_k(\mathbf{x}))| \, d\mathbf{x}, \tag{A.15}$$

where

$$M_1(x,y) = H_\varepsilon(x)H_\varepsilon(y), \qquad M_2(x,y) = (1-H_\varepsilon(x))H_\varepsilon(y),$$
$$M_3(x,y) = 1 - H_\varepsilon(y).$$

The gradients of the M_i are

$$\nabla M_1(x,y) = \begin{pmatrix} \delta_\varepsilon(x)H_\varepsilon(y) \\ H_\varepsilon(x)\delta_\varepsilon(y) \end{pmatrix}, \qquad \nabla M_2(x,y) = \begin{pmatrix} -\delta_\varepsilon(x)H_\varepsilon(y) \\ (1-H_\varepsilon(x))\,\delta_\varepsilon(y) \end{pmatrix},$$
$$\nabla M_3(x,y) = \begin{pmatrix} 0 \\ -\delta_\varepsilon(y) \end{pmatrix}.$$

As in 2 phases, the data term can be rewritten as:

$$\begin{aligned} E_D[\phi_1,\phi_2] &= -\int_\Omega \sum_{i=1}^{3} \lambda_i \int_\Omega K_\rho(\mathbf{y}-\mathbf{x}) \ln p_i(I(\mathbf{x});\theta_i(\mathbf{y}))\, d\mathbf{y} M_i(\phi_1(\mathbf{x}),\phi_2(\mathbf{x}))\, d\mathbf{x} \\ &= -\int_\Omega \sum_{i=1}^{3} \lambda_i e_i(\mathbf{x}) M_i(\phi_1(\mathbf{x}),\phi_2(\mathbf{x}))\, d\mathbf{x}, \end{aligned}$$

where $e_i(\mathbf{x})$ are similar to Eq. (A.7).

Then the two G*â*teaux variations are

$$\begin{aligned} \delta E_{D1}[h_1,\phi_1] =& \frac{d}{dt} E[\phi_1 + t h_1, \phi_2]_{t=0} \\ =& -\int_\Omega \delta_\varepsilon(\phi_1(\mathbf{x})) H_\varepsilon(\phi_2(\mathbf{x}))\,(\lambda_1 e_1(\mathbf{x}) - \lambda_2 e_2(\mathbf{x}))\, h_1(\mathbf{x}) d\mathbf{x}, \end{aligned} \tag{A.16}$$

$$\begin{aligned} \delta E_{D2}[h_2,\phi_2] =& \frac{d}{dt} E[\phi_2 + t h_2, \phi_2]_{t=0} \\ =& -\int_\Omega \delta_\varepsilon(\phi_2(\mathbf{x})) \Big(H_\varepsilon(\phi_1(\mathbf{x}))\,(\lambda_1 e_1(\mathbf{x}) - \lambda_2 e_2(\mathbf{x})) \\ & + (\lambda_2 e_2(\mathbf{x}) - \lambda_3 e_3(\mathbf{x})) \Big) h_2(\mathbf{x}) d\mathbf{x}. \end{aligned} \tag{A.17}$$

So with the same scalar-product argument, the evolution equations are

$$\begin{cases} \frac{\partial \phi_1}{\partial t} = \delta\phi_1(\mathbf{x}) \left[H(\phi_2(\mathbf{x}))\,(\lambda_1 e_1(\mathbf{x}) - \lambda_2 e_2(\mathbf{x})) + \mu_1 \mathrm{div}\left(\frac{\nabla \phi_1(\mathbf{x})}{|\nabla \phi_1(\mathbf{x})(|} \right) \right], \\ \frac{\partial \phi_2}{\partial t} = \delta\phi_2(\mathbf{x}) \left[H(\phi_1(\mathbf{x}))\,(\lambda_1 e_1(\mathbf{x}) - \lambda_2 e_2(\mathbf{x})) + \lambda_2 e_2(\mathbf{x}) - \lambda_3 e_3(\mathbf{x}) + \mu_2 \mathrm{div}\left(\frac{\nabla \phi_2(\mathbf{x})}{|\nabla \phi_2(\mathbf{x})|} \right) \right]. \end{cases} \tag{A.18}$$

The STS-LS Method: From the Energy to the Evolution Equations

B.1 Two phases

The energy function

$$\begin{aligned} E[\phi] =& E_D[\phi] + \mu E_R[\phi] \\ =& \int_\Omega \delta_\varepsilon(\phi(\mathbf{x})) \int_\Omega B(\mathbf{x},\mathbf{y})\, \mathscr{F}(\mathbf{x},\mathbf{y},I,\phi,B_T)\, d\mathbf{y} d\mathbf{x} + \mu \int_\Omega |\nabla H_\varepsilon(\phi(\mathbf{x}))|\, d\mathbf{x}, \end{aligned} \tag{B.1}$$

is composed of the data term $E_D[\phi]$ and the regularization term $E_R[\phi]$.

The data term energy only takes into account points that are closed to the zero level set of ϕ.

We define M_1 and M_2 as

$$\begin{aligned} M_1(\phi) =& H_\varepsilon(\phi), \\ M_2(\phi) =& 1 - H_\varepsilon(\phi). \end{aligned}$$

Let us define $B_\mathbf{x}$ (resp. $B_{T,\mathbf{x}}$) a small (resp. large) region centered at $\mathbf{x}$ for which $B(\mathbf{x},\mathbf{y}) = 1$ (resp. $B_T(\mathbf{x},\mathbf{y}) = 1$). $B_\mathbf{x}$ (resp. $B_{T,\mathbf{x}}$) can be subdivided in 2 non-intersecting sub-regions $B_{\mathbf{x},i}$ (resp. $B_{T,\mathbf{x},i}$), $i = 1,2$, of points that are part of region i. So $\mathbf{x}$ is not part of one of them.

In this Appendix, we focus our attention on the data term and the criterion $\mathscr{F}$. Regions parameters $\theta_i(\mathbf{x})$ are always estimated on $B_{T,\mathbf{x},i}$.

B.1.1 Lankton evolution equation

We derive the Lankton evolution from $\mathscr{F}_S$ with

$$\mathscr{F}_S(\mathbf{x},\mathbf{y},I,\phi,B_T) = -\sum_{i=1}^{2} \lambda_i M_i(\phi(\mathbf{y})) \ln p_i(I(\mathbf{x});\theta_i(\mathbf{y})). \tag{B.2}$$

The energy associated to each region $B_{\mathbf{x}}$ is based on the sum for all the subregions $B_{\mathbf{x},i}$ and all the points $\mathbf{y} \in B_{\mathbf{x},i}$ of the log-probability of the intensity $I(\mathbf{x})$ with parameter $\theta_i(\mathbf{y})$.

Note that $\mathbf{x}$ and $\mathbf{y}$ may well belong to 2 different subregions of the domain Ω, and this information is not taken into account in this energy.

λ_i are two constants close to 1 which provides some additional flexibility.

The G$\hat{a}$teaux variation is

$$\begin{aligned}
\delta E_{D_a}[h,\phi] =& \frac{d}{dt} E_{D_a}[\phi + th]_{t=0} \\
=& \int_\Omega \delta'_\varepsilon(\phi(\mathbf{x}))\, h(\mathbf{x}) \int_\Omega B(\mathbf{x},\mathbf{y})\, \mathscr{F}_S(\mathbf{x},\mathbf{y},I,\phi,B_T)\, d\mathbf{y} d\mathbf{x} \\
&+ \int_\Omega \delta_\varepsilon(\phi(\mathbf{x})) \int_\Omega B(\mathbf{x},\mathbf{y}) \left[-\sum_{i=1}^{2} \lambda_i M'_i(\phi(\mathbf{y})) h(\mathbf{y}) \ln p_i(I(\mathbf{x});\theta_i(\mathbf{y})) \right] d\mathbf{y} d\mathbf{x}.
\end{aligned} \tag{B.3}$$

As $\delta'_\varepsilon(0) = 0$ the first term is neglected near the zero level set and the role of $\mathbf{x}$ and $\mathbf{y}$ are exchanged,

$$\delta E_{D_a}[h,\phi] = \int_\Omega \int_\Omega \delta_\varepsilon(\phi(\mathbf{y}))\, B(\mathbf{y},\mathbf{x}) \left[-\sum_{i=1}^{2} \lambda_i M'_i(\phi(\mathbf{x})) \ln p_i(I(\mathbf{y});\theta_i(\mathbf{x})) \right] d\mathbf{y} h(\mathbf{x}) d\mathbf{x}. \tag{B.4}$$

We read the previous equation as the scalar-product between h and the function of interest. The gradient of the functional is

$$\nabla E_{D_a}[\phi](\mathbf{x}) = -\int_\Omega \delta_\varepsilon(\phi(\mathbf{y}))\, B(\mathbf{y},\mathbf{x}) \left[\sum_{i=1}^{2} \lambda_i M'_i(\phi(\mathbf{x})) \ln p_i(I(\mathbf{y});\theta_i(\mathbf{x})) \right] d\mathbf{y}. \tag{B.5}$$

When B is centrally symmetric $B(\mathbf{y},\mathbf{x}) = B(\mathbf{x},\mathbf{y})$ so

$$\nabla E_{D_a}[\phi](\mathbf{x}) = -\delta_\varepsilon(\phi(\mathbf{x})) \int_\Omega \delta_\varepsilon(\phi(\mathbf{y})) B(\mathbf{x},\mathbf{y}) \ln \frac{p_1^{\lambda_1}(I(\mathbf{y});\theta_1(\mathbf{x}))}{p_2^{\lambda_2}(I(\mathbf{y});\theta_2(\mathbf{x}))} d\mathbf{y}, \tag{B.6}$$

and the evolution equation is

$$\frac{\partial \phi}{\partial t}(\mathbf{x}) = \delta_\varepsilon(\phi(\mathbf{x}))\left[\int_\Omega \delta_\varepsilon(\phi(\mathbf{y}))B(\mathbf{x},\mathbf{y})\ln\frac{p_1^{\lambda_1}\left(I(\mathbf{y});\theta_1(\mathbf{x})\right)}{p_2^{\lambda_2}\left(I(\mathbf{y});\theta_2(\mathbf{x})\right)}d\mathbf{y} + \mu\,\mathrm{div}\left(\frac{\nabla\phi}{|\nabla\phi|}\right)\right]. \tag{B.7}$$

This equation is similar to the one derived by Lankton *et al.* [110] when $I(\mathbf{x})$ has a Gaussian statistics. But the evolution equation was derived from the energy based on the log-likelihood of the regions (See Section B.1.2 below). You may also find a different sign because in [110], H_ε is slightly different (i.e., $H_\varepsilon(x) = 0$ when $x > \varepsilon$, and $H_\varepsilon(x) = 1$ when $x < \varepsilon$).

They also did not introduce two different mask functions, so $B_T = B$.

B.1.2 $\mathscr{F}$ as the log-likelihood of the two regions

In this context $\mathscr{F}$ is based on the log-likelihood of the regions B_x centered on $\mathbf{x}$. The likelihood of each region $B_\mathbf{x}$ is the product for all $\mathbf{y}$ belonging to each sub-region $B_{\mathbf{x},i}$ of the probabilities $p_i\left(I(\mathbf{y});\theta_i(\mathbf{x})\right)$:

$$\mathscr{F}_\mathscr{L}(\mathbf{x},\mathbf{y},I,\phi,B_T) = -\sum_{i=1}^{2}\lambda_i M_i(\phi(\mathbf{y}))\ln p_i\left(I(\mathbf{y});\theta_i(\mathbf{x})\right). \tag{B.8}$$

With this model, the probability of the sub-region $B_{\mathbf{x},i}$ is described by the parameter $\theta_i(\mathbf{x})$ estimated on the larger sub-region $B_{T,\mathbf{x},i}$.

So at $\mathbf{x}$, 2 parameters, $\theta_1(\mathbf{x})$ and $\theta_2(\mathbf{x})$ are estimated, one for each sub-region of $B_{T,\mathbf{x}}$. When computing the probability of the point $\mathbf{y}$ which belong to region i, the pdf has parameter $\theta_i(\mathbf{x})$.

Eq. (B.4) is replaced by

$$\begin{aligned}\delta E_{D_\mathscr{L}}[h,\phi] = &\int_\Omega\int_\Omega \delta_\varepsilon\left(\phi(\mathbf{y})\right)B\left(\mathbf{y},\mathbf{x}\right)\\ &\times\left[-\sum_{i=1}^{2}\lambda_i M_i'(\phi(\mathbf{x}))\ln p_i\left(I(\mathbf{x});\theta_i(\mathbf{y})\right)\right]d\mathbf{y}h(\mathbf{x})d\mathbf{x}.\end{aligned} \tag{B.9}$$

Then with the same reasoning (centrally symmetric B, ...), the gradient of the functional is

$$\nabla E_{D_{\mathscr{L}}}[\phi](\mathbf{x}) = -\delta_\varepsilon(\phi(\mathbf{x})) \int_\Omega \delta_\varepsilon(\phi(\mathbf{y}))B(\mathbf{x},\mathbf{y}) \ln \frac{p_1^{\lambda_1}(I(\mathbf{x});\theta_1(\mathbf{y}))}{p_2^{\lambda_2}(I(\mathbf{x});\theta_2(\mathbf{y}))} d\mathbf{y}, \tag{B.10}$$

and the evolution equation is

$$\frac{\partial \phi}{\partial t}(\mathbf{x}) = \delta_\varepsilon(\phi(\mathbf{x}))\left[\int_\Omega \delta_\varepsilon(\phi(\mathbf{y}))B(\mathbf{x},\mathbf{y}) \ln \frac{p_1^{\lambda_1}(I(\mathbf{x});\theta_1(\mathbf{y}))}{p_2^{\lambda_2}(I(\mathbf{x});\theta_2(\mathbf{y}))} d\mathbf{y} + \mu \mathrm{div}\left(\frac{\nabla\phi}{|\nabla\phi|}\right)\right]. \tag{B.11}$$

Note that in Lankton paper [110], h is considered as a constant function in Eq. (B.9) (Eqs. (29)–(31) in [110]) and force a local variation along the normal direction of the level set function ϕ. Therefore, a different scalar-product is chosen, and the evolution equation Eq. (B.7) was derived.

B.2 Three phases

The 3-phase energy function:

$$E[\phi_1,\phi_2] = E_D[\phi_1,\phi_2] + E_R[\phi_1,\phi_2], \tag{B.12}$$

where the data term, $E_D[\phi_1,\phi_2]$, and regularization term, $E_R[\phi_1,\phi_2]$, are

$$E_D[\phi_1,\phi_2] = \sum_{k=1}^{2} \int_\Omega \delta(\phi_k(\mathbf{x})) \int_\Omega B(\mathbf{x},\mathbf{y}) \mathscr{F}(\mathbf{x},\mathbf{y},I,\phi_1,\phi_2,B_T)\, d\mathbf{y} d\mathbf{x}, \tag{B.13}$$

$$E_R(\phi_1,\phi_2) = \mu_1 \int_\Omega (|\nabla H_\varepsilon(\phi_1(\mathbf{x}))|\, d\mathbf{x} + \mu_2 \int_\Omega |\nabla H_\varepsilon(\phi_2(\mathbf{x}))|\, d\mathbf{x}. \tag{B.14}$$

We also define

$$\begin{aligned} M_1(\phi_1,\phi_2) &= H_\varepsilon(\phi_1)H_\varepsilon(\phi_2) \\ M_2(\phi_1,\phi_2) &= (1-H_\varepsilon(\phi_1))H_\varepsilon(\phi_2) \\ M_3(\phi_1,\phi_2) &= 1-H_\varepsilon(\phi_2), \end{aligned}$$

and consider two image criteria $\mathscr{F}_a$ and F_L.

B.2.1 Lankton evolution equation

It is based on $\mathscr{F}_a$ with

$$\mathscr{F}_a(\mathbf{x},\mathbf{y},I,\phi,B_T) = -\sum_{i=1}^{3} \lambda_i M_i(\phi_1(\mathbf{y}),\phi_2(\mathbf{y})) \ln p_i\left(I(\mathbf{x});\theta_i(\mathbf{y})\right). \tag{B.15}$$

Now we use the same machinery than before, and write the G$\hat{a}$teaux variations:

$$\begin{aligned}
\delta E_{D1_a}[h_1,\phi_1,\phi_2] =& \frac{d}{dt} E_D[\phi_1 + t h_1, \phi_2]_{t=0} \\
\delta E_{D2_a}[h_2,\phi_2,\phi_1] =& \frac{d}{dt} E_D[\phi_1, \phi_2 + t h_2]_{t=0}.
\end{aligned}$$

We focus our attention on $\delta E_{D1}[h_1,\phi_1,\phi_2]$

$$\begin{aligned}
\delta E_{D1_a} = & \int_{\Omega} \delta'_\varepsilon(\phi_1(\mathbf{x})) h_1(\mathbf{x}) \ldots d\mathbf{x} \\
& + \sum_{k=1}^{2} \int_{\Omega} \delta_\varepsilon(\phi_k(\mathbf{x})) \int_{\Omega} B(\mathbf{x},\mathbf{y}) \\
& \left[-\sum_{i=1}^{3} \lambda_i \frac{\partial M'_i}{\partial \phi_1}(\phi_1(\mathbf{y}),\phi_2(\mathbf{y})) h_1(\mathbf{y}) \ln p_i(I(\mathbf{x});\theta_i(\mathbf{y})) \right] d\mathbf{y} d\mathbf{x}.
\end{aligned} \tag{B.16}$$

We neglect the first term as $\delta'_\varepsilon(\phi_1(\mathbf{x})) = 0$ on the zero level set and get:

$$\begin{aligned}
\delta E_{D1_a} = & \sum_{k=1}^{2} \int_{\Omega} \delta_\varepsilon(\phi_k(\mathbf{x})) \int_{\Omega} B(\mathbf{x},\mathbf{y}) \\
& \left[-\sum_{i=1}^{3} \lambda_i \frac{\partial M'_i}{\partial \phi_1}(\phi_1(\mathbf{y}),\phi_2(\mathbf{y})) h_1(\mathbf{y}) \ln p_i(I(\mathbf{x});\theta_i(\mathbf{y})) \right] d\mathbf{y} d\mathbf{x},
\end{aligned} \tag{B.17}$$

The $\frac{\partial M_i'}{\partial \phi_1}$ is replaced by their respective values, and terms are reordered,

$$\begin{aligned}\delta E_{D1_a} =& -\sum_{k=1}^{2}\int_{\Omega}\delta_\varepsilon(\phi_1(\mathbf{y}))H_\varepsilon(\phi_2(\mathbf{y}))\\ &\times\int_{\Omega}\delta_\varepsilon(\phi_k(\mathbf{x}))B(\mathbf{x},\mathbf{y})\ln\frac{p_1^{\lambda_1}(I(\mathbf{x});\theta_1(\mathbf{y}))}{p_2^{\lambda_2}(I(\mathbf{x});\theta_2(\mathbf{y}))}d\mathbf{x}h_1(\mathbf{y})d\mathbf{y}.\\ =& -\int_{\Omega}\delta_\varepsilon(\phi_1(\mathbf{y}))H_\varepsilon(\phi_2(\mathbf{y}))\\ &\times\int_{\Omega}\left(\sum_{k=1}^{2}\delta_\varepsilon(\phi_k(\mathbf{x}))\right)B(\mathbf{x},\mathbf{y})\ln\frac{p_1^{\lambda_1}(I(\mathbf{x});\theta_1(\mathbf{y}))}{p_2^{\lambda_2}(I(\mathbf{x});\theta_2(\mathbf{y}))}d\mathbf{x}h_1(\mathbf{y})d\mathbf{y}.\end{aligned} \tag{B.18}$$

After exchanging $\mathbf{x}$ and $\mathbf{y}$ and taking into account the centrally symmetry of B, we derive the gradient of the functional,

$$\begin{aligned}\nabla E_{D1_a}[\phi_1,\phi_2](\mathbf{x}) =& -\delta_\varepsilon(\phi_1(\mathbf{x}))H_\varepsilon(\phi_2(\mathbf{x}))\\ &\times\int_{\Omega}\left(\sum_{k=1}^{2}\delta_\varepsilon(\phi_k(\mathbf{y}))\right)B(\mathbf{x},\mathbf{y})\ln\frac{p_1^{\lambda_1}(I(\mathbf{y});\theta_1(\mathbf{x}))}{p_2^{\lambda_2}(I(\mathbf{y});\theta_2(\mathbf{x}))}d\mathbf{y}.\end{aligned} \tag{B.19}$$

Concerning the second level set ϕ_2,

$$\begin{aligned}\nabla E_{D2_a}[\phi_1,\phi_2](\mathbf{x}) =& -\delta_\varepsilon(\phi_2(\mathbf{x}))\int_{\Omega}\left(\sum_{k=1}^{2}\delta_\varepsilon(\phi_k(\mathbf{y}))\right)B(\mathbf{x},\mathbf{y})\\ &\times\left[H_\varepsilon(\phi_1(\mathbf{x}))\ln\frac{p_1^{\lambda_1}(I(\mathbf{y});\theta_1(\mathbf{x}))}{p_2^{\lambda_2}(I(\mathbf{y});\theta_2(\mathbf{x}))}+\ln\frac{p_2^{\lambda_2}(I(\mathbf{y});\theta_2(\mathbf{x}))}{p_3^{\lambda_3}(I(\mathbf{y});\theta_3(\mathbf{x}))}\right]d\mathbf{y}.\end{aligned} \tag{B.20}$$

B.2.2 $\mathscr{F}$ as the log-likelihood of the three regions

Now $\mathscr{F}_{\mathscr{L}}$ is

$$\mathscr{F}_{\mathscr{L}}(\mathbf{x},\mathbf{y},I,\phi,B_T) = -\sum_{i=1}^{3}\lambda_i M_i(\phi_1(\mathbf{y}),\phi_2(\mathbf{y})))\ln p_i\left(I(\mathbf{y});\theta_i(\mathbf{x})\right), \tag{B.21}$$

so all occurences of $p_i(I(\mathbf{x});\theta_i(\mathbf{y}))$ in Eq. (B.15) are replaced by $p_i(I(\mathbf{y});\theta_i(\mathbf{x}))$.

With the same machinery than before, we finally find that all $p_i(I(\mathbf{y});\theta(\mathbf{x}))$ in Eqs. (B.19)–(B.20)

are replaced by $p_i(I(\mathbf{x});\theta_i(\mathbf{y}))$ and write:

$$\begin{aligned}\nabla E_{D1_{\mathscr{L}}}[\phi_1,\phi_2](\mathbf{x}) = &-\delta_\varepsilon(\phi_1(\mathbf{x}))H_\varepsilon(\phi_2(\mathbf{x})) \\ &\times \int_\Omega \left(\sum_{k=1}^{2}\delta_\varepsilon(\phi_k(\mathbf{y}))\right) B(\mathbf{x},\mathbf{y}) \ln \frac{p_1^{\lambda_1}(I(\mathbf{x});\theta_1(\mathbf{y}))}{p_2^{\lambda_2}(I(\mathbf{x});\theta_2(\mathbf{y}))} d\mathbf{y}. \end{aligned} \tag{B.22}$$

Concerning the second level set ϕ_2,

$$\begin{aligned}\nabla E_{D2_{\mathscr{L}}}[\phi_1,\phi_2](\mathbf{x}) = &-\delta_\varepsilon(\phi_2(\mathbf{x})) \int_\Omega \left(\sum_{k=1}^{2}\delta_\varepsilon(\phi_k(\mathbf{y}))\right) B(\mathbf{x},\mathbf{y}) \\ &\times \left[H_\varepsilon(\phi_1(\mathbf{x})) \ln \frac{p_1^{\lambda_1}(I(\mathbf{x});\theta_1(\mathbf{y}))}{p_2^{\lambda_2}(I(\mathbf{x});\theta_2(\mathbf{y}))} + \ln \frac{p_2^{\lambda_2}(I(\mathbf{x});\theta_2(\mathbf{y}))}{p_3^{\lambda_3}(I(\mathbf{x});\theta_3(\mathbf{y})}\right] d\mathbf{y}. \end{aligned} \tag{B.23}$$

Again with Lankton original derivation, one would read $p_i(I(\mathbf{y});\theta_i(\mathbf{x}))$ instead of $p_i(I(\mathbf{x});\theta_i(\mathbf{y}))$ in $\nabla E_{D1}[\phi_1,\phi_2]$ and $\nabla E_{D2}[\phi_1,\phi_2]$.

References

1. J. Mamou, A. Coron, M. Hata, J. Machi, E. Yanagihara, P. Laugier, and E. J. Feleppa, "Three-dimensional high-frequency characterization of cancerous lymph nodes," *Ultrasound in medicine & biology*, vol. 36, no. 3, pp. 361–375, 2010. xx, 8, 12, 17, 23, 96

2. J. Mamou, A. Coron, M. L. Oelze, E. Saegusa-Beecroft, M. Hata, P. Lee, J. Machi, E. Yanagihara, P. Laugier, and E. J. Feleppa, "Three-dimensional high-frequency backscatter and envelope quantification of cancerous human lymph nodes," *Ultrasound in medicine & biology*, vol. 37, no. 3, pp. 345–357, 2011. xx, 8, 12, 17, 45, 95, 96, 102

3. A. Coron, J. Mamou, E. Saegusa-Beecroft, M. L. Oelze, T. Yamaguchi, M. Hata, J. Machi, E. Yanagihara, P. Laugier, and E. J. Feleppa, "A quantitative ultrasound-based method and device for reliably guiding pathologists to metastatic regions of dissected lymph nodes," in *9th IEEE International Symposium on Biomedical Imaging (ISBI)*. IEEE, 2012, pp. 1064–1067. xx, 12

4. E. Saegusa-Beecroft, J. Machi, J. Mamou, M. Hata, A. Coron, E. T. Yanagihara, T. Yamaguchi, M. L. Oelze, P. Laugier, and E. J. Feleppa, "Three-dimensional quantitative ultrasound for detecting lymph node metastases," *Journal of surgical research*, vol. 183, no. 1, pp. 258–269, 2013. xx, 5, 8, 9, 12, 13, 102

5. G. Ghoshal, J. Mamou, and M. L. Oelze, "State of the art methods for estimating backscatter coefficients," in *Quantitative Ultrasound in Soft Tissues*. Springer, 2013, pp. 3–19. xx, 13

6. A. Coron, J. Mamou, M. Hata, J. Machi, E. Yanagihara, P. Laugier, and E. J. Feleppa, "Three-dimensional segmentation of high-frequency ultrasound echo signals from dissected lymph nodes," in *International Ultrasonics Symposium*. IEEE, 2008, pp. 1370–1373. xxi, 14, 34

7. K. Kawada and M. M. Taketo, "Significance and mechanism of lymph node metastasis in cancer progression," *Cancer research*, vol. 71, no. 4, pp. 1214–1218, 2011. 1

8. M. H. Ross and W. Pawlina, *Histology: A Text and Atlas: with Correlated Cell and Molecular Biology*, 6th ed., 2011. 1, 3

9. I. Albrecht and G. Christofori, "Molecular mechanisms of lymphangiogenesis in development and cancer," *International journal of developmental biology*, vol. 55, no. 4, p. 483, 2011. 1, 3, 4

10. L. P. Gartner and J. L. Hiatt, *Color atlas and text of histology*, 6th ed. Lippincott Williams & Wilkins, 2014. 2

11. J. S. Lowe and P. G. Anderson, *Stevens & Lowe's Human Histology: With STUDENT CONSULT Online Access*. Elsevier Health Sciences, 2014. 1

12. H. L. Ioachim and L. J. Medeiros, *Ioachim's lymph node pathology*. Lippincott Williams & Wilkins, 2012. 1

13. X. Cui, M. Hocke, C. Jenssen, A. Ignee, S. Klein, D. Schreiber-Dietrich, and C. Dietrich, "Conventional ultrasound for lymph node evaluation, update 2013," *Z Gastroenterol*, vol. 52, no. 02, pp. 212–221, 2014. 1

14. S. M. Qatarneh, I.-C. Kiricuta, A. Brahme, U. Tiede, and B. K. Lind, "Three-dimensional atlas of lymph node topography based on the visible human data set," *The Anatomical Record Part B: The New Anatomist*, vol. 289, no. 3, pp. 98–111, 2006. 1

15. E. R. Pereira, D. Jones, K. Jung, and T. P. Padera, "The lymph node microenvironment and its role in the progression of metastatic cancer," in *Seminars in cell & developmental biology*, vol. 38. Elsevier, 2015, pp. 98–105. 3, 5

16. M. B. Faries, I. Bedrosian, C. Reynolds, H. Q. Nguyen, A. Alavi, and B. J. Czerniecki, "Active macromolecule uptake by lymph node antigen-presenting cells: a novel mechanism in determining sentinel lymph node status," *Annals of surgical oncology*, vol. 7, no. 2, pp. 98–105, 2000. 3

17. B. S. Edge, D. Byrd, C. Compton *et al.*, *AJCC (American Joint Committee on Cancer) Cancer Staging Manual*. 7th Ed., New York, Springer-Verlag, 2010. 4, 5

18. B. S. Edge and C. C. Compton, "The american joint committee on cancer: the 7th edition of the AJCC cancer staging manual and the future of TNM," *Journal of Surgical Oncology*, vol. 17, no. 30, pp. 1471–1474, 2010. 4

19. G. H. Lyman, A. E. Giuliano, M. R. Somerfield, A. B. Benson, D. C. Bodurka, H. J. Burstein, A. J. Cochran, H. S. Cody, S. B. Edge, S. Galper *et al.*, "American society of clinical oncology guideline recommendations for sentinel lymph node biopsy in early-stage breast cancer," *Journal of Clinical Oncology*, vol. 23, no. 30, pp. 7703–7720, 2005. 4

20. B. Märkl, H. M. Arnholdt, H. Jähnig, H. Spatz, M. Anthuber, D. V. Oruzio, and T. G. Kerwel, "A new concept for the role of ex vivo sentinel lymph nodes in node-negative colorectal cancer," *Annals of surgical oncology*, vol. 17, no. 10, pp. 2647–2655, 2010. 4, 6

21. A. Resch and C. Langner, "Lymph node staging in colorectal cancer: old controversies and recent advances," *World J Gastroenterol*, vol. 19, no. 46, pp. 8515–8526, 2013. 4, 6, 7, 8

22. J. Mamou, A. Coron, E. Saegusa-Beecroft, M. Hata, E. Yanagihara, J. Machi, P. Laugier, and E. J. Feleppa, "Backscatter quantification for the detection of metastatic regions in human lymph nodes," in *Quantitative Ultrasound in Soft Tissues*. Springer, 2013, pp. 147–170. 5, 6, 8

23. P. S. Mullenix, P. L. Carter, M. J. Martin, S. R. Steele, C. L. Scott, M. J. Walts, and A. L. Beitler, "Predictive value of intraoperative touch preparation analysis of sentinel lymph nodes for axillary metastasis in breast cancer," *The American journal of surgery*, vol. 185, no. 5, pp. 420–424, 2003. 6

24. J. A. Guidroz, M. T. Johnson, C. E. Scott-Conner, B. R. De Young, and R. J. Weigel, "The use of touch preparation for the evaluation of sentinel lymph nodes in breast cancer," *The American Journal of Surgery*, vol. 199, no. 6, pp. 792–796, 2010. 6

25. M. Hata, J. Machi, J. Mamou, E. T. Yanagihara, E. Saegusa-Beecroft, G. K. Kobayashi, C. C. Wong, C. Fung, E. J. Feleppa, and K. Sakamoto, "Entire-volume serial histological examination for detection of micrometastases in lymph nodes of colorectal cancers," *Pathology & Oncology Research*, vol. 17, no. 4, pp. 835–841, 2011. 6, 8

26. O. Nordgård, S. Oltedal, H. Kørner, O. G. Aasprong, K. Tjensvoll, B. Gilje, and R. Heikkilä, "Quantitative RT-PCR detection of tumor cells in sentinel lymph nodes isolated from colon

cancer patients with an ex vivo approach," *Annals of surgery*, vol. 249, no. 4, pp. 602–607, 2009. 6, 8

27. D. Iddings, A. Ahmad, D. Elashoff, and A. Bilchik, "The prognostic effect of micrometastases in previously staged lymph node negative (N0) colorectal carcinoma: a meta-analysis," *Annals of surgical oncology*, vol. 13, no. 11, pp. 1386–1392, 2006. 7

28. J. Choi, S. N. Oh, D.-M. Yeo, W. K. Kang, C.-K. Jung, S. W. Kim, and M. Y. Park, "Computed tomography and magnetic resonance imaging evaluation of lymph node metastasis in early colorectal cancer," *World J Gastroenterol*, vol. 21, no. 2, pp. 556–562, 2015. 7

29. X.-W. Cui, C. Jenssen, A. Saftoiu, A. Ignee, and C. F. Dietrich, "New ultrasound techniques for lymph node evaluation," *World Journal of Gastroenterol*, vol. 19, no. 30, pp. 4850–4860, 2013. 7, 8

30. S. O. Hwang, S.-W. Lee, H. J. Kim, W. W. Kim, H. Y. Park, and J. H. Jung, "The comparative study of ultrasonography, contrast-enhanced MRI, and 18F-FDG PET/CT for detecting axillary lymph node metastasis in T1 breast cancer," *Journal of breast cancer*, vol. 16, no. 3, pp. 315–321, 2013. 7

31. A. T. Ahuja and M. Ying, "Sonographic evaluation of cervical lymph nodes," *American Journal of Roentgenology*, vol. 184, no. 5, pp. 1691–1699, 2005. 7

32. M.-H. Schmid-Wendtner, K. Partscht, H. C. Korting, and M. Volkenandt, "Improved differentiation of benign and malignant lymphadenopathy in patients with cutaneous melanoma by contrast-enhanced color doppler sonography," *Archives of dermatology*, vol. 138, no. 4, pp. 491–497, 2002. 7

33. F. Matsuzawa, K. Omoto, T. Einama, H. Abe, T. Suzuki, J. Hamaguchi, T. Kaga, M. Sato, M. Oomura, Y. Takata *et al.*, "Accurate evaluation of axillary sentinel lymph node metastasis using contrast-enhanced ultrasonography with Sonazoid in breast cancer: a preliminary clinical trial," *SpringerPlus*, vol. 4, no. 1, pp. 1–9, 2015. 8

34. A. E. Giuliano, D. Hawes, K. V. Ballman, P. W. Whitworth, P. W. Blumencranz, D. S. Reintgen, M. Morrow, A. M. Leitch, K. K. Hunt, L. M. McCall *et al.*, "Association of occult metastases in sentinel lymph nodes and bone marrow with survival among women with early-stage

invasive breast cancer," *Journal of the American Medical Association*, vol. 306, no. 4, pp. 385–393, 2011. 8

35. E. Lotspeich, M. Schoene, H. Gerngroß, R. Schmidt, R. Steinmann, M. Ramadani, and S. Gansauge, "Detection of disseminated tumor cells in the lymph nodes of colorectal cancer patients using a real-time polymerase chain reaction assay," *Langenbeck's Archives of Surgery*, vol. 392, no. 5, pp. 559–566, 2007. 8

36. Å. N. Öberg, G. E. Lindmark, A. C. Israelsson, S. G. Hammarström, and M.-L. K. Hammarström, "Detection of occult tumour cells in lymph nodes of colorectal cancer patients using real-time quantitative RT-PCR for CEA and CK20 mRNAS," *International journal of cancer*, vol. 111, no. 1, pp. 101–110, 2004. 8

37. Y. Ohi, Y. Umekita, Y. Sagara, Y. Rai, D. Yotsumoto, A. Matsukata, S. Baba, S. Tamada, Y. Matsuyama, M. Ando *et al.*, "Whole sentinel lymph node analysis by a molecular assay predicts axillary node status in breast cancer," *British journal of cancer*, vol. 107, no. 8, pp. 1239–1243, 2012. 8

38. L. B. Vegué, F. Rojo, D. Hardisson, A. C. Iturriagagoitia, M. J. Panadés, A. Velasco, E. L. Bonet, R. C. Muñoz, L. Polo *et al.*, "Comparison of molecular analysis and histopathology for axillary lymph node staging in primary breast cancer: results of the B-CLOSER-I study," *Diagnostic Molecular Pathology*, vol. 21, no. 2, pp. 69–76, 2012. 8

39. D. Hoon, L. Bernet, R. Cano, and G. Viale, "Molecular analysis of sentinel lymph nodes and search for molecular signatures of the metastatic potential of breast cancer." *The quarterly journal of nuclear medicine and molecular imaging: official publication of the Italian Association of Nuclear Medicine (AIMN)[and] the International Association of Radiopharmacology (IAR)*, vol. 58, no. 2, pp. 180–192, 2014. 8

40. O. Bernard, "Segmentation in echocardiographic imaging using parametric level set model driving by the statistics of the radiofrequency signal," Ph.D. dissertation, Ph. D. thesis, INSA-Lyon, 2006. 10

41. J. A. Noble and D. Boukerroui, "Ultrasound image segmentation: a survey," *IEEE Transactions on Medical Imaging*, vol. 25, no. 8, pp. 987–1010, 2006. 10, 16, 48

42. J. A. Zagzebski, J.-F. Chen, F. Dong, and T. Wilson, "Intervening attenuation affects first-order statistical properties of ultrasound echo signals," *Ultrasonics, Ferroelectrics, and Frequency Control, IEEE Transactions on*, vol. 46, no. 1, pp. 35–40, 1999. 10

43. R. F. Wagner, S. W. Smith, J. M. Sandrik, and H. Lopez, "Statistics of speckle in ultrasound B-scans." *IEEE transactions on Sonics and Ultrasonics*, no. 3, pp. 156–163, 1983. 10

44. P. M. Shankar, "A model for ultrasonic scattering from tissues based on the K distribution," *Physics in medicine and biology*, vol. 40, no. 10, p. 1633, 1995. 10, 11, 45

45. J. Mamou and M. L. Oelze, *Quantitative Ultrasound in Soft Tissues*. Springer Science & Business Media, 2013. 11, 45

46. G. Ghoshal, M. L. Oelze, and W. D. O'Brien Jr, "Quantitative ultrasound history and successes," in *Quantitative Ultrasound in Soft Tissues*. Springer, 2013, pp. 21–42. 11

47. F. L. Lizzi, M. Greenebaum, E. J. Feleppa, M. Elbaum, and D. J. Coleman, "Theoretical framework for spectrum analysis in ultrasonic tissue characterization," *The Journal of the Acoustical Society of America*, vol. 73, no. 4, pp. 1366–1373, 1983. 11

48. F. Lizzi, M. Ostromogilsky, E. Feleppa, M. Rorke, and M. Yaremko, "Relationship of ultrasonic spectral parameters to features of tissue microstructure," *Ultrasonics, Ferroelectrics, and Frequency Control, IEEE Transactions on*, vol. 34, no. 3, pp. 319–329, 1987. 11

49. M. F. Insana, T. J. Hall, and J. L. Fishback, "Identifying acoustic scattering sources in normal renal parenchyma from the anisotropy in acoustic properties," *Ultrasound in medicine & biology*, vol. 17, no. 6, pp. 613–626, 1991. 11

50. M. L. Oelze, J. F. Zachary, and W. D. O'Brien Jr, "Characterization of tissue microstructure using ultrasonic backscatter: Theory and technique for optimization using a Gaussian form factor," *The Journal of the Acoustical Society of America*, vol. 112, no. 3, pp. 1202–1211, 2002. 11

51. D. P. Hruska and M. L. Oelze, "Improved parameter estimates based on the homodyned K distribution," *IEEE Transactions on Ultrasonics, Ferroelectrics and Frequency Control*, vol. 56, no. 11, pp. 2471–2481, 2009. 11

52. T. Yamaguchi and H. Hachiya, "Proposal of a parametric imaging method for quantitative diagnosis of liver fibrosis," *Journal of Medical Ultrasonics*, vol. 37, no. 4, pp. 155–166, 2010. 13, 103

53. J. Mamou, O. Aristizábal, R. H. Silverman, J. A. Ketterling, and D. H. Turnbull, "High-frequency chirp ultrasound imaging with an annular array for ophthalmologic and small-animal imaging," *Ultrasound in medicine & biology*, vol. 35, no. 7, pp. 1198–1208, 2009. 18

54. J. Mamou, E. Saegusa-Beecroft, A. Coron, M. L. Oelze, T. Yamaguchi, M. Hata, J. Machil, E. Yanagihara, P. Laugier, and E. J. Feleppa, "Lymph explorer: A new GUI using 3D high-frequency quantitative ultrasound methods to guide pathologists towards metastatic regions in human lymph nodes," in *2012 IEEE International Ultrasonics Symposium (IUS)*. IEEE, 2012, pp. 2340–2343. 21

55. T. M. Bui, A. Coron, J. Mamou, E. Saegusa-Beecroft, T. Yamaguchi, E. Yanagihara, J. Machi, S. L. Bridal, and E. J. Feleppa, "Modeling the envelope statistics of three-dimensional high-frequency ultrasound echo signals from dissected human lymph nodes," *Japanese Journal of Applied Physics*, vol. 53, no. 7S, p. 07KF22, 2014. 25, 50, 51

56. Y. Zimmer, R. Tepper, and S. Akselrod, "A lognormal approximation for the gray level statistics in ultrasound images," in *Proceedings of the 22nd Annual International Conference of the IEEE Engineering in Medicine and Biology Society, 2000.*, vol. 4. IEEE, 2000, pp. 2656–2661. 25, 28

57. P. Shankar, V. A. Dumane, T. George, C. W. Piccoli, J. M. Reid, F. Forsberg, and B. B. Goldberg, "Classification of breast masses in ultrasonic B scans using Nakagami and K distributions," *Physics in medicine and biology*, vol. 48, no. 14, p. 2229, 2003. 25

58. Z. Tao, H. D. Tagare, and J. D. Beaty, "Evaluation of four probability distribution models for speckle in clinical cardiac ultrasound images," *IEEE Transactions on Medical Imaging*, vol. 25, no. 11, pp. 1483–1491, 2006. 25, 47, 51

59. M. M. Nillesen, R. G. Lopata, I. H. Gerrits, L. Kapusta, J. M. Thijssen, and C. L. de Korte, "Modeling envelope statistics of blood and myocardium for segmentation of echocardio-

graphic images," *Ultrasound in medicine & biology*, vol. 34, no. 4, pp. 674–680, 2008. 25, 47, 51

60. Y. Igarashi, T. Yamaguchi, and H. Hachiya, "Stability of quantitative evaluation method of liver fibrosis using amplitude distribution model of fibrotic liver," *Japanese Journal of Applied Physics*, vol. 50, no. 7S, p. 07HF17, 2011. 26

61. A. Koriyama, W. Yasuhara, and H. Hachiya, "Experimental evaluation of quantitative diagnosis technique for hepatic fibrosis using ultrasonic phantom," *Japanese Journal of Applied Physics*, vol. 51, no. 7S, p. 07GF09, 2012. 26

62. T. Higuchi, S. Hirata, T. Yamaguchi, and H. Hachiya, "Quantitative evaluation of liver fibrosis using multi-Rayleigh model with hypoechoic component," *Japanese Journal of Applied Physics*, vol. 52, no. 7S, p. 07HF19, 2013. 26

63. J. Anquez, E. Angelini, G. Grange, and I. Bloch, "Automatic segmentation of antenatal 3-D ultrasound images," *IEEE Transactions on Biomedical Engineering*, vol. 60, no. 5, pp. 1388–1400, 2013. 26, 28, 29, 46, 50, 51, 55, 62, 65, 75

64. B. Raju, M. Srinivasan *et al.*, "Statistics of envelope of high-frequency ultrasonic backscatter from human skin in vivo," *IEEE Transactions on Ultrasonics, Ferroelectrics, and Frequency Control*, vol. 49, no. 7, pp. 871–882, 2002. 26, 27, 28, 29

65. B. I. Raju, K. J. Swindells, S. Gonzalez, and M. A. Srinivasan, "Quantitative ultrasonic methods for characterization of skin lesions in vivo," *Ultrasound in medicine & biology*, vol. 29, no. 6, pp. 825–838, 2003. 26

66. G. Slabaugh, G. Unal, M. Wels, T. Fang, and B. Rao, "Statistical region-based segmentation of ultrasound images," *Ultrasound in medicine & biology*, vol. 35, no. 5, pp. 781–795, 2009. 26

67. P. Mohana Shankar, "A general statistical model for ultrasonic backscattering from tissues," *Ultrasonics, Ferroelectrics, and Frequency Control, IEEE Transactions on*, vol. 47, no. 3, pp. 727–736, 2000. 27, 28, 50

68. F. Shao, K. V. Ling, and W. S. Ng, "Automatic 3D prostate surface detection from TRUS with level sets," *International Journal of Image and Graphics*, vol. 4, no. 03, pp. 385–403,

2004. 28

69. W. Q. Meeker and L. A. Escobar, *Statistical methods for reliability data*. Wiley, New York, 1998. 28, 29

70. M. Nakagami, "The m-distribution - A general formula of intensity of rapid fading," in *Statistical Methods in Radio Wave Propagation*. Permagon, New York, 1960, p. 3. 28

71. M. B. Yacoub, "Fading distributions and co-channel interference in wireless systems," *IEEE Antennas and Propagation Magazine*, vol. 42, no. 1, pp. 150–160, 2000. 28

72. P. M. Shankar, V. Dumane, J. M. Reid, V. Genis, F. Forsberg, C. W. Piccoli, and B. B. Goldberg, "Classification of ultrasonic B-mode images of breast masses using Nakagami distribution," *IEEE Transactions on Ultrasonics, Ferroelectrics, and Frequency Control*, vol. 48, no. 2, pp. 569–580, 2001. 28

73. D. Fernandes and M. Sekine, "Suppression of weibull radar clutter," *IEICE transactions on communications*, vol. 76, no. 10, pp. 1231–1235, 1993. 28

74. P. Embrechts, C. Klüppelberg, and T. Mikosch, *Modelling extremal events for Insurance and Finance*. Springer Heidelberg, 1996, vol. 33. 29, 31

75. E. W. Stacy, "A generalization of the gamma distribution," *The Annals of Mathematical Statistics*, pp. 1187–1192, 1962. 29

76. M. P. Shankar, "Ultrasonic tissue characterization using a generalized Nakagami model," *IEEE Transactions on Ultrasonics, Ferroelectrics, and Frequency Control*, vol. 48, no. 6, pp. 1716–1720, 2001. 29

77. J. A. Greenwood and D. Durand, "Aids for fitting the gamma distribution by maximum likelihood," *Technometrics*, vol. 2, no. 1, pp. 55–65, 1960. 30

78. Q. Zhang, "A note on the estimation of nakagami-m fading parameter," *IEEE Communications Letters*, vol. 6, no. 6, pp. 237–238, 2002. 30

79. C. Walck, "Handbook on statistical distributions for experimentalists," p. 153, 2007. 31

80. E. W. Stacy and G. A. Mihram, "Parameter estimation for a generalized gamma distribution," *Technometrics*, vol. 7, no. 3, pp. 349–358, 1965. 31

81. J. D. Gibbons and S. Chakraborti, *Nonparametric statistical inference*. Marcel Dekker, New York, 2003. 32

82. T. Hastie, R. Tibshirani, and J. Friedman, *The Elements of Statistical Learning: Data Mining, Inference, and Prediction*, 2nd ed. Springer Verlag, 2009. 41, 43

83. C. de Boor, *A Practical Guide to Splines: Revised edition*. Springer-Verlag New York, 1978. 41, 43

84. M. Hansson, S. S. Brandt, J. Lindström, P. Gudmundsson, A. Jujić, A. Malmgren, and Y. Cheng, "Segmentation of B-mode cardiac ultrasound data by Bayesian probability maps," *Medical image analysis*, 2014. 46, 49

85. T. M. Bui, A. Coron, J. Mamou, E. Saegusa-Beecroft, E. Yanagihara, J. Machi, A. Dizeux, S. L. Bridal, and E. J. Feleppa, "Level-set segmentation of 2D and 3D ultrasound data using local gamma distribution fitting energy," in *IEEE International Symposium on Biomedical Imaging (ISBI)*. IEEE, 2015, pp. 1110–1113. 47, 50

86. J. Noble, "Ultrasound image segmentation and tissue characterization," *Proceedings of the Institution of Mechanical Engineers, Part H: Journal of Engineering in Medicine*, vol. 224, no. 2, pp. 307–316, 2010. 48

87. A. Katouzian, E. D. Angelini, S. G. Carlier, J. S. Suri, N. Navab, and A. F. Laine, "A state-of-the-art review on segmentation algorithms in intravascular ultrasound (IVUS) images," *IEEE Transactions on Information Technology in Biomedicine*, vol. 16, no. 5, pp. 823–834, 2012. 48

88. G. Xiao, M. Brady, J. A. Noble, and Y. Zhang, "Segmentation of ultrasound B-mode images with intensity inhomogeneity correction," *IEEE Transactions on Medical Imaging*, vol. 21, no. 1, pp. 48–57, 2002. 48

89. Y. Zhang, M. Brady, and S. Smith, "Segmentation of brain MR images through a hidden Markov random field model and the expectation-maximization algorithm," *IEEE Transactions on Medical Imaging*, vol. 20, no. 1, pp. 45–57, 2001. 48

90. D. Boukerroui, A. Baskurt, J. A. Noble, and O. Basset, "Segmentation of ultrasound images–multiresolution 2-D and 3-D algorithm based on global and local statistics," *Pattern Recognition Letters*, vol. 24, no. 4, pp. 779–790, 2003. 48

91. D. Boukerroui, O. Basset, N. Guerin, and A. Baskurt, "Multiresolution texture based adaptive clustering algorithm for breast lesion segmentation," *European Journal of Ultrasound*, vol. 8, no. 2, pp. 135–144, 1998. 48

92. F. Destrempes, J. Meunier, M.-F. Giroux, G. Soulez, and G. Cloutier, "Segmentation in ultrasonic B-mode images of healthy carotid arteries using mixtures of Nakagami distributions and stochastic optimization," *IEEE Transactions on Medical Imaging*, vol. 28, no. 2, pp. 215–229, 2009. 48

93. M. Pereyra, N. Dobigeon, H. Batatia, and J.-Y. Tourneret, "Segmentation of skin lesions in 2-D and 3-D ultrasound images using a spatially coherent generalized Rayleigh mixture model," *IEEE Transactions on Medical Imaging*, vol. 31, no. 8, pp. 1509–1520, 2012. 49, 78, 103

94. J.-W. Kuo, J. Mamou, Y. Wang, E. Saegusa-Beecroft, J. Machi, and E. J. Feleppa, "A novel nested graph cuts method for segmenting human lymph nodes in 3D high frequency ultrasound images," in *IEEE 12th International Symposium on Biomedical Imaging (ISBI)*. IEEE, 2015, pp. 372–375. 49

95. M. A. Figueiredo, J. Leitão, and A. K. Jain, "Unsupervised contour representation and estimation using B-splines and a minimum description length criterion," *IEEE Transactions on Image Processing*, vol. 9, no. 6, pp. 1075–1087, 2000. 49

96. P. Brigger, J. Hoeg, and M. Unser, "B-spline snakes: a flexible tool for parametric contour detection," *IEEE Transactions on Image Processing*, vol. 9, no. 9, pp. 1484–1496, 2000. 49

97. B. Li and S. T. Acton, "Active contour external force using vector field convolution for image segmentation," *IEEE Transactions on Image Processing*, vol. 16, no. 8, pp. 2096–2106, 2007. 49

98. R. Delgado-Gonzalo, P. Thévenaz, C. S. Seelamantula, and M. Unser, "Snakes with an ellipse-reproducing property," *IEEE Transactions on Image Processing*, vol. 21, no. 3, pp. 1258–1271, 2012. 49

99. R. Malladi, J. Sethian, B. C. Vemuri *et al.*, "Shape modeling with front propagation: A level set approach," *IEEE Transactions on Pattern Analysis and Machine Intelligence*, vol. 17, no. 2, pp. 158–175, 1995. 49

100. T. F. Chan and L. A. Vese, "Active contours without edges," *IEEE Trans. Image Processing*, vol. 10, no. 2, Feb. 2001. 49, 50, 106

101. A. Sarti, C. Corsi, E. Mazzini, and C. Lamberti, "Maximum likelihood segmentation of ultrasound images with Rayleigh distribution," *IEEE Transactions on Ultrasonics, Ferroelectrics and Frequency Control*, vol. 52, no. 6, pp. 947–960, 2005. 49, 50

102. F. Lecellier, S. Jehan-Besson, and J. Fadili, "Statistical region-based active contours for segmentation: an overview," *IRBM*, vol. 35, no. 1, pp. 3–10, 2014. 49

103. D. Cremers, M. Rousson, and R. Deriche, "A review of statistical approaches to level set segmentation: integrating color, texture, motion and shape," *Int. J. Comput. Vis.*, vol. 72, no. 2, pp. 195–215, 2007. 49, 50

104. M. Pereyra and H. Batatia, "Modeling ultrasound echoes in skin tissues using symmetric α-stable processes," *IEEE Transactions on Ultrasonics, Ferroelectrics and Frequency Control*, vol. 59, no. 1, pp. 60–72, 2012. 50

105. P. Martin, P. Réfrégier, F. Goudail, and F. Guérault, "Influence of the noise model on level set active contour segmentation," *IEEE Transactions on Pattern Analysis and Machine Intelligence*, vol. 26, no. 6, pp. 799–803, 2004. 50

106. F. Lecellier, J. Fadili, S. Jehan-Besson, G. Aubert, M. Revenu, and E. Saloux, "Region-based active contours with exponential family observations," *Journal of Mathematical Imaging and Vision*, vol. 36, no. 1, pp. 28–45, 2010. 50

107. S. Dahdouh, A. Serrurier, G. Grangé, E. D. Angelini, and I. Bloch, "Segmentation of fetal envelope from 3-D ultrasound images based on pixel intensity statistical distribution and shape priors," in *2013 IEEE 10th International Symposium on Biomedical Imaging (ISBI)*. IEEE, 2013, pp. 1026–1029. 50

108. S. Dahdouh, E. D. Angelini, G. Grangé, and I. Bloch, "Segmentation of embryonic and fetal 3D ultrasound images based on pixel intensity distributions and shape priors," *Medical image*

analysis, 2015. 50

109. C. Li, C. Kao, J. C. Gore, and Z. Ding, "Minimization of region-scalable fitting energy for image segmentation," *IEEE Trans. Image Process.*, vol. 17, no. 10, pp. 1940–1949, October 2008. 50, 51, 52, 54, 58, 66

110. S. Lankton and A. Tannenbaum, "Localizing region-based active contours," *IEEE Transactions on Image Processing*, vol. 17, no. 11, pp. 2029–2039, 2008. 50, 62, 65, 66, 68, 111, 112

111. L. Wang, L. He, A. Mishra, and C. Li, "Active contours driven by local Gaussian distribution fitting energy," *Signal Processing*, vol. 89, no. 12, pp. 2435–2447, 2009. 50, 51, 52, 55, 56, 58, 66

112. T. Brox and D. Cremers, "On local region models and a statistical interpretation of the piecewise smooth mumford-shah functional," *International Journal of Computer Vision*, vol. 84, no. 2, pp. 184–193, 2009. 50

113. D. Barbosa, T. Dietenbeck, J. Schaerer, J. D'hooge, D. Friboulet, and O. Bernard, "B-spline explicit active surfaces: An efficient framework for real-time 3-D region-based segmentation," *IEEE Transactions on Image Processing*, vol. 21, no. 1, pp. 241–251, 2012. 50

114. C. He, Y. Wang, and Q. Chen, "Active contours driven by weighted region-scalable fitting energy based on local entropy," *Signal Processing*, vol. 92, no. 2, pp. 587–600, 2012. 52

115. T.-Y. Hwang and P.-H. Huang, "On new moment estimation of parameters of the gamma distribution using its characterization," *Annals of the Institute of Statistical Mathematics*, vol. 54, no. 4, pp. 840–847, 2002. 53, 68

116. C. Li, R. Huang, Z. Ding, C. Gatenby, D. N. Metaxas, and J. C. Gore, "A level set method for image segmentation in the presence of intensity inhomogeneities with application to MRI," *IEEE Trans. Image Process.*, vol. 20, no. 7, pp. 2007–2016, July 2011. 53, 69

117. L. A. Vese and T. F. Chan, "A multiphase level set framework for image segmentation using the Mumford and Shah model," *International journal of computer vision*, vol. 50, no. 3, pp. 271–293, 2002. 53, 69

118. G. Gerig, O. Kübler, R. Kikinis, and F. A. Jolesz, "Nonlinear anisotropic filtering of MRI data," *IEEE Transactions on Medical Imaging*, vol. 11, no. 2, pp. 221–232, 1992. 55

119. C. J. V. Rijsbergen, *Information Retrieval*, 2nd ed. Newton, MA, USA: Butterworth-Heinemann, 1979. 55

120. D. Adalsteinsson and J. A. Sethian, "A fast level set method for propagating interfaces," *Journal of computational physics*, vol. 118, no. 2, pp. 269–277, 1995. 70

121. Y. N. Law, H. K. Lee, and A. M. Yip, "A multiresolution stochastic level set method for Mumford–Shah image segmentation," *IEEE Transactions on Image Processing*, vol. 17, no. 12, pp. 2289–2300, 2008. 70

122. M. Sussman, P. Smereka, and S. Osher, "A level set approach for computing solutions to incompressible two-phase flow," *Journal of Computational physics*, vol. 114, no. 1, pp. 146–159, 1994. 71

123. J. M. Bland and D. G. Altman, "Multiple significance tests: the Bonferroni method," *British Medical Journal*, vol. 310, no. 6973, p. 170, 1995. 75, 90

124. T. Brox and J. Weickert, "Level set segmentation with multiple regions," *IEEE Transactions on Image Processing*, vol. 15, no. 10, pp. 3213–3218, 2006. 82

125. T. M. Bui, A. Coron, J. Mamou, E. Saegusa-Beecroft, J. Machi, L. Bridal, and E. J. Feleppa, "Random forest classification and local region-based, level-set segmentation for quantitative ultrasound of human lymph nodes," in *IEEE International Ultrasonics Symposium (IUS)*. IEEE, 2015, pp. 1–4. 83

126. E. Alpaydin, *Introduction to machine learning*. MIT press, 2014. 84

127. I. El Naqa and M. J. Murphy, "What is machine learning?" in *Machine Learning in Radiation Oncology*. Springer, 2015, pp. 3–11. 84

128. L. Breiman, "Random forests," *Machine learning*, vol. 45, no. 1, pp. 5–32, 2001. 84, 87

129. R. Caruana, N. Karampatziakis, and A. Yessenalina, "An empirical evaluation of supervised learning in high dimensions," in *Proceedings of the 25th international conference on Machine learning*. ACM, 2008, pp. 96–103. 84

130. J. Gall, N. Razavi, and L. Van Gool, "An introduction to random forests for multi-class object detection," in *Outdoor and Large-Scale Real-World Scene Analysis*. Springer, 2012, pp. 243–263. 84

131. P. Kontschieder, M. Fiterau, A. Criminisi, and S. Rota Bulo, "Deep neural decision forests," in *Proceedings of the IEEE International Conference on Computer Vision*, 2015, pp. 1467–1475. 84, 104

132. A. Criminisi and J. Shotton, *Decision forests for computer vision and medical image analysis*. Springer Science & Business Media, 2013. 84, 87

133. V. Lempitsky, M. Verhoek, J. A. Noble, and A. Blake, "Random forest classification for automatic delineation of myocardium in real-time 3D echocardiography," in *Functional Imaging and Modeling of the Heart*. Springer, 2009, pp. 447–456. 84

134. M. Yaqub, R. Napolitano, C. Ioannou, A. T. Papageorghiou, and J. A. Noble, "Automatic detection of local fetal brain structures in ultrasound images," in *9th IEEE International Symposium on Biomedical Imaging (ISBI)*. IEEE, 2012, pp. 1555–1558. 84

135. M. Yaqub, M. K. Javaid, C. Cooper, and J. A. Noble, "Investigation of the role of feature selection and weighted voting in random forests for 3-D volumetric segmentation," *IEEE Transactions on Medical Imaging*, vol. 33, no. 2, pp. 258–271, 2014. 84

136. J. Shotton, T. Sharp, P. Kohli, S. Nowozin, J. Winn, and A. Criminisi, "Decision jungles: Compact and rich models for classification," in *Advances in Neural Information Processing Systems*, 2013, pp. 234–242. 84

137. Y. Cao, H. Wang, M. Moradi, P. Prasanna, and T. F. Syeda-Mahmood, "Fracture detection in X-ray images through stacked random forests feature fusion," in *12th International Symposium on Biomedical Imaging (ISBI)*. IEEE, 2015, pp. 801–805. 84, 104

138. J. Shotton, R. Girshick, A. Fitzgibbon, T. Sharp, M. Cook, M. Finocchio, R. Moore, P. Kohli, A. Criminisi, A. Kipman *et al.*, "Efficient human pose estimation from single depth images," *IEEE Transactions on Pattern Analysis and Machine Intelligence*, vol. 35, no. 12, pp. 2821–2840, 2013. 84

139. J. Deng, W. Dong, R. Socher, L.-J. Li, K. Li, and L. Fei-Fei, "Imagenet: A large-scale hierarchical image database," in *IEEE Conference on Computer Vision and Pattern Recognition, CVPR 2009*. IEEE, 2009, pp. 248–255. 84

140. P. Dollar, C. Wojek, B. Schiele, and P. Perona, "Pedestrian detection: An evaluation of the state of the art," *IEEE Transactions on Pattern Analysis and Machine Intelligence*, vol. 34, no. 4, pp. 743–761, 2012. 84

141. S. Sedai, P. K. Roy, and R. Garnavi, "Right ventricle landmark detection using multiscale hog and random forest classifier," in *12th International Symposium on Biomedical Imaging (ISBI)*. IEEE, 2015, pp. 814–818. 84

142. J. M. Bland and D. G. Altman, "Applying the right statistics: analyses of measurement studies," *Ultrasound in obstetrics & gynecology*, vol. 22, no. 1, pp. 85–93, 2003. 89

143. D.-R. Chen, R.-F. Chang, W.-J. Kuo, M.-C. Chen, and Y.-L. Huang, "Diagnosis of breast tumors with sonographic texture analysis using wavelet transform and neural networks," *Ultrasound in medicine & biology*, vol. 28, no. 10, pp. 1301–1310, 2002. 99

144. A. V. Alvarenga, W. C. Pereira, A. F. C. Infantosi, and C. M. Azevedo, "Complexity curve and grey level co-occurrence matrix in the texture evaluation of breast tumor on ultrasound images," *Medical physics*, vol. 34, no. 2, pp. 379–387, 2007. 99

145. M.-C. Yang, W. K. Moon, Y.-C. F. Wang, M. S. Bae, C.-S. Huang, J.-H. Chen, and R.-F. Chang, "Robust texture analysis using multi-resolution gray-scale invariant features for breast sonographic tumor diagnosis," *IEEE Transactions on Medical Imaging*, vol. 32, no. 12, pp. 2262–2273, 2013. 99

146. T. Ojala, M. Pietikäinen, and T. Mäenpää, "Multiresolution gray-scale and rotation invariant texture classification with local binary patterns," *IEEE Transactions on Pattern Analysis and Machine Intelligence*, vol. 24, no. 7, pp. 971–987, 2002. 99

147. Z. Guo, L. Zhang, and D. Zhang, "A completed modeling of local binary pattern operator for texture classification," *IEEE Transactions on Image Processing*, vol. 19, no. 6, pp. 1657–1663, 2010. 99

148. H. Yoshida, D. D. Casalino, B. Keserci, A. Coskun, O. Ozturk, and A. Savranlar, "Wavelet-packet-based texture analysis for differentiation between benign and malignant liver tumours in ultrasound images," *Physics in Medicine and Biology*, vol. 48, no. 22, p. 3735, 2003. 99

149. J. Virmani, V. Kumar, N. Kalra, and N. Khandelwal, "SVM-based characterization of liver ultrasound images using wavelet packet texture descriptors," *Journal of digital imaging*, vol. 26, no. 3, pp. 530–543, 2013. 99

150. A. Saffari, C. Leistner, J. Santner, M. Godec, and H. Bischof, "On-line random forests," in *12th International Conference on Computer Vision Workshops (ICCV Workshops)*. IEEE, 2009, pp. 1393–1400. 99

151. S. Schulter, C. Leistner, P. M. Roth, H. Bischof, and L. J. Van Gool, "On-line hough forests." in *British Machine Vision Conference*, 2011, pp. 1–11. 99

152. L. Saroul, O. Bernard, D. Vray, and D. Friboulet, "Prostate segmentation in echographic images: A variational approach using deformable super-ellipse and rayleigh distribution," in *5th IEEE International Symposium on Biomedical Imaging: From Nano to Macro (ISBI)*. IEEE, 2008, pp. 129–132. 103

153. T. Dietenbeck, "Segmentation of 2D-echocardiographic sequences using level-set constrained with shape and motion priors," Ph.D. dissertation, INSA de Lyon, 2012. 103